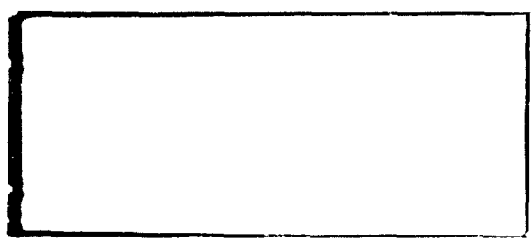
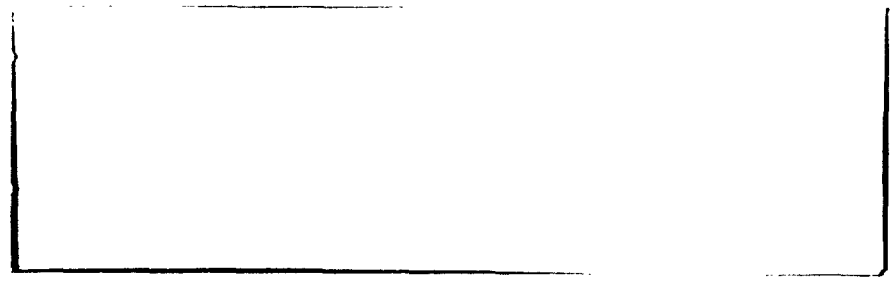


①

408 556

AD No. ~~408556~~

DDC FILE COPY



5000

ORDNANCE RESEARCH LABORATORY
The Pennsylvania State University
University Park, Pennsylvania

JUN 27

TISIA

NAVY DEPARTMENT BUREAU OF NAVAL WEAPONS CONTRACT NORD 1

\$12.50

(4) \$12.50
(5) 671300

(6)

PROPELLERS WITH DISTORTED INFLOW,

(7)

By J. J. Eisenhuth

(8) NA

(9) MA

(10) NA

(11) 12 June 63

(12) 153 p

(13) NA

(14) MA

(15) 11

(16) MA

Technical Memorandum

File No. TM 5.2410-20

June 12, 1963

Copy No. 11

(15) Distorted NOrel
16-19 NA

Abstract:

Am2 *was made of the*
~~This~~ investigation is concerned with the steady-state reaction of a propeller to velocity perturbations induced by deflected control surfaces located upstream of the propeller. The study was pursued along both theoretical and experimental lines. Theoretically, actuator disk theory is used, first, to represent the control surfaces and introduce a distortion into the flow and, secondly, to represent the action of the propeller when exposed to the distorted flow. The problem is reduced to a boundary value problem by linearizing the equations of motion and the continuity equation and then solved by proper choice of boundary and matching conditions at the actuator discs.

The experimental results show that the maximum reactive force of the propeller is about 34 per-cent of the control surface force. This maximum occurs for a 10-bladed propeller with lesser percentages occurring for propellers of 2 and 5 blades. Practically no variation with advance ratio and spacing distance was measured.

The conclusion is made that, although further work is needed particularly with regard to computational accuracy, the theoretical method is a useable one which can easily be extended to the case of a ducted rotating device.

ACKNOWLEDGMENTS

The author wishes to express his sincere appreciation for the guidance of his advisor, Dr. H. Yeh, particularly in the theoretical development of the study. Special thanks is also expressed to the chairman of his committee, Dr. G. F. Wislicenus, for his overall guidance and instructive comments.

The investigation was performed at the Garfield Thomas Water Tunnel of the Ordnance Research Laboratory under U. S. Navy Contract NOrd 16597. Appreciation is offered to members of the laboratory who contributed in many ways. Particular thanks go to S. M. Laposata who gave invaluable assistance in programming the computations; to G. B. Gurney for his assistance in the experimental instrumentation; and to H. D. Cannon, R. F. Davis, J. M. Long, W. S. Gearhart, and M. W. McBride and his tunnel crew for their individual contributions to the success of the experimental program.

SUMMARY

Statement of the Problem

The purpose of this investigation is, in general, to determine the steady-state reaction of a propeller to velocity perturbations induced by deflected control surfaces located upstream of the propeller. A propeller operating in such a distorted flow will tend to straighten the flow, thus producing forces that are opposite to those induced by the control surfaces. The effectiveness of the control surfaces is therefore reduced.

Origin of the Problem

Theoretically, the investigation belongs to a class of problems characterized as flow distortion problems. Most of the steady-state investigations of this class have their origin in the axial flow compressor field. Here the principal interest is in predicting the flow leaving a blade row.

Two distinct types of distortion, radial⁵ and circumferential⁶ have been treated. A combination of both these types was investigated with reference to a plane cascade of airfoils⁷. There was consequently a need for a three-dimensional analysis of radially and circumferentially distorted flows in cylindrical

coordinates. This need, combined with the practical problem of propeller reaction to control surface deflections, forms the basis for this investigation.

Procedure of the Investigation

The investigation was pursued along both theoretical and experimental lines. Theoretically, actuator disc theory is used, first, to represent the control surfaces and introduce a distortion into the flow and, secondly, to represent the action of a propeller when exposed to a distorted flow. The distorted flow investigated is that produced by two control surfaces, vertically oriented 180 degrees apart, deflecting the flow in the same sideward direction.

The approach that in general is followed is to linearize the equations of motion and the continuity equation and combine them to produce a single differential equation for the pressure perturbation. By assuming a series solution for this equation, expressions for the velocity perturbations are derived which can be evaluated by proper choice of boundary and matching conditions at the actuator discs. The perturbations that are still present in the flow downstream of the propeller disc are a measure of the reaction of the propeller to the distorted inflow. The prediction of

the velocity perturbations just upstream and just downstream of the propeller disc permits the estimation of the force reaction to the distorted inflow.

The experimental part of the investigation was divided into two phases. The first phase was devoted purely to the measurement of the distortion induced by the deflected control surfaces. This was accomplished with a three-dimensional, pitot type probe. The second phase was concerned with the measurement of the propeller reaction to the flow distortions. These measurements included velocity surveys downstream of the propeller and force measurements of the control surfaces and propeller.

In both the theoretical and experimental phases account was taken of the propeller reaction to variations in propeller advance ratio, spacing distance between control surfaces and propeller, and numbers of propeller blades.

Results

The distribution of velocity perturbations measured immediately downstream of the propeller shows that the general shape of the original disturbance is maintained. The magnitude is less and as such is a measure of the reaction of the propeller.

The force measurements show that the maximum reactive side force of the propeller is about 34 per cent of the control surface force. This maximum occurs for a 10-bladed propeller. Lesser percentages occur for propellers of 2 and 5 blades. Practically no variation with advance ratio or spacing distance was measured.

The theoretical representation of the velocity perturbations by series was generally good. One exception occurred with the radial component of velocity perturbation downstream of the control surface. A vortex trailing from each control surface tip occurs in this region. The predicted values were considerably larger than those measured. An explanation for this lies in the difference between a real flow vortex with viscous effects and a potential vortex represented only approximately by a truncated series.

There is an indication, by virtue of the prediction of velocity perturbations in the vicinity of the propeller disc and of the resulting predicted side-force, that the action of the propeller is either not properly represented or that the series representing this action were not carried to a sufficiently large number of terms. Nevertheless, the force prediction for the 5-bladed propeller with comparatively close spacing between propeller and control surfaces was good. The predicted

gradient of propeller side-force with number of blades, however, was larger than that measured.

There was a breakdown of the velocity perturbation predictions for larger spacings. This was traceable to an accuracy problem in the computations that occurred with large exponential values. The major portion of this problem was corrected by simplifying certain equations. Enough inaccuracy still exists, however, to make the predictions for larger spacings generally unreliable.

Conclusions

In the light of the results of the investigation, the following conclusions can be made:

1. The experimental results give a very good picture of the force cancellation by the propeller.
2. The theoretical method that was developed appears to be a useable one.
3. The theory is being extended to its limits when applied to a case with a strong vortex present.
4. The theoretical approach can probably be extended easily to the case of a ducted rotating device.

5. The agreement of theory with experiment is sufficiently good to warrant further studies concerned chiefly with improving the accuracy of predictions.

Suggestions for Further Research

The following suggestions are made with regard to future work in this general area:

1. Extension of work with the existing experimental setup to cover other practical configurations should be attempted.
2. Ways to improve the computing accuracy of a study such as this should be undertaken.
3. An extension of the theory to the case of control surfaces and propellers immersed in the boundary layer of a body should be pursued.
4. An extension of this theoretical approach to pumps and compressors should be tried.

TABLE OF CONTENTS

	Page
ACKNOWLEDGMENTS	ii
SUMMARY	iii
TABLE OF CONTENTS	ix
LIST OF TABLES	xii
LIST OF FIGURES	xiii
LIST OF SYMBOLS	xviii
 Chapter	
I. INTRODUCTION	
Origin of the Problem	1
Statement of the Problem and Its Limitations	3
 II. DEVELOPMENT OF THEORY	
Formulation of the Problem	6
Solution of Pressure Equation	7
Velocity Perturbations	10
Boundary Conditions	11
Functions of Integration	13
Unknowns	15
Specification of Flow Distortion at Disc A	16
Specification of Propeller Mean Swirl. .	18
Propeller Normality Condition	20
Continuity at Disc B	22
Continuity at Disc A	23

Chapter	Page
Relation Between Tangential Velocity Perturbations at Disc A	24
Relation Between Tangential and Axial Velocity Perturbations at Disc B	27
Solution of Unknown Coefficients	28
III. MEASUREMENT OF FLOW DISTORTION	
Experimental Setup	31
Instrumentation	32
Experimental Procedure	34
Experimental Results	35
IV. MEASUREMENT OF PROPELLER REACTION TO A FLOW DISTORTION	
Experimental Setup	37
Propeller Design	37
Instrumentation	38
Experimental Procedure	39
Force Measurement Results	40
Results of Velocity Survey	42
V. THEORETICAL COMPUTATIONS	
Eigenvalue Calculations	43
Propeller Properties	44
Computing Accuracy	45
Calculation of Velocity Perturbations	47
Calculation of Propeller Forces	49

Chapter	Page
VI. DISCUSSION OF RESULTS AND CONCLUSIONS	
Experimental Results	52
Theoretical Results	53
Conclusions	55
Suggestions for Further Research	56
REFERENCES	58
APPENDIX A: DERIVATION OF PRESSURE EQUATION . . .	61
APPENDIX B: DERIVATION OF VELOCITY PERTURBATION EQUATIONS	64
APPENDIX C: DERIVATION OF RELATION BETWEEN TANGENTIAL AND AXIAL VELOCITY PERTURBATIONS AT DISC B	68
APPENDIX D: SOLUTION OF UNKNOWN COEFFICIENT, C_{mn} .	76
APPENDIX E: COMPUTATIONAL PROCEDURES	81
APPENDIX F: REDUCTION OF C_{mn} EQUATION	85

LIST OF TABLES

Table		Page
I	Summation Values for α_{12} , γ_{12} , λ_{12}	45
II	Calculated Force Coefficients	50

LIST OF FIGURES

Figure		Page
1.	Theoretical Model for Flow Distortion Study	88
2.	Normal Velocity Diagram for Blade Section	89
3.	Velocity Diagram of Blade Section in Distorted Flow	90
4.	Interim Model with Velocity Probe	91
5.	Interim Model with Velocity Probe and Traversing Unit	92
6.	Typical Results of Velocity Survey . . .	93
7.	Measured Distribution of v_{u_1} at $z = -d$.	94
8.	Measured Distribution of v_{u_2} at $z = -d$.	95
9.	Measured Distribution of v_{r_1} at $z = -d$.	96
10.	Measured Distribution of v_{r_2} at $z = -d$.	97
11.	Measured Distribution of v_{z_1} at $z = -d$.	98
12.	Measured Distribution of v_{z_2} at $z = -d$.	99
13.	Flow Distortion Model with 10-bladed Propeller	100
14.	View of Flow Distortion Model from Upstream to Downstream	101
15.	Strain-Gaged Assemblies for Force Measurements	102
16.	Measured Force Coefficients for $d/R_p = 0.267$, $B = 10$	103
17.	Measured Force Coefficients for $d/R_p = 0.667$, $B = 10$	104

Figure		Page
18.	Measured Force Coefficients for $d/R_p = 1.067$, $B = 10$	105
19.	Measured Force Coefficients for $d/R_p = 0.267$, $B = 5$	106
20.	Measured Force Coefficients for $d/R_p = 0.667$, $B = 5$	107
21.	Measured Force Coefficients for $d/R_p = 1.067$, $B = 5$	108
22.	Measured Force Coefficients for $d/R_p = 0.267$, $B = 2$	109
23.	Measured Force Coefficients for $d/R_p = 0.667$, $B = 2$	110
24.	Measured Force Coefficients for $d/R_p = 1.067$, $B = 2$	111
25.	Measured Force Coefficients for $d/R_p = 0.267$, $B = 10$, $J = 2.0$	112
26.	Measured Force Coefficients for $d/R_p = 0.667$, $B = 10$, $J = 2.0$	113
27.	Measured Force Coefficients for $d/R_p = 1.067$, $B = 10$, $J = 2.0$	114
28.	Measured Force Coefficients for $d/R_p = 0.267$, $B = 5$, $J = 2.0$	115
29.	Measured Force Coefficients for $d/R_p = 0.667$, $B = 5$, $J = 2.0$	116
30.	Measured Force Coefficients for $d/R_p = 1.067$, $B = 5$, $J = 2.0$	117
31.	Measured Force Coefficients for $d/R_p = 0.267$, $B = 2$, $J = 2.0$	118
32.	Measured Force Coefficients for $d/R_p = 0.667$, $B = 2$, $J = 2.0$	119
33.	Measured Force Coefficients for $d/R_p = 1.067$, $B = 2$, $J = 2.0$	120

Figure		Page
34.	Effect of Spacing Distance on Force Coefficients	121
35.	Effect of Blade Number on Force Coefficients	122
36.	Measured Distribution of v_{u_3} at $z/R_p = 0.267$ ($d/R_p = 0.267$, $B = 10$) . . .	123
37.	Measured Distribution of v_{u_3} at $z/R_p = 2.667$ ($d/R_p = 0.267$, $B = 10$) . . .	124
38.	Radial Distribution of $M(r)$	125
39.	Radial Distribution of $N(r)$	126
40.	Calculated Distribution of v_{u_1} at $z = -d$ ($d/R_p = 0.267$, $B = 10$)	127
41.	Calculated Distribution of v_{r_1} at $z = -d$ ($d/R_p = 0.267$, $B = 10$)	128
42.	Calculated Distribution of v_{z_1} and v_{z_2} at $z = -d$ ($d/R_p = 0.267$, $B = 10$)	129
43.	Calculated Distribution of v_{u_2} at $z = -d$ ($d/R_p = 0.267$, $B = 10$)	130
44.	Calculated Distribution of v_{r_2} at $z = -d$ ($d/R_p = 0.267$, $B = 10$)	131
45.	Calculated Distribution of v_{u_2} at $z = -d$ ($d/R_p = 0.267$, $B = 10$)	132
46.	Calculated Distribution of v_{r_2} at $z = -d$ ($d/R_p = 0.267$, $B = 10$)	133
47.	Calculated Distribution of v_{z_2} and v_{z_3} at $z = -d$ ($d/R_p = 0.267$, $B = 10$)	134
48.	Calculated Distribution of v_{u_3} at $z = -d$ ($d/R_p = 0.267$, $B = 10$)	135

Figure		Page
49.	Calculated Distribution of v_{r3} at $z = d$ ($d/R_p = 0.267$, $B = 10$)	136
50.	Calculated Distribution of v_{u2} at $z = d$ ($d/R_p = 0.267$, $B = 5$)	137
51.	Calculated Distribution of v_{r2} at $z = d$ ($d/R_p = 0.267$, $B = 5$)	138
52.	Calculated Distribution of v_{z2} and v_{z3} at $z = d$ ($d/R_p = 0.267$, $B = 5$)	139
53.	Calculated Distribution of v_{u3} at $z = d$ ($d/R_p = 0.267$, $B = 5$)	140
54.	Calculated Distribution of v_{r3} at $z = d$ ($d/R_p = 0.267$, $B = 5$)	141
55.	Calculated Distribution of v_{u2} at $z = d$ ($d/R_p = 0.267$, $B = 2$)	142
56.	Calculated Distribution of v_{r2} at $z = d$ ($d/R_p = 0.267$, $B = 2$)	143
57.	Calculated Distribution of v_{z2} and v_{z3} at $z = d$ ($d/R_p = 0.267$, $B = 2$)	144
58.	Calculated Distribution of v_{u3} at $z = d$ ($d/R_p = 0.267$, $B = 2$)	145
59.	Calculated Distribution of v_{r3} at $z = d$ ($d/R_p = 0.267$, $B = 2$)	146
60.	Calculated Distribution of v_{u2} at $z = d$ ($d/R_p = 0.667$, $B = 10$)	147
61.	Calculated Distribution of v_{z2} and v_{z3} at $z = d$ ($d/R_p = 0.667$, $B = 10$)	148
62.	Calculated Distribution of v_{u3} at $z = d$ ($d/R_p = 0.667$, $B = 10$)	149
63.	Calculated Distribution of v_{u2} at $z = d$ ($d/R_p = 1.067$, $B = 10$)	150

Figure		Page
64.	Calculated Distribution of v_{z_2} and v_{z_3} at $z = d(d/R_p = 1.067, B = 10)$	151
65.	Calculated Distribution of v_{u_3} at $z = d(d/R_p = 1.067, B = 10)$	152
66.	Comparison of Measured and Calculated Force Coefficients	153

LIST OF SYMBOLS

A_{mn}	coefficient for velocity perturbation series in region (1)
a_{mn}	coefficient for pressure perturbation series in region (1)
B	number of propeller blades
B_{mn}	coefficient for velocity perturbation series in region (2)
b_{mn}	coefficient for pressure perturbation series in region (2)
c	blade section chord length
C_{cs}	coefficient of control surface side force
C_f	force coefficient defined by Equation (51)
C_H	coefficient of propeller side force
c_ℓ	blade section lift coefficient
$c_{\ell 0}$	blade section lift coefficient at zero angle of attack
C_{mn}	coefficient for velocity perturbation series in region (2)
c_{mn}	coefficient for pressure perturbation series in region (2)
C_{Q_f}	torque force coefficient
C_v	coefficient of propeller vertical force
d	half of spacing distance between Disc A and Disc B
D_{mn}	coefficient for velocity perturbation series in region (3)

d_{mn}	coefficient for pressure perturbation series in region (3)
D_p	propeller diameter
E	real part of C_{mn} coefficient
F	imaginary part of C_{mn} coefficient
$f(r, \varphi)$	function of integration for radial velocity perturbation
$g(r, \varphi)$	function of integration for tangential velocity perturbation
$h(r, \varphi)$	function of integration for axial velocity perturbation
$I_{0\ell}$	coefficient for series representing mean axial velocity component of propeller induced velocity
J	propeller advance ratio $= \frac{V_z}{2n R_p}$
$J_m(k_{mn}r)$	Bessel function of the first kind
k_{mn}	Eigenvalue
$K(r)$	function representing action of propeller
$L_{0\ell}$	coefficient for series representing mean tangential component of propeller induced velocity
m	order of Bessel function
$M(r)$	function relating v_{z_2} and v_{u_3} at propeller disc
n	propeller rotational speed
$N(r)$	function relating v_{u_2} and v_{u_3} at propeller disc
N_{mn}	normalizing factor for Fourier Bessel Coefficient

O_{mn}	coefficient for axial velocity perturbation series in region (2)
P	pressure
p	pressure perturbation
P_{mn}	Fourier-Bessel coefficient for prescribed distortion in region (2)
$P_m(x)$	series in Bessel function asymptotic expression
Q_f	propeller torque force
$Q_m(x)$	series in Bessel function asymptotic expression
r	radial distance
r_h	hub radius
R_{mn}	radius function in the assumed solution of pressure equation
r_o	outer radius at which v_u goes to zero
R_p	propeller tip radius
s	index in Bessel function series
S	function defined in Equations (D-5)
T	function defined in Equations (D-5)
U	function defined in Equations (D-5)
v_{BV}	velocity induced by bound vortex
V_e	relative velocity at propeller blade section
V_r	velocity in radial direction
v_r	velocity perturbation in radial direction

V_u	velocity in circumferential direction
v_u	velocity perturbation in circumferential direction
V_z	velocity in axial direction
v_z	velocity perturbation in axial direction
\bar{V}_z	primary velocity
w	velocity induced at a wing
w_a	component of propeller induced velocity in the z direction
w_t	component of propeller induced velocity in circumferential direction
x	relative radius ($= r/R_p$); Bessel function argument
$Y_m(k_{mn}r)$	Bessel function of the second kind
z	distance in axial direction
$Z_m(k_{mn}r)$	Bessel function of both kinds
α	exponent for assumed distribution of \bar{V}_z
$\alpha_{i,l}$	coefficient in series representation of $M(r)$
β_{mn}	constant relating Bessel function of the first kind with Bessel function of the second kind
$\gamma_{i,l}$	coefficient in series representation of $N(r)/r$
δ_m	order of Bessel function for radially varying primary velocity, $\bar{V}_z(r)$
θ	angle of relative velocity at propeller blade section

K	Goldstein averaging factor
λ_{μ}	coefficient in series representation of $\frac{1}{r}$
μ	term in Bessel function asymptotic expansion (= $4m^2$)
ξ_m	term in Bessel function asymptotic expansion (= $x - 1/2 (m + 1/2) \pi$)
ρ	mass density of fluid
ϕ	circumferential angle
ψ	angle of relative velocity at propeller blade section when flow is distorted

Subscripts

m	order of Bessel function
n	Eigenvalue index
1	region (1)
2	region (2)
3	region (3)

Superscript

$()'$	indicates quantities occurring with distorted flow; differentiation with respect to the argument $()$.
--------	--

CHAPTER I

INTRODUCTION

Origin of the Problem

The design of a propeller, compressor blade row, or similar axial flow turbomachinery device is normally based, of necessity, upon the assumption of a steady, axisymmetric inflow. A possible exception to this statement occurs in the design of such items as helicopter rotors where the use of cyclic pitch variation of the blades is employed to compensate for the circumferential variations in the inflow.

In reality, there are many cases in turbomachinery where radially and circumferentially varying distortions or perturbations to the originally assumed inflow velocity exist. Interest in distorted flows of this type may be divided roughly into two classes. The first is characterized as the steady-state reaction of a blade row to a distorted inflow. In this class of problems one generally would be interested either in the reactive force of the blade row caused by the distortion or in the flow that leaves the blade row. The other class of problems is that associated with the unsteady fluid dynamic reactions to distorted inflows.

To a great extent, the unsteady analyses have dealt with the application of non-stationary airfoil theory to

two-dimensional shapes passing through a sinusoidal gust or a viscous wake^{1, 2}. Of interest here has been the fluctuating forces and moments on a two-dimensional airfoil resulting from such disturbances in the flow. The calculations of the forces and moments are then applied to the determination of the amplitude of torsional oscillations of blades.

Extension of this work was performed by Meyer³ in which he determined the time-dependent pressure gradient and velocity on two-dimensional blades of a blade row passing through the viscous wakes of a preceding stage. A further extension of this work was reported by Yeh and Eisenhuth⁴ in which the transient effects were reduced to a quasi-steady analysis involving an equivalent angle of attack of a blade section.

In the strictly steady-state studies, two basic types of distortion - radial⁵ (axisymmetric) and circumferential⁶ (periodic in the peripheral direction) have been examined. Yeh⁷ reported on a study in which he treated on the basis of classical actuator disc approximation, the flow behind a rotor (or stator) blade row due to an arbitrary inlet distortion along both circumferential and spanwise directions. He showed that, in general, the spanwise and the circumferential distortion waves interact, so that the combined influence is not the sum of the influence of the

two simple types of distortions. Yeh's analysis assumed a plane cascade. A need for a three-dimensional analysis of distorted flows in cylindrical coordinates therefore still exists. Methods of handling the three-dimensional aspects of flow in turbomachinery are available^{8, 9, 10}. The application of these to the problem of distorted inflows, however, has not been attempted.

The need for an analysis of flow distortions in cylindrical coordinates is particularly strong in terms of propellers. A specific type of distortion occurs with propellers in the propulsion of underwater bodies. Often it is necessary in the design of underwater bodies to place control surfaces immediately upstream of the propeller. The deflected flow produced by the control surfaces, when actuated, constitutes a flow distortion that is partly carried through the propeller. The propeller tends to straighten the deflected flow, thus reducing the effectiveness of the control surfaces.

Combined with the need for a study of flow distortions in cylindrical coordinates, the practical problem posed by the interaction between control surfaces and propellers on underwater bodies forms the basis for this investigation.

Statement of the Problem and Its Limitations

The purpose of this investigation is, in general, to determine the steady-state reaction of a propeller to

velocity perturbations induced by deflected control surfaces located upstream of the propeller. This is to be accomplished by a theoretical development which will permit the prediction of the velocity perturbations throughout the field and make possible the calculation of forces on the propeller produced by the perturbations. The analysis is restricted throughout to the study of incompressible, inviscid flow. The purpose is further to be accomplished by an experimental wind tunnel program in which the reactive force of the propeller and the velocity pattern at various locations in the field is measured.

Because of the many variables involved in a study such as this, the number of configurations and operating conditions must be limited. The study is first limited to the consideration of two control surfaces, 180 degrees apart, which are both deflected the same amount in a given sideward direction. Mathematically this means that in the circumferential direction a cosine (a zero degree circumferential angle corresponds to the location of one control surface) type distribution of the tangential component of velocity disturbance is considered. Also, with regard to the configuration itself, the propeller and control surfaces are limited to the same hub and tip radius. The number of blades is, however, varied to include 2, 5, and 10-bladed

configurations. The final configuration variable results from the consideration of different spacing distances between control surfaces and propeller. Three spacing distances of 2, 5, and 8 inches are considered.

Although, in the problem of practical interest, the control surfaces and the propeller operate in the radially varying viscous wake of the body, the present study is restricted to those cases with a uniform "primary" velocity. The advance ratio (ratio of forward velocity to the rotational velocity) of the propeller is variable and is varied in the experiments involving propeller force measurements. In the theoretical analysis and in the velocity surveys downstream of the propeller, only the design advance ratio is used. The velocity surveys downstream of the propeller are, in fact, restricted to one propeller configuration, one spacing, one advance ratio, and one angle of attack of the control surfaces. Variation of any of these in the surveys would have involved a prohibitive amount of work.

CHAPTER II

DEVELOPMENT OF THEORY

Formulation of the Problem

The model that was chosen in the formulation of the problem is shown in Fig. 1. There is a given "primary" velocity, V_z , which is in general a function of radius. The primary flow is assumed to be directed axially, external to the cylindrical hub. The action of the control surfaces and the propeller is represented by two actuator discs, Disc A and Disc B respectively. Disc A serves to introduce a flow distortion characterized by a tangential velocity disturbance, v_u , which is a function of radius, r , and of circumferential angle, φ . This disturbance can represent the action of one or more control surfaces.

Disc B represents the action of the propeller. Certain characteristics, consistent with propeller theory, are prescribed for Disc B. These characteristics, in effect, take the time dependency aspect of the problem out of consideration.

The flow field is divided into three separate regions: Region (1) upstream of Disc A; Region (2), between the two discs; Region (3) downstream of Disc B. The solution of the problem involves the determination of the velocity perturbations in all three regions.

The approach* that in general is followed is to start with the equations of motion and continuity equation in cylindrical coordinates, make the assumption of very small velocity and pressure disturbances compared with the primary velocity, and then combine the equations to produce a single differential equation for p , the pressure perturbation. A series solution for this equation is assumed, permitting the derivation of expressions for the velocity perturbations in all regions. The velocity perturbations are obtained from these expressions by proper choice of boundary and matching conditions at the discs.

Solution of Pressure Equation

The equations of motion and continuity equation in cylindrical coordinates were used in Appendix A to derive the following differential equation in pressure perturbation:

$$\bar{V}_z^2 \frac{\partial}{\partial z} \left(\frac{1}{\bar{V}_z^2} \frac{\partial p}{\partial r} \right) + \frac{1}{r} \frac{\partial p}{\partial r} + \frac{\partial^2 p}{r^2 \partial \phi^2} + \frac{\partial^2 p}{\partial z^2} = 0 \quad (1)$$

*This approach to the problem was suggested by Dr. H. Yeh of the University of Pennsylvania.

From the nature of the problem a solution for Equation (1) of the following form can be assumed:

$$p(r, \phi, z) = \sum_m \sum_n a_{mn} R_{mn}(r) e^{\pm k_{mn} z} e^{im\phi} \quad (2)$$

When this solution is applied to Equation (1), the following total differential equation results:

$$\nabla_z^2 \frac{d}{dz} \left(\frac{1}{\nabla_z^2} \frac{dR_{mn}}{dr} \right) + \frac{1}{r} \frac{dR_{mn}}{dr} + \left(k_{mn}^2 - \frac{m^2}{r^2} \right) R_{mn} = 0 \quad (3)$$

For an arbitrarily prescribed $\nabla_z = \nabla_z(r)$, Equation (3) can normally be handled only in a numerical way. If, however, the distribution were given by some power law such as $\nabla_z(r) = cr^\alpha$, Equation (3) could be written as:

$$\frac{d^2 R_{mn}}{dr^2} + \left(\frac{1-2\alpha}{r} \right) \frac{dR_{mn}}{dr} + \left(k_{mn}^2 - \frac{m^2}{r^2} \right) R_{mn} = 0 \quad (4)$$

If, then, a quantity δ_m is defined by:

$$\delta_m^2 = m^2 + \alpha^2 \quad (5)$$

Equation (4) can be written as:

$$\frac{d^2 R_{mn}}{dr^2} + \left(\frac{1-2\alpha}{r} \right) \frac{dR_{mn}}{dr} + \left(k_{mn}^2 + \frac{\alpha^2 - \delta_m^2}{r^2} \right) R_{mn} = 0 \quad (6)$$

which is a Bessel type equation for which the solution is:

$$R_{mn} = r^\alpha Z_{\delta_m}(k_{mn} r) \quad (7)$$

$Z_{\delta_m}(k_{mn} r)$ is, in general, a linear combination of Bessel functions of both kinds. Even though m and α are integers, δ_m will not generally be an integer. The solution, therefore, will include a linear combination of Bessel functions of the first kind with like positive and negative orders.

If the primary velocity, V_z , were considered as uniform, that is:

$$V_z = \text{constant} \quad (8)$$

Equation (3) would reduce to:

$$\frac{d^2 R_{mn}}{dr^2} + \frac{1}{r} \frac{dR_{mn}}{dr} + \left(k_{mn}^2 - \frac{m^2}{r^2} \right) R_{mn} = 0 \quad (9)$$

This is simply Bessel's equation for which the solution is, in general, $Z_m(k_{mn}r)$. In other words:

$$R_{mn}(r) = Z_m(k_{mn}r) = J_m(k_{mn}r) + \beta_{mn} Y_m(k_{mn}r) \quad (10)$$

where:

$J_m(k_{mn}r)$ = Bessel function of the first kind

$Y_m(k_{mn}r)$ = Bessel function of the second kind

β_{mn} = A constant depending on m and n

k_{mn} = The characteristic values or Eigenvalues

The problem that has been chosen is the one in which V_z is considered constant. This corresponds to the case of a "free-stream" condition as opposed to the case where the control surfaces and propeller operate in the boundary layer of a body.

Velocity Perturbations

Having obtained the solution of the pressure perturbation equation, Equation (1), the component velocity perturbations, v_r , v_u , and v_z can be derived. This is accomplished by first writing Equation (2) for each of the three regions, substituting into the linearized equations of motion, and integrating to determine each of the three component velocity perturbations for each

region. The details of this derivation and all the resulting expressions are included in Appendix B. The velocity perturbations are given by Equations (B-2), (B-3), and (B-4).

The ability to calculate the velocity perturbations in all regions becomes one of determining the coefficients A_{mn} , B_{mn} , C_{mn} , and D_{mn} and certain of the functions of integration (discussed in a later section) that evolved. The procedure for finding these unknowns is one of considering the physics of the problem.

Boundary Conditions

It is necessary to apply a boundary condition first of all at the hub. The radial component of velocity perturbation at the hub must be zero which, upon examination of Equations (B-2), (B-3), and (B-4), means that the slope of the Bessel function, $Z'_m(k_{mn}r)$, must be zero.

It is not necessary to apply a condition at $r = \infty$. All the velocity perturbations can be expected to decrease to zero as $r \rightarrow \infty$ because the Bessel functions and their slopes all decrease to zero as $r \rightarrow \infty$.

It is still necessary to apply a condition at some outer radius. The tangential component of velocity perturbation must be zero at such a radius. One would expect that this would occur at the tip radius

of the control surfaces. It will be seen later from velocity survey data that this is not exactly true and that some radius slightly greater than the tip radius must be chosen. This condition, whatever the radius, leads to the stipulation that the Bessel function itself must be zero at that radius.

The boundary conditions that were just stated permit the determination of the Eigenvalues for the problem. In equation form, the two conditions can be written:

$$Z'_m(k_{mn}r_h) = J'_m(k_{mn}r_h) + \beta_{mn} Y'_m(k_{mn}r_h) = 0 \quad (11)$$

$$Z_m(k_{mn}r_o) = J_m(k_{mn}r_o) + \beta_{mn} Y_m(k_{mn}r_o) = 0$$

where r_h is the hub radius and r_o is the outer radius.

Solving this set of equations leads to the relation:

$$J_m(k_{mn}r_o) Y'_m(k_{mn}r_h) - J'_m(k_{mn}r_h) Y_m(k_{mn}r_o) = 0 \quad (12)$$

which can be further altered by recurrence formulae to read:

$$\begin{aligned} J_m(k_{mn}r_o) [Y_{m-1}(k_{mn}r_h) - Y_{m+1}(k_{mn}r_h)] \\ - Y_m(k_{mn}r_o) [J_{m-1}(k_{mn}r_h) - J_{m+1}(k_{mn}r_h)] = 0 \end{aligned} \quad (13)$$

By obtaining the correct combinations of values for the Bessel Functions, the Eigenvalues, k_{mn} , can be determined. Knowing the Eigenvalues, it is then possible to obtain from one of the Equations (11), the values of β_{mn} . For instance:

$$\beta_{mn} = - \frac{J_m(k_{mn} r_0)}{Y_m(k_{mn} r_0)} \quad (14)$$

Functions of Integration

The functions that resulted from integration when determining the expressions for the velocity perturbations can be analyzed and, by virtue of the physical problem being considered, certain conclusions can be drawn as to their existence.

In Region (1) one could ordinarily assume that as $z \rightarrow -\infty$ all velocity perturbations would approach zero. This consideration necessitates that:

$$f_1(r, \varphi) = g_1(r, \varphi) = h_1(r, \varphi) = 0 \quad (15)$$

because the rest of the expressions for the velocity perturbations in Region (1) go to zero as z goes to $-\infty$.

In Region (2) the analysis of the additional functions is more complicated. Consider, first, the function, $g_2(r, \varphi)$. It can be reasoned that this additional function

represents that part of the solution that is lost when $m = 0$ (See Equations (B-3)). As such, $g_2(r, \varphi) = g_2(r)$ would represent the mean "swirl" that is produced by the control surfaces and is therefore a function only of radius. For the case of two control surfaces deflected in the same side direction the net swirl is zero. In other words, for such a special case,

$$g_2(r) = 0 \quad (16)$$

The function $h_2(r, \varphi)$ can in general exist. On the other hand, when Equations (B-3) are substituted into the equation of continuity, Equation (A-7), and the boundary condition, $v_r = 0$ at $r = r_h$, is used it is observed that $f_2(r, \varphi)$ must necessarily be zero, regardless of whether $g_2(r)$ was zero or not.

In Region (3) the function $g_3(r, \varphi)$ could again represent the mean swirl leaving the propeller and would, therefore, be a function only of radius. A mean swirl would exist if the propeller were a "thrusting propeller", that is, in the absence of a flow distortion the propeller were producing a thrust. This function could, therefore, be specified as a characteristic of the propeller. If the propeller were a "nonthrusting propeller" $g_3(r)$ would be zero.

The function, $h_3(r, \varphi)$, could in general exist but would be determined in some manner by the function $g_3(r)$. Because of this, it would likewise be a function only of radius. This is consistent with standard propeller theory which deals only with circumferentially mean values. The function, $f_3(r, \varphi)$, would again have to be zero to satisfy the continuity equation.

Unknowns

To summarize at this point, one can list the following as the unknowns of the problem:

- | | |
|-------------|----------------------|
| 1. A_{mn} | 5. $h_2(r, \varphi)$ |
| 2. B_{mn} | 6. $g_3(r)$ |
| 3. C_{mn} | 7. $h_3(r)$ |
| 4. D_{mn} | |

The functions listed can also be written in series form with appropriate coefficients. The coefficients can then be considered as the unknowns permitting easier handling of the solution. Several of the unknowns can be determined directly while the others must be determined as the unknowns of a set of simultaneous equations. The seven relations necessary to determine these unknowns are listed below and discussed in turn in the seven following sections.

1. Specification of flow distortion at Disc A
2. Specification of propeller mean swirl
3. Propeller normality condition
4. Continuity at Disc B
5. Continuity at Disc A
6. Relation between tangential velocity perturbations at Disc A
7. Relation between tangential and axial velocity perturbations at Disc B.

Specification of Flow Distortion at Disc A. The distortion introduced by deflected control surfaces is characterized by the distribution of the tangential velocity perturbation, v_{u_2} , immediately downstream of the control surfaces. It is possible to calculate this perturbation by use of existing wing theories. On the other hand, since v_{u_2} is the starting point of the calculation and can be arbitrarily assigned, it would be physically more meaningful to actually measure the distribution of distortion and use that in the calculation. This is the approach that was followed in this study.

The distribution of v_{u_2} in the circumferential and radial directions, however determined, constitutes an input to the problem. What changes occur in all the component velocity perturbations through the field due

to the action of the propeller constitutes the output to the problem.

Having arrived at a distribution of v_{u_2} immediately behind Disc A, a Fourier-Bessel type analysis can be made. This is accomplished by first letting:

$$\frac{\tilde{u}_2}{\tilde{V}_2} = \sum_m \sum_n \frac{P_{mn}}{k_{mn} r} Z_m(k_{mn} r) e^{im\varphi} \quad (17)$$

at the $z = -d$ location, i.e., immediately downstream of Disc A. The coefficient, P_{mn} , can then be found by use of:

$$\frac{P_{mn}}{k_{mn}} = \frac{1}{\pi N_{mn}} \int_{r_h}^{r_0} r Z_m(k_{mn} r) dr \int_{-\pi}^{\pi} (r \cdot \frac{\tilde{u}_2}{\tilde{V}_2}) e^{-im\varphi} d\varphi \quad (18)$$

where N_{mn} is the normalizing factor and is given by:

$$N_{mn} = \int_{r_h}^{r_0} r [Z_m(k_{mn} r)]^2 dr = \frac{r_0^2}{2} [Z_{m+1}(k_{mn} r_0)]^2 + \frac{m^2 - k_{mn}^2 r_h^2}{2 k_{mn}^2} [Z_m(k_{mn} r_h)]^2 \quad (19)$$

v_{u_2} is also given by Equation (B-3) which allows the writing of the following relation for a single two-dimensional wave in r and φ :

$$P_{mn} = -im B_{mn} e^{-k_{mn} d} + im C_{mn} e^{k_{mn} d} \quad (20)$$

Since P_{mn} is known, this is simply a relation between C_{mn} and B_{mn} which can be written as:

$$B_{mn} = C_{mn} e^{2k_{mn}d} + \frac{i}{m} P_{mn} e^{k_{mn}d} \quad (21)$$

B_{mn} and C_{mn} are, in general, complex.

Specification of Propeller Mean Swirl. As stated previously, the function $g_3(r)$ is used to represent the mean swirl introduced by a thrusting propeller. This function exists when there is a thrusting propeller regardless of whether there is a distortion or not. $g_3(r)$ can therefore be specified independently of the rest of the problem and can be defined as:

$$g_3(r) = \sum_l L_{ol} Z_o(k_{ol}r) \quad (22)$$

Knowing $g_3(r)$, the coefficients, L_{ol} , can be determined in a manner similar to that given by Equation (18), but without the trigonometric integral included. The Eigenvalues could be determined with the same boundary conditions used previously.

In the specification of $g_3(r)$ it is necessary to resort to propeller theory. Fig. 2 illustrates a typical velocity diagram for a particular blade section. The

diagram demonstrates the action of a propeller section at normal operating conditions in the absence of a flow distortion.

The following definitions apply:

w_a = Component of induced velocity in the z direction

w_t = Component of induced velocity in the circumferential direction

V_e = Relative velocity at the blade section
(midway between regions 2 and 3)

V_z = Primary velocity or free-stream velocity

x = Relative radius $\left(= \frac{r}{R_p} \right)$

R_p = Propeller Radius

J = Propeller advance ratio $\left(= \frac{V_z}{2n R_p} \right)$

n = Rotational speed (rps)

θ = Angle of resultant velocity at the propeller blade section

The numbers 2 and 3 on the diagram in Fig. 2 refer to conditions immediately upstream and downstream of the propeller disc respectively. This indicates that the full value of the tangential component of induced velocity, $2w_t$, is reached immediately behind the disc. Right at the blade section half the value or just w_t is assumed to exist.

On either side of the disc, the axial component of induced velocity is w_a . Upstream at $-\infty$ the axially induced velocity is zero. Downstream at $+\infty$ the value has reached $2w_a$.

For a specific propeller the function, $g_3(r)$, can be given at a particular radius by:

$$g_3(r) = \frac{2K w_T}{V_z} = \frac{1}{2} \cdot \frac{CB}{2\pi r} \cdot \frac{V_e}{V_z} c_l \quad (23)$$

where:

K = Goldstein averaging factor¹¹ (function of r, J, B)

B = Number of blades

c = Section chord length

c_l = Section lift coefficient, $= c_{l_0}$, the lift coefficient at zero angle of attack, when the section chord is aligned with V_e .

Propeller Normality Condition. A condition is available from propeller theory for the determination of $h_3(r)$. The condition of normality states that the resultant induced velocity at infinity is normal to the trailing vortex sheet. In terms of the velocity diagram in Fig. 2, this means:

$$\frac{2 \frac{w_T}{V_z}}{2 \frac{w_a}{V_z}} = \frac{1 + 2 \frac{w_a}{V_z}}{\frac{\pi x}{J} - 2 \frac{w_T}{V_z}} \quad (24)$$

Making use of Equations (23) and (24) and dropping higher order terms:

$$\kappa \frac{\bar{w}_a}{V_z} = \frac{1}{2} \left(\frac{\pi x}{J} \right) g_3(r) \quad (25)$$

The axial component of induced velocity is thus given in terms of the function $g_3(r)$. It is convenient to define the function, $h_3(r)$, as:

$$h_3(r) = \kappa \frac{\bar{w}_a}{V_z} = \frac{1}{2} \left(\frac{\pi x}{J} \right) g_3(r) \quad (26)$$

Because $h_3(r)$ will not vary with a change in axial distance, this definition does not completely follow propeller theory. In other words, $h_3(r)$ will not reach the full value of $2\bar{w}_a$ at $+\infty$. This results from the linearization process in the problem in which the perturbations are carried along by the primary velocity, V_z . It does not appear to be a serious source of concern in handling the problem because $h_3(r)$ actually drops out of the problem when later relations are applied.

The function, $h_3(r)$ with the help of Equation (23) can be written as:

$$h_3(r) = \frac{1}{2} \left(\frac{\pi x}{J} \right) \left(2\kappa \frac{\bar{w}_E}{V_z} \right) = \frac{1}{2} \left(\frac{\pi x}{J} \right) \cdot \frac{1}{2} \cdot \frac{CB}{2\pi r} \cdot \frac{V_c}{V_z} C_L \quad (27)$$

As in the case of $g_3(r)$, it can also be put in series form:

$$h_3(r) = \sum_{\ell} I_{0\ell} Z_0(k_{0\ell} r) \quad (28)$$

where $h_3(r)$ is given by Equation (27) when performing a numerical analysis.

Continuity at Disc B. Continuity at Disc B means simply that at $x = d$:

$$\psi_{z_2} = \psi_{z_3} \quad (29)$$

This relation involves the functions of $h_3(r)$ and $h_2(r, \varphi)$. $h_3(r)$ has already been defined in Equation (28). If the case of a nondistorted flow is considered, $h_2(r, \varphi)$ must actually be equal to $h_3(r)$ by virtue of Equation (29). It is therefore convenient to define $h_2(r, \varphi)$ in the following manner:

$$h_2(r, \varphi) = \sum_m \sum_n O_{mn} Z_m(k_{mn} r) e^{im\varphi} + \sum_{\ell} I_{0\ell} Z_0(k_{0\ell} r) \quad (30)$$

Using, now, the v_z equations from Equations (B-3) and (B-4) and employing Equations (28) and (30), continuity at Disc B yields for a single two-dimensional wave in r and φ :

$$D_{mn} = (e^{4k_{mn}d} + 1) C_{mn} - e^{k_{mn}d} O_{mn} + \frac{i}{m} e^{3k_{mn}d} P_{mn} \quad (31)$$

B_{mn} was eliminated in this equation through use of Equation (21).

Continuity at Disc A. As in the case of Disc B, continuity can be employed at Disc A so that at $z = -d$:

$$v_{z_1} = v_{z_2} \quad (32)$$

Again the function $h_2(r, \varphi)$ is involved. In the case of nondistorted flow, Equation (32) means that there must be a function $h_1(r)$:

$$h_1(r) = \sum_l I_{0l} Z_0(k_{0l} r) \quad (33)$$

It had previously been reasoned that $h_1(r, \varphi)$ was zero. If the action of the propeller could be more accurately represented, $h_1(r, \varphi)$ would actually be zero. The action of the propeller with regard to the axially induced velocity is thus represented as not varying in the axial direction.

Using the v_z equations from Equations (B-2) and (B-3) and employing Equations (30) and (33), continuity at Disc A yields for a single wave:

$$O_{mn} = 2 C_{mn} e^{k_{mn} d} + \frac{i}{m} P_{mn} - e^{-k_{mn} d} A_{mn} \quad (34)$$

Again, B_{mn} was eliminated through use of Equation (21).

Relation between Tangential Velocity Perturbations at Disc A. Consistent with the linear aspects of the problem, a relation of the following form is needed:

$$\frac{\bar{v}_{u_2}}{\bar{V}_2} = A + B \frac{\bar{v}_{u_1}}{\bar{V}_2} \quad (35)$$

One of the choices that can be made is that $A = 0$ and $B = 1$. In other words:

$$\frac{\bar{v}_{u_2}}{\bar{V}_2} = \frac{\bar{v}_{u_1}}{\bar{V}_2} \quad (36)$$

This is contrary to the normal concept of an actuator disc in which the tangential component of velocity changes discontinuously across the disc. If this relation is used, the disc location could be thought of more as a place which is mathematically convenient for specifying a distortion, but which involves no discontinuous changes. This might not be the best type of relation to use for the physical case under consideration, where the tangential velocity does change abruptly. Equation (36) might best be used where a distortion is introduced farther upstream but which is measured at a location corresponding to that of Disc A.

Another approach that might be considered is derived by looking at the distribution of induced velocity about

a wing. The induced velocity at a particular point is composed of contributions from both the bound and trailing vortex systems. If one considered the contribution of a bound vortex alone, one could write:

$$\overline{v}_{u_2} = - \overline{v}_{u_1} \quad (37)$$

If, on the other hand, the contribution of the trailing vortex system is considered alone, the following could be written:

$$\overline{v}_{u_2} = \overline{v}_{u_1} = w \quad (38)$$

The w is the normal designation given to the induced velocity at the wing due to the trailing vortex system. A value of $2w$ is induced by this system at infinity.

What occurs in reality is a combination of these two effects. One could say, for instance:

$$\frac{\overline{v}_{u_2}}{\overline{V}_Z} = \frac{w}{\overline{V}_Z} + \frac{\overline{v}_{BV}}{\overline{V}_Z} \quad (39)$$

and

$$\frac{\overline{v}_{u_1}}{\overline{V}_Z} = \frac{w}{\overline{V}_Z} - \frac{\overline{v}_{BV}}{\overline{V}_Z} \quad (40)$$

where v_{BV} is the velocity due to the bound vortex. A solution of these equations yields:

$$\frac{v_{u_2}}{V_z} = 2 \frac{w}{V_z} - \frac{v_{u_1}}{V_z} \quad (41)$$

If the following definition is made:

$$Q = \frac{w}{v_{u_2}} \quad (42)$$

then

$$(1 - 2Q) \frac{v_{u_2}}{V_z} = - \frac{v_{u_1}}{V_z} \quad (43)$$

There is a question of how Equation (43) would be used. Actually v_{u_2} and v_{u_1} could be measured in lateral planes just aft and just ahead of the control surfaces. Further, w at the wing can be related to the lift of the wing or the distribution of lift along the span. Equation (43) could then merely be used as a check on the v_{u_2} and v_{u_1} measurements.

In any event, the knowledge of two of the variables w , v_{u_2} , or v_{u_1} yields the third. The choice of how this is done depends upon the circumstances under which the problem is being solved.

Let it be assumed for the present case that the v_{u_1} distribution is known and is related to v_{u_2} through

Equation (43). The coefficient A_{mn} can then be determined directly. From Equation (B-2), v_{u_1} at $z = -d$ can be written as:

$$\frac{v_{u_1}}{V_z} = -\sum_m \sum_n \frac{im}{k_{mn} r} A_{mn} Z_m(k_{mn} r) e^{-k_{mn} d} e^{im\varphi} \quad (44)$$

A_{mn} can then be found in the same manner that P_{mn} was determined:

$$\frac{im}{k_{mn}} e^{-k_{mn} d} A_{mn} = -\frac{1}{\pi N_{mn}} \int_{r_n}^{r_o} r Z_m(k_{mn} r) dr \int_{-\pi}^{\pi} \left(r \frac{v_{u_1}}{V_z} \right) e^{-im\varphi} d\varphi \quad (45)$$

where N_{mn} is defined in Equation (19). For ease in later application, it is convenient to define a coefficient, A'_{mn} , which is of the same form as P_{mn} :

$$A'_{mn} = im e^{-k_{mn} d} A_{mn} \quad (46)$$

Relation between Tangential and Axial Velocity

Perturbations at Disc B. If a distortion were introduced by Disc A, the velocity diagram shown in Fig. 2 would be altered in a manner as represented in Fig. 3. In Fig. 3 part of the altered diagram is superimposed over the original velocity diagram of Fig. 2. It should be noted that v_{z_2} in the diagram includes both the induced velocity w_a and an increment of axial velocity due to the

original disturbance and the reaction of the propeller to that disturbance. Using this velocity picture as a basis, a linear relation between v_{u_2} , v_{z_2} , and v_{u_3} of the following form can be derived:

$$\frac{v_{u_3}}{V_z} = K(r) + M(r) \frac{v_{z_2}}{V_z} + N(r) \frac{v_{u_2}}{V_z} \quad (47)$$

The derivation of Equation (47) and expressions for $K(r)$, $M(r)$, and $N(r)$ are given in Appendix C. The case that will be studied is that of a nonthrusting propeller which causes the $K(r)$ term in Equation (47) to be zero. It is also shown by virtue of Equation (C-29), that whether or not a propeller is thrusting has no effect on the final results. Terms involving the normal action of the propeller cancel each other in Equation (47). For calculating the effects of flow distortions, therefore, one can always consider the propeller as nonthrusting.

Solution of Unknown Coefficients

Enough relations are now available to determine all the unknowns that were previously listed. Of those originally listed $h_3(r)$ and $g_3(r)$ can be determined independently of the rest of the problem. It was also assumed that a knowledge of v_{u_1} just upstream of Disc A was available so that the coefficient A_{mn} could be

determined directly. This left to be determined the coefficients B_{mn} , C_{mn} , D_{mn} , and O_{mn} . The coefficient O_{mn} replaces the unknown function $h_2(r, \varphi)$.

The first of the equations available for the solution is Equation (21). This has already been used in eliminating B_{mn} from succeeding equations. Two of remaining three equations that are necessary are Equations (31) and (34). The third equation is Equation (47). No simple relation between coefficients can be derived from Equation (47), however. Because the $K(r)$, $M(r)$, and $N(r)$ terms are not constants but vary with radius, it is necessary to define additional coefficients which further complicate the solution. The details of getting Equation (47) in a suitable form for solution is presented in Appendix D. The equation is solved for the coefficient, C_{mn} .

The remaining unknown, B_{mn} , O_{mn} , and D_{mn} , can be found in turn by substituting the values of C_{mn} in Equations (21), (34), and (31) respectively.

Equation (21), after substituting for C_{mn} in the form of Equation (D-11), will read:

$$B_{mn} = E e^{2k_{mn}d} + i \left(\frac{1}{m} P_{mn} e^{k_{mn}d} - F e^{2k_{mn}d} \right) \quad (48)$$

If similar substitutions are made in Equations (34) and (31), the following equations will result:

$$O_{mn} = 2E e^{k_{mnd}} + i \left(\frac{1}{m} P_{mn} - 2F e^{k_{mnd}} + \frac{1}{m} A'_{mn} \right) \quad (49)$$

$$D_{mn} = e^{k_{mnd}} S E + i \left(\frac{1}{m} e^{k_{mnd}} U P_{mn} - e^{k_{mnd}} S F - \frac{1}{m} e^{k_{mnd}} A'_{mn} \right) \quad (50)$$

S and U are defined in Equation (D-5).

CHAPTER III

MEASUREMENT OF FLOW DISTORTION

Experimental Setup

The flow distortion was determined experimentally in this investigation in the subsonic wind tunnel at the Garfield Thomas Water Tunnel of the Ordnance Research Laboratory. This tunnel¹² has an octagonal test section with a nominal diameter of 48 inches.

The same basic model was used for both the measurement of the flow distortion and for the reaction of the propeller to the flow distortion. However, in the distortion measurements, there was no need to have a propeller or force sensing instrumentation. Therefore an "interim" model was used.

The essential components of the interim model include an 8-inch diameter housing supported by a streamlined strut, a 5-inch diameter cylindrical sleeve (hub), two control surfaces, a wood nose section, and a supporting stationary shaft. Views of the model can be seen in Figs. 4 and 5.

The 8-inch diameter housing is, in reality, a torpedo model with its upstream and downstream ends reversed. Normally it will house the electric motors to turn the propellers. In this setup, it is used primarily to

support the rest of the model. In the final model, it is also used to house a twenty horsepower motor.

The control surfaces are mounted on the upstream end of the model. The surfaces are, therefore, operating in a uniform flow or free-stream condition. The control surfaces are independently moveable over a range of approximately plus or minus six degrees.

The design of the control surfaces consists of a tapered planform in which the chord length varies linearly from 4.66 inches at the hub to 3.00 inches at the tip. The section shapes are standard NACA 65-009 airfoils all along the span. This designation indicates a symmetrical section with a maximum thickness-to-chord ratio of 0.09.

Instrumentation

The measurement of the velocity components was accomplished by use of a three-dimensional pitot-type probe. The probe is shown in Figs. 4 and 5. It is a commercially available instrument, manufactured by the United Sensor and Control Corporation, Glastonbury, Connecticut and is designated as a DC-120 type probe.

The probe incorporates five pressure holes, the center hole giving a measure of total head. Two horizontally orientated holes indicate variations in yaw angle and two vertically orientated holes indicate

variations in pitch angle. The pressure holes are connected by tubes to a manometer board.

The probe is mounted on a traversing unit, shown in Fig. 5, which permits orientation of the probe in the vertical and lateral directions for a particular lateral plane. The traversing device also permits the changing of the pitch orientation of the probe. A dial with a vernier device makes it possible to read changes in pitch angle to about 0.1 degree.

Calibration curves were available with the probe but were found inadequate for the accuracy of measurements that were needed. Calibration of the probe was, therefore, performed in the wind tunnel, taking into account the change in yaw angle indication due to the bending of the probe shaft.

The procedure for using the probe is to orientate the probe in the desired location, change the pitch of the probe until the manometer readings associated with pitch are balanced, and then read the pitch angle and the level of the rest of the manometer tubes. Calibration curves relate the manometer readings to the yaw angle and to the resultant velocity. With the resultant velocity, the yaw angle, and the pitch angle known, the components of velocity in the radial, circumferential, and axial directions can be calculated. The manometer readings of

the probe were referenced to a tunnel pitot tube so that results are given as velocity ratios.

Experimental Procedure

The purpose in making the velocity surveys was to learn the velocity perturbations in planes just upstream and downstream of the control surfaces and from these to determine the coefficients A_{mn} and P_{mn} in the problem. Two such planes were chosen and one quadrant thoroughly surveyed in each plane. Points in neighboring quadrants were checked to make sure of symmetry. The assumption was made that the distribution of the disturbance would have the same form in each quadrant. Except for some slight variations near the control surfaces, which were within the accuracy of the measurements, this assumption was experimentally verified.

Because of the physical limitations on positioning the probe, it was necessary to take measurements with the control surface placed first in a vertical plane and then rotated 90 degrees to lie in a horizontal plane. This allowed a full coverage of points in a single quadrant.

The proximity of the probe to the trailing edge of the control surface gave rise to effects traceable to the finite shape of the airfoil sections. The wedge formed by the trailing edge of each section influences the flow in such a way that it produces tangential

components of velocity in opposite directions on either side of the trailing edge. This means that there is a rapid change in the tangential components when passing circumferentially by the trailing edge. The same effect occurs at the leading edge. This effect occurs whether or not the surfaces are deflected. At angular locations closer to the trailing edge, part of the effect might be traceable to the viscous wake shed by the surface. Immediately downstream of the trailing edge the low velocity region in the wake is replenished by fluid from outside the wake, thereby producing tangential components in opposite directions on either side of the trailing edge.

Because the interest is solely in the perturbations caused by the deflection of the control surfaces, it seemed advisable to subtract the effects of finite shape from the measurements. It is also likely in measurements of this type that other extraneous velocity perturbations are already present even when the control surfaces are at zero angle of attack. The procedure that was followed was to take measurements with the control surfaces deflected and at zero angle and subtract the readings to obtain the net perturbations.

Experimental Results

Because of the great amount of time necessary to make the velocity surveys, measurements were made for

only the 0-degree and 3-degree angle of attack cases. These were performed at a nominal tunnel speed of 100 feet per second. A plot of typical experimental results are shown in Fig. 6. This shows the discontinuous change in tangential velocity that occurs when traversing past the trailing edge of the control surface. One can also note the increment of velocity that exists between the 0-degree and 3-degree cases. This increment stays roughly the same for corresponding points on either side of the trailing edge.

Because the tangential components of velocity are the ones that constitute the input to the problem, these data were plotted and cross-plotted several times to insure smoothness of the distribution curves in both the radial and tangential directions. The resulting curves of v_{u_1} and v_{u_2} are shown in Figs. 7 and 8 respectively. Figs. 9, 10, 11, and 12 are plots of the experimentally measured values of v_{r_1} , v_{r_2} , v_{z_1} , and v_{z_2} respectively.

CHAPTER IV

MEASUREMENT OF PROPELLER REACTION TO A FLOW DISTORTION

Experimental Setup

The measurement of the reaction of a propeller to a distorted inflow consisted in measuring the reactive force of the propeller and in surveying the velocity field leaving the propeller. Views of the model used for these tests are shown in Figs. 13 and 14. The changes in the model from the interim model included addition of a propeller, variable spacing between the propeller and control surfaces, an electric motor within the main housing to power the propeller, and instrumentation to measure the side force of the control surfaces and the reactive force of the propeller.

Propeller Design

The propeller was designed to have different numbers of blades (2, 5, and 10). This is possible because the propeller fabrication process at the Garfield Thomas Water Tunnel is one of making individual blades and mounting them on a hub. Hub blanks can be inserted when blades are removed.

The hub and tip diameters of the propeller are the same as those of the control surfaces. The chord length and thickness ratios of the blades were varied linearly from values of 3.0 inches and .0900 at the hub to 3.25 inches and .0775 at the tip. Symmetrical NACA Series 16 airfoils were used throughout.

The advance ratio ($J = V_z/nD$) of the propeller was chosen to be 2.0. This is a representative advance ratio for the propulsion of underwater bodies.

Instrumentation

The force measurements for both the control surfaces and propeller were done with electrical strain gages. Sketches of the main features of the strain-gaged assemblies are shown in Fig. 15. The strain gages in this application are used as transducers rather than purely strain measuring devices. Calibration was performed statically with known weights. It was necessary, because of the very small forces that were measured and the drift in the readings, to calibrate before and after each run.

The readings were taken on a Leeds and Northrup Speedomax recorder. The rpm of the propeller was measured with a Hewlett Packard electronic counter.

The same three-dimensional probe used with the interim model was used for the velocity surveys downstream of the propeller.

Experimental Procedure

The force measurements were made over a wide range of conditions. The number of blades was varied to include 2, 5, and 10 blades. For each one of these propellers the spacing between propeller and control surfaces ($\approx 2d$) was varied over values of the ratio, $\frac{2d}{R_p}$, of 0.267, 0.667, and 1.067. These distances were measured approximately from the trailing edge of the control surface at the hub to the leading edge of the propeller.

The advance ratio of the propeller and the angle of attack of the control surfaces were also varied. Angles of 0, +3, +6, and -3 degrees were used. The procedure followed was to zero the recorder at the 0 angle of attack, change the angle quickly to one of the three angles mentioned, take the reading, and then return to a zero angle to see if there was a return to a zero reading. This technique was again necessary because of the very small forces and the drift in the readings and was made possible by a simple angle of attack changing device. This device consisted simply of an internal yoke connecting the two control surfaces which was held at prescribed positions by detents. By pushing or pulling on this yoke with a long rod, the position could be changed. The rod was inserted through a small hole in the wind tunnel and then through

another hole in the wood nose of the model. This latter hole is visible in Fig. 14.

The velocity surveys were taken in a plane immediately behind the propeller and in one about nine inches downstream of the propeller. The same procedure used in the previous surveys was followed here.

Force Measurement Results

For convenience and ease of handling the forces measured for the propeller and control surfaces were reduced to nondimensional coefficient form. The type of coefficient used is defined by:

$$C_f = \frac{F}{\frac{1}{2} \rho \bar{V}_z^2 \frac{\pi D_p^2}{4}} \quad (51)$$

where:

F = a force

ρ = mass density of air

D_p = propeller diameter

Coefficients defined in this manner for the side force of the control surfaces, side force of the propeller, and vertical force of the propeller are designated C_{cs} , C_H , and C_V respectively. The side force direction is taken as perpendicular to the longitudinal plane in which the control surfaces lie. The vertical force direction is

parallel to this plane. Plots of these coefficients for varying conditions of numbers of blades, spacings, advance ratios, and control surface angle of attack are shown in Figs. 16 through 24. It will be observed that the variation with advance ratio is very small. The greatest changes appear to occur with the vertical force coefficient of the propeller.

To study how the force coefficients vary with angle of attack of the control surfaces, plots were made for a constant value of advance ratio. The advance ratio chosen for these plots is the design advance ratio, $J = 2.0$. The resulting curves are seen in Figs. 25 through 33. They appear to be essentially linear. Because of the linearity, comparisons can be made at any angle of attack. An angle of +3 degrees was chosen and the coefficients plotted versus spacing distance in Fig. 34. Practically no difference in coefficients is noticed with spacing distance.

For any spacing then a comparison between numbers of blades can be made. This was done and is shown in Fig. 35. One of the curves shows the percentage of side force cancellation by the propeller for different numbers of blades.

Results of Velocity Survey

The results of the velocity surveys are helpful in giving some idea of how much of the original distortion passes through the propeller. Figs. 36 and 37 (for $\frac{z}{R_p} = 0.133$ and 1.200) show how the tangential disturbance resulting from a 3 degree control surface angle has changed for the 10-bladed, $\frac{2d}{R_p} = 0.267$ spacing case. No attempt was made to survey downstream of the propeller for any other cases. Because of the danger of the probe being struck by the propeller, no surveys were made just upstream of the propeller.

CHAPTER V

THEORETICAL COMPUTATIONS

Eigenvalue Calculations

The computations proceeded along the lines already discussed in Chapter II. It was necessary to go to machine computation because of the difficulty and length of the calculations. For this purpose the IBM 1620 computer at the Garfield Thomas Water Tunnel was used in developing and proving the programs. The IBM 7074 computer of the Pennsylvania State University Computer Center was used for the bulk of the actual computations. Details of how certain types of calculations were handled are presented in Appendix E. Detailed Fortran programs and flow charts for all computations performed in this investigation are available in Reference 20.

The first computations undertaken were of the Eigenvalues. These were found by use of Equation (12). The procedure that was necessary was to choose successive values of k_{mn} until Equation (12) was satisfied. This procedure was eventually incorporated in a computer program which included a Bessel function subroutine. The β_{mn} constants were calculated from Equation (14).

The choice of how many orders of Bessel functions and how many Eigenvalues within an order resulted from examination of the A'_{mn} and P_{mn} calculations. The A'_{mn} and P_{mn} values were calculated from Equations (45) and (18) respectively. The convergence of Equation (17) was rather slow with the distribution in Fig. 8 and a choice of 16 orders and 16 Eigenvalues for each order was made. The v_{u_1} series of Equation (B-2) converged more rapidly. The distributions that resulted from the chosen number of terms are shown in Figs. 40 and 43. The calculated v_{u_2} values, although not so close to the measured distribution as the v_{u_1} case, were considered sufficiently close to be meaningful.

Propeller Properties

Before calculating C_{mn} from Equation D-9, the functions $M(r)$ and $N(r)$ had to be calculated. The properties of the propeller described in Chapter IV were used for this purpose. The slopes of the lift curves as well as the K values for the 2 and 5-bladed propellers were obtained from Reference 12. The values for the 10-bladed case were calculated as the more approximate Prandtl tip loss factor:

$$K = \frac{2}{\pi} \cos^{-1} \exp \left[-\frac{B}{2} \cdot \frac{(1 - \sqrt{R_P})}{\sin \phi_T} \right] \quad (52)$$

In each case, corrections for finite hub effects¹³ were applied to the K values.

The resulting distributions of $M(r)$ and $N(r)$ are shown in Figs. 38 and 39. The summations based on $M(r)$ and $N(r)$ necessary for the C_{mn} calculations are given in Table I. Twenty terms were used in these summations.

TABLE I

Summation Values for α_{1l} , γ_{1l} , λ_{1l}

B	$\sum_l \alpha_{1l}$	$\sum_l \gamma_{1l}$	$\sum_l \lambda_{1l}$
2	.4342	.2611	.4632
5	.8351	.0584	.4632
10	1.0662	-.0886	.4632

Computing Accuracy

The computation of the C_{mn} coefficients and the other unknown coefficients introduced some questions of accuracy. The determination of E and F (Equations (D-12) and (D-13) involved the subtraction or addition of some very large numbers. The large numbers resulted from the large values of the exponentials when the spacing distance and the order of the Bessel functions became large. The difficulties were felt in the determination of both the real and imaginary parts of C_{mn} and consequently in the

other coefficients which depend upon C_{mn} . Values of E and F , when obtained directly from Equation (D-9), were often extremely high. To alleviate this problem Equations (D-12) and (D-13) were rewritten. In the case of Equation (D-12) some of the very large terms cancelled. Equation (D-13) was put in such a form that, for exponentials beyond a certain size, the expression could be simplified. The manner in which these equations were altered appears in Appendix F. In Appendix F it is shown that for sufficiently high values of $e^{k_{mn}d}$ the term F reduces to:

$$F = e^{-k_{mn}d} \frac{P_{mn}}{m} \quad (53)$$

When Equation (53) is substituted in Equations (48), (49), and (50) the expressions for B_{mn} , O_{mn} , and D_{mn} become:

$$B_{mn} = E e^{2k_{mn}d} \quad (54)$$

$$O_{mn} = 2 E e^{k_{mn}d} + i(A'_{mn} - P_{mn}) \frac{1}{m} \quad (55)$$

$$D_{mn} = e^{k_{mn}d} 5 E + i(P_{mn} - A'_{mn}) \frac{e^{k_{mn}d}}{m} \quad (56)$$

By examination the value of k_{mn} beyond which to use Equations (53), (54), (55) and (56) was chosen to be 8.5.

Calculation of Velocity Perturbations

By substituting the appropriate coefficients in the series listed in Appendix B, the velocity perturbations at any point can be computed. The real part of the combination of coefficient and $e^{im\phi}$ in each series is the part that has physical significance.

The velocity perturbations were calculated for a series of conditions to determine the effects of numbers of blades and spacing distance. For the shortest spacing distance ($\frac{2d}{R_p} = 0.267$) calculations were made for 2, 5 and 10-bladed propellers. For the 10-bladed propeller calculations, spacing distances corresponding to $\frac{2d}{R_p} = 0.267$, 0.667, and 1.067 were performed. This gave a total of five distinct sets of conditions.

The computations of the perturbations in Region (1) and just downstream of Disc A in Region (2) would be the same regardless of what set of conditions was being considered if it is assumed that the inputs are unchanged. Calculation of the perturbations at these locations was therefore performed only once. The results of these calculations are shown in Figs. 40 through 44.

Comparison of the calculated tangential components just upstream and just downstream of the control surfaces with the measured values were already made and assumed to be adequate. The v_r and v_z calculations at the same locations show how well these components can be represented on the basis of coefficients derived from just the v_u distributions. The v_{r_1} and v_{z_1} computed distributions just in front of Disc A are also seen to compare reasonably well with the measured values. Just downstream of Disc A, however, the calculated v_{r_2} values are found to be considerably at variance with those measured in the region of the tip radius. The measured v_{z_2} values in the same plane do check fairly well with the predicted except at points very close to the trailing vortex from the control surface tip.

The calculated effect of the propeller on the distortions are shown in Figs. 45 through 49 for the case of $d = 1.0$ inch and $B = 10$. The predicted violent radial perturbations are still present just upstream of the propeller but are radically reduced downstream of the propeller. In all cases calculated continuity at both discs was maintained. For this reason v_{z_2} and v_{z_3} are always plotted as being the same. Angular locations

other than in the first quadrant are shown for this set of conditions to demonstrate the manner in which the disturbances have ceased to follow strictly cosine or sine type distributions.

Distributions at the propeller for all the remaining sets of conditions are shown in Figs. 50 through 65. The important observation to be made is the apparent disordered distributions that are present with spacings larger than $d = 1.0$ inches.

Prediction of the velocity perturbations nine inches upstream of the control surfaces and nine inches downstream of the propeller were made. In both cases the results were indistinguishable from zero and were therefore not reported.

Calculation of Propeller Forces

With a knowledge of the velocity components before and after the propeller, the torque force at each radial location of the propeller can be determined. By taking the component of this force in the side and vertical directions an estimate of side and pitching force can be made.

From standard propeller theory a torque force coefficient defined as:

$$C_{Q_f} = \frac{Q_f}{\frac{1}{2} \rho \bar{V}_x^2 \pi R_p^2} \quad (57)$$

can be expressed in terms of the velocity perturbations at
Disc B:

$$C_{Q_f} = \int_{x_h}^{1.0} 4x \left(\frac{\sqrt{u_2}}{\sqrt{z}} - \frac{\sqrt{u_3}}{\sqrt{z}} \right) \left(1 + \frac{\sqrt{z_2}}{\sqrt{z}} \right) dx \quad (58)$$

One can perform this integration at various angular
locations and then find the mean component of force in
both the side and vertical directions by use of:

$$C_H = \frac{1}{2\pi} \int_0^{2\pi} C_{Q_f} \cos \varphi \, d\varphi \quad (59)$$

and

$$C_V = \frac{1}{2\pi} \int_0^{2\pi} C_{Q_f} \sin \varphi \, d\varphi \quad (60)$$

The results of this type of calculation are shown in
Table II. The coefficients are the same as those used for
the experimental measurements.

TABLE II
Calculated Force Coefficients

$\frac{2d}{R_p}$	B	C_H	C_V
0.267	10	- .0362	+ .0264
0.267	5	- .0122	- .0031
0.267	2	0.0	0.0
0.667	10	+ .0082	0.0
1.067	10	+ .0085	- .0143

The C_H value for the $d = 1.0$, $B = 10$ case is high compared to experiment. For the 5-bladed propeller C_H is close to measured and for the 2-bladed propeller it is low. The increase of C_H with numbers of blades is therefore greater than shown by experiment. The variation with numbers of blades of predicted and experimental C_H and C_V values are compared in Fig. 66.

The magnitude of C_V for the first listed case also appears to be very high. The C_H and C_V values for the larger spacings and the plots from which they were derived generally appear unreliable.

CHAPTER VI

DISCUSSION OF RESULTS AND CONCLUSIONS

Experimental Results

The experimental phase of the investigation had the dual goal of measuring the disturbed flow and of measuring the force reaction to the disturbed flow. These goals were accomplished. The first phase of the distortion measurements was primarily to determine the disturbance to be used as the input to the theoretical solution. The second phase was directed toward measuring the flow perturbations after having passed through the propeller.

The distribution of the v_{u_3} perturbation measured immediately downstream of the propeller (Fig. 36) shows that the general shape of the original disturbance is maintained. The magnitude is less and as such is a measure of the force reaction of the propeller. The perturbation still was present nine inches farther downstream although again further diminished (Fig. 37).

The force measurements gave a quantitative picture of how the effectiveness of the control surfaces is reduced. As one would suppose, the maximum reaction occurs with the 10-bladed propeller. The cancellation was about 34 per cent for this case. From the shape of

this curve in Fig. 35, the variation with numbers of blades has leveled at about 10 blades, indicating that it represents close to the maximum reaction.

The force measurements show further that the reaction is linear over a range of angles to 6 degrees. At some higher angle this linearity must cease to exist, but in the linear range the percentage of force cancellation is the same. The comparatively constant reaction with changes in advance ratio show that the theoretical result that the reaction of a thrusting or nonthrusting propeller is the same is reasonably accurate. The force measurements showed practically no variation with the spacings investigated.

Theoretical Results

A measure of the theoretical development can first be made in how well the original disturbed flow can be represented. The v_u disturbances before and after the control surfaces were represented reasonably well by their respective series. The calculated v_{r_2} downstream of the control surface, however, varied considerably from the measured values. A possible explanation for this lies in the difference between a real flow vortex with viscous effects and a potential vortex represented only approximately by a truncated series. Mathematically

the source of trouble is traceable to the slopes of the Bessel functions. Because of the abrupt change in v_{u_2} at the tip region of the control surfaces the cumulative effect of the Bessel function slopes is very strong.

The effect of the propeller on the flow just upstream of the propeller is an interesting one. As seen in Figs. 45, 50, and 55, the vortex near the tip region apparently reverses. The tangential perturbation is generally reduced as it approaches the propeller. The greatest reduction, however, occurs with a smaller number of blades.

In Fig. 48, the tangential perturbation is seen to be generally negative after passing through the propeller. When the distortion feeding into the propeller is generally positive, it does not seem likely that the tangential flow leaving would be negative. This is an indication that the propeller action is not properly represented either through the original factors $M(r)$ and $N(r)$ or through an insufficient number of terms in the series representing these factors. The convergence of these series was not very complete after 20 terms.

The breakdown of the perturbation predictions for larger spacings probably has its origin in the accuracy problem described in Chapter V and Appendix E. Although the accuracy was improved greatly by simplifying the

coefficient equations beyond a certain value of $k_{mn}d$, the choice of what $k_{mn}d$ to use as the dividing point may be fairly critical. The effect of the accuracy problem on the predictions of the force reactions follows logically. The force coefficients predicted for the larger spacings do not appear to make much sense.

The prediction for the $\frac{2d}{R_p} = 0.267$ spacing, 10-bladed case is apparently high and is probably traceable to the arguments already brought forth with respect to $M(r)$ and $N(r)$. Although the predicted 5-bladed case is close to the measured value, the 2-bladed prediction is too low. The theoretical trend of the variation of force coefficient with blade number therefore has a greater slope than the experimental one.

There is a rapid decay of the predicted perturbations with distance away from the discs, as shown by the fact that no measurable values were computed at distances nine inches away. This is contrary to the experimental findings which show that the perturbations do exist at distances such as that.

Conclusions

In the light of the discussion of results the following conclusions can be made:

1. The experimental results give a very good picture of the force cancellation by a propeller.

2. The theoretical method that was developed appears to be a useable one.
3. The theory is being extended to its limits when being applied to a case with a strong vortex present.
4. The theoretical approach can probably be extended easily to the case of a ducted rotating device.
5. The agreement of theory with experiment is sufficiently good to warrant further studies concerned chiefly with improving the accuracy of predictions.

Suggestions for Further Research

The following suggestions are made with regard to future work in this general area.

1. Work with existing test setup should be extended to the cases of propellers with different diameters than the control surfaces. This very practical type study can be done simply by cutting down the tips of the existing blades.
2. Ways to improve the computing accuracy of a study such as this should be undertaken.

3. An extension of the theory to the case of control surfaces and propellers immersed in the boundary layer of a body should be pursued.
4. An extension of this theoretical approach to pumps and compressors should be tried.

REFERENCES

1. Sears, William R. Some Aspects of Non-Stationary Airfoil Theory and Its Practical Application. Journal of the Aeronautical Sciences, Vol. 8, pp. 104-108, August 1941.
2. Kemp, N. H. and Sears, W. R. The Unsteady Forces Due to Viscous Wakes in Turbomachines. Journal of the Aeronautical Sciences, Vol. 22, pp. 478-483, July 1955.
3. Meyer, R. X. The Effect of Wakes on the Transient Pressure and Velocity Distributions in Turbomachines. Transactions of the American Society of Mechanical Engineers, Vol. 80, pp. 1544-1552, 1958.
4. Yeh, Hsuan and Eisenhuth, J. J. The Unsteady Wake Interaction in Turbomachinery and Its Effect on Cavitation. Journal of Basic Engineering, Vol. 81, pp. 181-189, June 1959.
5. Smith, Leroy H. Recovery Ratio - A Measure of the Loss Recovery Potential of Compressor Stages. Transactions of the American Society of Mechanical Engineers, Vol. 80, pp. 517-524, April 1958.
6. Ehrich, Fredric. Circumferential Inlet Distortion in Axial Flow Turbomachinery. Journal of the Aeronautical Sciences, Vol. 24, pp. 413-417, June 1957.
7. Yeh, Hsuan, An Actuator Disc Analysis of Inlet Distortion and Rotating Stall in Axial Flow Turbomachines. Journal of the Aero/Space Sciences, Vol. 26, pp. 739-753, November 1959.
8. McCune, James E. A Three-Dimensional Theory of Axial Compressor Blade Rows - Application in Subsonic and Supersonic Flows. Journal of the Aero/Space Sciences, Vol. 25, pp. 544-560, September 1958.
9. McCune, James E. The Transient Flow Field of an Axial Compressor Blade Row. Journal of the Aero/Space Sciences, Vol. 25, pp. 616-626, October 1958.

10. Smith, L. H., Jr., Trangott, S. C., and Wislicenus, G. F. A Practical Solution of a Three-Dimensional Flow Problem of Axial-Flow Turbomachinery. Transactions of the American Society of Mechanical Engineers, Vol. 75, pp. 789-803, July 1953.
11. McCormick, B. W., Eisenhuth, J. J., and Lynn, J. E. A Study of Torpedo Propellers - Part I, Ordnance Research Laboratory Report NOrd 16597-5, March 30, 1956.
12. Lehman, A. F. The Garfield Thomas Water Tunnel. Ordnance Research Laboratory Report NOrd 16597-56, September 1959.
13. Mercier, J. A. Optimum Propellers with Finite Hubs. Hydronautics, Inc., Technical Report 127-1, June 1962.
14. Abbott, Ira, H., Von Doenhoff, Albert E., and Stivers, Louis S., Jr. Summary of Airfoil Data. National Advisory Committee for Aeronautics Report No. 824, 1945.
15. British Association for the Advancement of Science. Mathematical Tables - Volume VI, Bessel Functions - Part I - Functions of Orders Zero and Unity. University Press, Cambridge, 1958.
16. British Association for the Advancement of Science. Mathematical Tables - Volume X, Bessel Functions - Part II - Functions of Positive Integer Order. University Press, Cambridge, 1960.
17. Watson, G. N., A Treatise on the Theory of Bessel Functions. The Macmillan Company, 1945.
18. Jahnke, Eugene, Dr., Emde, Fritz. Tables of Functions with Formulae and Curves. Dover Publications, 1945.
19. Churchill, Ruel V. Fourier Series and Boundary Value Problems. McGraw-Hill, 1941.

20. Laposata, S. M. and Eisenhuth, J. J. Computer Program for Flow Distortion Investigation. Ordnance Research Laboratory Technical Memorandum 5.2410-19, May 24, 1963.

APPENDIX A

DERIVATION OF PRESSURE EQUATION

The equations of motion in cylindrical coordinates are:

$$\begin{aligned} V_r \frac{\partial V_r}{\partial r} + \frac{V_u}{r} \frac{\partial V_r}{\partial \phi} + V_z \frac{\partial V_r}{\partial z} - \frac{V_u^2}{r} &= -\frac{1}{\rho} \frac{\partial P}{\partial r} \\ V_r \frac{\partial V_u}{\partial r} + \frac{V_u}{r} \frac{\partial V_u}{\partial \phi} + V_z \frac{\partial V_u}{\partial z} + \frac{V_r V_u}{r} &= -\frac{1}{\rho} \frac{1}{r} \frac{\partial P}{\partial \phi} \quad (\text{A-1}) \\ V_r \frac{\partial V_z}{\partial r} + \frac{V_u}{r} \frac{\partial V_z}{\partial \phi} + V_z \frac{\partial V_z}{\partial z} &= -\frac{1}{\rho} \frac{\partial P}{\partial z} \end{aligned}$$

Likewise in cylindrical coordinates, the continuity equation can be written as

$$\frac{1}{r} \frac{\partial}{\partial r} (r V_r) + \frac{1}{r} \frac{\partial V_u}{\partial \phi} + \frac{\partial V_z}{\partial z} = 0 \quad (\text{A-2})$$

The following are assumed

$$\begin{aligned} V_r &= \bar{v}_r(r, \phi, z) \\ V_u &= \bar{v}_u(r, \phi, z) \\ V_z &= \bar{V}_z(r) + \bar{v}_z(r, \phi, z) \\ P &= \bar{p}(r, \phi, z) \end{aligned} \quad (\text{A-3})$$

where the disturbance velocities, v_r , v_u , and v_z and the disturbance pressure p are very small compared to the primary velocity $\bar{V}_z = \bar{V}_z(r)$. When used in Equations (A-1) the following set of linear differential equations result:

$$\bar{V}_z \frac{\partial \bar{v}_r}{\partial z} = -\frac{1}{\rho} \frac{\partial p}{\partial r} \quad (\text{A-4})$$

$$\bar{V}_z \frac{\partial \bar{v}_u}{\partial z} = -\frac{1}{\rho} \frac{1}{r} \frac{\partial p}{\partial \phi} \quad (\text{A-5})$$

$$\bar{v}_r \left(\frac{d\bar{V}_z}{dr} \right) + \bar{V}_z \frac{\partial \bar{v}_z}{\partial z} = -\frac{1}{\rho} \frac{\partial p}{\partial z} \quad (\text{A-6})$$

The continuity equation also becomes:

$$\frac{1}{r} \frac{\partial}{\partial r} (r \bar{v}_r) + \frac{1}{r} \frac{\partial \bar{v}_u}{\partial \phi} + \frac{\partial \bar{v}_z}{\partial z} = 0 \quad (\text{A-7})$$

Solving for $\frac{\partial \bar{v}_z}{\partial z}$ in Equation (A-7) and substituting in Equation (A-6):

$$\bar{v}_r \left(\frac{d\bar{V}_z}{dr} \right) - \frac{\bar{V}_z}{r} \frac{\partial}{\partial r} (r \bar{v}_r) - \frac{\bar{V}_z}{r} \frac{\partial \bar{v}_u}{\partial \phi} = -\frac{1}{\rho} \frac{\partial p}{\partial z} \quad (\text{A-8})$$

Differentiating Equation (A-8) with respect to z yields:

$$\frac{\partial v_r}{\partial z} \frac{d\bar{V}_z}{dr} - \frac{\bar{V}_z}{r} \left[\frac{\partial v_r}{\partial z} + r \frac{\partial^2 v_r}{\partial r \partial z} + \frac{\partial^2 v_\theta}{\partial \phi \partial z} \right] = -\frac{1}{r} \frac{\partial^2 p}{\partial z^2} \quad (\text{A-9})$$

Differentiating Equation (A-4) with respect to r and Equation (A-5) with respect to ϕ and substituting the results and Equation (A-4) in Equation (A-9) produces, after proper grouping of terms:

$$\bar{V}_z^2 \frac{\partial}{\partial z} \left(\frac{1}{\bar{V}_z^2} \frac{\partial p}{\partial r} \right) + \frac{1}{r} \frac{\partial p}{\partial r} + \frac{1}{r^2} \frac{\partial^2 p}{\partial \phi^2} + \frac{\partial^2 p}{\partial z^2} = 0 \quad (\text{A-10})$$

APPENDIX B

DERIVATION OF VELOCITY PERTURBATION EQUATIONS

The equations for pressure perturbation can be written, as in Equation (2), for each of the three regions:

$$\begin{aligned}
 p_1 &= \sum_m \sum_n a_{mn} Z_m(k_{mn}r) e^{k_{mn}z} e^{im\varphi} \\
 p_2 &= \sum_m \sum_n b_{mn} Z_m(k_{mn}r) e^{k_{mn}z} e^{im\varphi} + \sum_m \sum_n c_{mn} Z_m(k_{mn}r) e^{-k_{mn}z} e^{im\varphi} \quad (\text{B-1}) \\
 p_3 &= \sum_m \sum_n d_{mn} Z_m(k_{mn}r) e^{-k_{mn}z} e^{im\varphi}
 \end{aligned}$$

These expressions for p can be substituted in the linearized equations of motion and, upon integration, equations for the velocity perturbations in each region can be derived:

Region (1)

$$\begin{aligned}
 \frac{\tilde{v}_r}{V_2} &= - \sum_m \sum_n A_{mn} Z'_m(k_{mn}r) e^{k_{mn}z} e^{im\varphi} + f_1(r, \varphi) \\
 \frac{\tilde{v}_{u_1}}{V_2} &= - \sum_m \sum_n \frac{im}{k_{mn}r} A_{mn} Z_m(k_{mn}r) e^{k_{mn}z} e^{im\varphi} + g_1(r, \varphi) \quad (\text{B-2}) \\
 \frac{\tilde{v}_{z_1}}{V_2} &= - \sum_m \sum_n A_{mn} Z_m(k_{mn}r) e^{k_{mn}z} e^{im\varphi} + h_1(r, \varphi)
 \end{aligned}$$

Region (2)

$$\frac{\sqrt{r_2}}{\sqrt{z}} = -\sum_m \sum_n B_{mn} Z'_m(k_{mn}r) e^{k_{mn}z} e^{im\varphi} + \sum_m \sum_n C_{mn} Z'_m(k_{mn}r) e^{-k_{mn}z} e^{im\varphi} + f_2(r, \varphi)$$

$$\frac{\sqrt{u_2}}{\sqrt{z}} = -\sum_m \sum_n \frac{im}{k_{mn}r} B_{mn} Z_m(k_{mn}r) e^{k_{mn}z} e^{im\varphi} + \sum_m \sum_n \frac{im}{k_{mn}r} C_{mn} Z_m(k_{mn}r) e^{-k_{mn}z} e^{im\varphi} + g_2(r, \varphi) \quad (B-3)$$

$$\frac{\sqrt{z_2}}{\sqrt{z}} = -\sum_m \sum_n B_{mn} Z_m(k_{mn}r) e^{k_{mn}z} e^{im\varphi} - \sum_m \sum_n C_{mn} Z_m(k_{mn}r) e^{-k_{mn}z} e^{im\varphi} + h_2(r, \varphi)$$

Region (3)

$$\frac{\sqrt{r_3}}{\sqrt{z}} = \sum_m \sum_n D_{mn} Z'_m(k_{mn}r) e^{-k_{mn}z} e^{im\varphi} + f_3(r, \varphi)$$

$$\frac{\sqrt{u_3}}{\sqrt{z}} = \sum_m \sum_n \frac{im}{k_{mn}r} D_{mn} Z_m(k_{mn}r) e^{-k_{mn}z} e^{im\varphi} + g_3(r, \varphi) \quad (B-4)$$

$$\frac{\sqrt{z_3}}{\sqrt{z}} = -\sum_m \sum_n D_{mn} Z_m(k_{mn}r) e^{-k_{mn}z} e^{im\varphi} + h_3(r, \varphi)$$

The definition for $z'_m(K_{mn}r)$, where it occurs, is:

$$Z'_m(K_{mn}r) = \frac{dZ_m(K_{mn}r)}{d(K_{mn}r)} \quad (\text{B-5})$$

The functions, $f(r, \varphi)$, $g(r, \varphi)$, and $h(r, \varphi)$ are a result of the integrations. The evaluation of these functions is dependent upon the physical problem and is discussed in another section.

The coefficient, A_{mn} , used in these equations is defined as:

$$A_{mn} = \frac{a_{mn}}{\rho \bar{V}_z^2} \quad (\text{B-6})$$

The coefficients, B_{mn} , C_{mn} , and D_{mn} , are defined in the same manner with respect to b_{mn} , c_{mn} , and d_{mn} respectively.

APPENDIX C

DERIVATION OF RELATION BETWEEN TANGENTIAL AND AXIAL VELOCITY PERTURBATIONS AT DISC B

Referring to Fig. 3, a relation similar to Equation (23) can be written:

$$\frac{w_T'}{\bar{V}_2} = \frac{1}{4K} \cdot \frac{CB}{2\pi r} \cdot \frac{V_e'}{\bar{V}_2} C_l' \quad (C-1)$$

where the primes indicate conditions with a distortion present. Let it be assumed that the chord of the section is set at the angle θ . C_l' is then given by:

$$C_l' = C_{l_0} + a_0 (\theta - \psi) \quad (C-2)$$

where C_{l_0} is again the lift coefficient at zero angle of attack and a_0 is the slope of the section lift curve.

The angle θ is given by:

$$\theta = \tan^{-1} \left[\frac{1 + h_3(r)}{\frac{\pi x}{J} - \frac{1}{2} g_3(r)} \right] \quad (C-3)$$

and the angle ψ is given by:

$$\psi = \tan^{-1} \left[\frac{1 + \frac{\bar{v}_{z_2}}{\bar{V}_2}}{\frac{\pi x}{J} + \frac{\bar{v}_{u_2}}{\bar{V}_2} - \frac{w_T'}{\bar{V}_2}} \right] \quad (C-4)$$

To be consistent with the linearized aspects of the problem these expressions for angle must also be linearized. Consider first the angle, θ . This can be represented by:

$$\theta = \tan^{-1} y \quad (C-5)$$

A reasonable range of $\frac{\pi x}{J}$ would be from 0.3 to 3.0. Therefore, y would have a corresponding range of approximately $3.0 \rightarrow 0.3$. Because it could be reasonably expected that values of y would be both greater than and less than 1.0 it would be necessary to consider two series for θ . For $y^2 < 1$:

$$\tan^{-1} y = y - \frac{1}{3} y^3 + \frac{1}{5} y^5 - \dots \quad (C-6)$$

For $y^2 > 1$

$$\tan^{-1} y = \frac{\pi}{2} - \frac{1}{y} + \frac{1}{3y^3} - \frac{1}{5y^5} + \dots \quad (C-7)$$

The results of linearizing either of these expressions is the same so only details of working with Equation (C-6) will be discussed.

Let the following substitutions be made for ease of handling:

$$\begin{aligned} A &= \frac{\pi x}{J} \\ a &= h_3(r) \\ b &= -\frac{1}{2} g_3(r) \end{aligned} \tag{C-8}$$

Therefore:

$$\begin{aligned} y &= \frac{1+a}{A+b} = \frac{1}{A} \left(\frac{1+a}{1+\frac{b}{A}} \right) \sim \frac{1}{A} \left(1+a - \frac{b}{A} \right) \\ y^3 &\sim \frac{1}{A^3} \left(1 + 3a - \frac{3b}{A} \right) \\ y^5 &\sim \frac{1}{A^5} \left(1 + 5a - \frac{5b}{A} \right) \end{aligned} \tag{C-9}$$

Substituting these approximations back into Equation (C-6):

$$\begin{aligned} \tan^{-1} y &= \left(\frac{1}{A} - \frac{1}{3A^3} + \frac{1}{5A^5} - \dots \right) + a \left(\frac{1}{A} - \frac{1}{A^3} + \frac{1}{A^5} - \dots \right) \\ &\quad - \frac{b}{A} \left(\frac{1}{A} - \frac{1}{A^3} + \frac{1}{A^5} - \dots \right) \end{aligned} \tag{C-10}$$

or

$$\tan^{-1} y = \tan^{-1} \left(\frac{1}{A} \right) + \left(a - \frac{b}{A} \right) \left[\frac{1}{A} - \frac{1}{A^3} + \frac{1}{A^5} - \dots \right] \tag{C-11}$$

Taking now the series $\left[\frac{1}{A} - \frac{1}{A^3} + \frac{1}{A^5} - \dots\right]$ let $\frac{1}{A} = \gamma$.
The series can then be put in the following succeeding forms:

$$I = \gamma - \gamma^3 + \gamma^5 - \dots$$

$$\frac{I}{\gamma} - 1 = -\gamma^2 + \gamma^4 - \dots$$

$$\frac{I - \gamma}{\gamma} = -\gamma \left[\gamma - \gamma^3 + \gamma^5 - \dots \right] \quad (\text{C-12})$$

$$I - \gamma = -\gamma^2 I$$

$$I = \frac{\gamma}{1 + \gamma^2} = \frac{A}{1 + A^2}$$

Finally:

$$\theta = \tan^{-1}\left(\frac{1}{\pi x}\right) + \left[h_3(r) + \frac{1}{(\pi x)} \cdot \frac{1}{2} g_3(r) \right] \cdot \frac{\frac{\pi x}{j}}{1 + \left(\frac{\pi x}{j}\right)^2} \quad (\text{C-13})$$

Using the same type of derivation the expression for ψ will be:

$$\psi = \tan^{-1}\left(\frac{1}{\pi x}\right) + \left[\frac{\sqrt{z_2}}{\sqrt{z_2}} - \frac{1}{(\pi x)} \cdot \frac{(\sqrt{u_2} - u_2')}{\sqrt{z_2}} \right] \cdot \frac{\frac{\pi x}{j}}{1 + \left(\frac{\pi x}{j}\right)^2} \quad (\text{C-14})$$

and from these:

$$(\theta - \psi) = \frac{(\frac{\pi x}{J})}{1 + (\frac{\pi x}{J})^2} \times$$

$$\left[\left(h_3(r) - \frac{\sqrt{z_2}}{\sqrt{z}} \right) + \frac{(\frac{1}{2} g_3(r) + \frac{\sqrt{u_2}}{\sqrt{z}} - \frac{\omega_{\tau}'}{\sqrt{z}})}{\frac{\pi x}{J}} \right] \quad (C-15)$$

From the velocity diagram in Fig. 3 the following expression for V_e' is derived:

$$\frac{V_e'}{\sqrt{z}} = \left[\left(1 + \frac{\sqrt{z_2}}{\sqrt{z}} \right)^2 + \left(\frac{\pi x}{J} + \frac{\sqrt{u_2}}{\sqrt{z}} - \frac{\omega_{\tau}'}{\sqrt{z}} \right)^2 \right]^{\frac{1}{2}} \quad (C-16)$$

To linearize Equation (C-16) let:

$$\frac{\sqrt{z_2}}{\sqrt{z}} = a$$

$$\frac{\pi x}{J} = A \quad (C-17)$$

$$\left(\frac{\sqrt{u_2}}{\sqrt{z}} - \frac{\omega_{\tau}'}{\sqrt{z}} \right) = b$$

so that

$$\frac{V_e'}{\sqrt{z}} = \left[(1 + a)^2 + A^2 \left(1 + \frac{b}{A} \right)^2 \right]^{\frac{1}{2}} \quad (C-18)$$

Dropping higher order terms within the brackets:

$$\frac{V_e'}{V_z} = \left[1 + 2a + A^2 \left(1 + 2 \frac{b}{A} \right) \right]^{\frac{1}{2}} \quad (C-19)$$

which can be rewritten:

$$\frac{V_e'}{V_z} = \left[(1 + A^2) + 2(a + bA) \right]^{\frac{1}{2}} \quad (C-20)$$

Using the binomial expansion and dropping higher order terms:

$$\frac{V_e'}{V_z} \sim (1 + A^2)^{\frac{1}{2}} + \frac{1}{2} (1 + A^2)^{-\frac{1}{2}} [2(a + bA)] \quad (C-21)$$

When Equations (C-17) are substituted and terms rearranged the final linearized equation for V_e' is:

$$\frac{V_e'}{V_z} = \left[1 + \left(\frac{\pi x}{J} \right)^2 \right]^{\frac{1}{2}} x$$

$$\left\{ 1 + \frac{1}{\left[1 + \left(\frac{\pi x}{J} \right)^2 \right]} \left[\frac{v_{z2}}{V_z} + \left(\frac{\pi x}{J} \right) \left(\frac{v_{u2}}{V_z} - \frac{w_z'}{V_z} \right) \right] \right\} \quad (C-22)$$

If substitutions are now made in Equation (C-2) and then in Equation (C-1), the following equation results after further dropping of higher order terms:

$$\frac{\omega'_t}{\bar{V}_2} = \left(\frac{1}{4K} \cdot \frac{CB}{2\pi r} \right) \left[1 + \left(\frac{\pi Z}{J} \right)^2 \right]^{\frac{1}{2}} \left\{ C_{L_0} + a_0 \left[\frac{\left(\frac{\pi Z}{J} \right)}{1 + \left(\frac{\pi Z}{J} \right)^2} \right] \times \right. \\ \left. \left[\left(h_3(r) - \frac{\bar{v}_{z_2}}{\bar{V}_2} \right) + \frac{\left(\frac{1}{2} g_3(r) + \frac{\bar{v}_{u_2}}{\bar{V}_2} - \frac{\omega'_t}{\bar{V}_2} \right)}{\left(\frac{\pi Z}{J} \right)} \right] \right\} \quad (C-23)$$

The change in the tangential component of velocity across Disc B is represented by $2K \omega'_t$. One can therefore write:

$$\frac{\bar{v}_{u_3}}{\bar{V}_2} = \frac{\bar{v}_{u_2}}{\bar{V}_2} - 2K \frac{\omega'_t}{\bar{V}_2} \quad (C-24)$$

When Equation (C-23) is substituted in Equation (C-24)

\bar{v}_{u_3} is given in the following form:

$$\frac{\bar{v}_{u_3}}{\bar{V}_2} = K(r) + M(r) \frac{\bar{v}_{z_2}}{\bar{V}_2} + N(r) \frac{\bar{v}_{u_2}}{\bar{V}_2} \quad (C-25)$$

where:

$$K(r) = - \frac{2 \left(\frac{1}{4} \cdot \frac{CB}{2\pi r} \right) \left[1 + \left(\frac{\pi x}{J} \right)^2 \right]^{\frac{1}{2}}}{1 + \frac{a_0 \left(\frac{1}{4K} \cdot \frac{CB}{2\pi r} \right)}{\left[1 + \left(\frac{\pi x}{J} \right)^2 \right]^{\frac{1}{2}}}} \cdot \left\{ c_{\ell_0} + a_0 \left[\frac{\left(\frac{\pi x}{J} \right)}{1 + \left(\frac{\pi x}{J} \right)^2} \right] \left[h_3(r) + \frac{\frac{1}{2} S_3(r)}{\left(\frac{\pi x}{J} \right)} \right] \right\} \quad (C-26)$$

$$M(r) = \frac{2 \left(\frac{1}{4} \cdot \frac{CB}{2\pi r} \right) \left[1 + \left(\frac{\pi x}{J} \right)^2 \right]^{\frac{1}{2}}}{1 + \frac{a_0 \left(\frac{1}{4K} \cdot \frac{CB}{2\pi r} \right)}{\left[1 + \left(\frac{\pi x}{J} \right)^2 \right]^{\frac{1}{2}}}} \cdot \left\{ a_0 \left[\frac{\left(\frac{\pi x}{J} \right)}{1 + \left(\frac{\pi x}{J} \right)^2} \right] \right\} \quad (C-27)$$

$$N(r) = 1 - \frac{2 a_0 \left(\frac{1}{4} \cdot \frac{CB}{2\pi r} \right) \left[1 + \left(\frac{\pi x}{J} \right)^2 \right]^{\frac{1}{2}}}{1 + \frac{a_0 \left(\frac{1}{4K} \cdot \frac{CB}{2\pi r} \right)}{\left[1 + \left(\frac{\pi x}{J} \right)^2 \right]^{\frac{1}{2}}}} \cdot \left[\frac{1}{1 + \left(\frac{\pi x}{J} \right)^2} \right] \quad (C-28)$$

It will be observed that when the propeller is a nonthrusting propeller the value of $K(r)$ is zero. $M(r)$ and $N(r)$ will have values regardless of the propeller design. If one goes through the detailed substitutions,

it will be observed that when no distortion is present,
Equation (C-25) reduces to:

$$\frac{\sqrt{u_3}}{\bar{V}_2} = -2 K \frac{\omega_T}{\bar{V}_2} \quad (\text{C-29})$$

This is a check on the correctness of the relation.

APPENDIX D

SOLUTION OF UNKNOWN COEFFICIENT, C_{mn}

As stated previously the propeller need be considered only as a non-thrusting propeller. Equation (44) can then be written as:

$$\frac{\bar{u}_3}{\bar{V}_z} = M(r) \frac{\bar{u}_2}{\bar{V}_z} + N(r) \frac{\bar{u}_2}{\bar{V}_z} \quad (D-1)$$

with the $g_3(r)$ and that part of $h_2(r, \varphi)$ equivalent to $h_3(r)$ dropped from the expressions for v_{u_3} and v_{z_2} .

Substituting from Equations (B-3) and (B-4) into Equation (D-1):

$$\begin{aligned} & \sum_m \sum_n \frac{i m D_{mn}}{k_{mn} r} Z_m(k_{mn} r) e^{-k_{mn} d} e^{i m \varphi} \\ &= -M(r) \left[\sum_m \sum_n B_{mn} Z_m(k_{mn} r) e^{k_{mn} d} e^{i m \varphi} \right. \\ & \quad \left. + \sum_m \sum_n C_{mn} Z_m(k_{mn} r) e^{-k_{mn} d} e^{i m \varphi} - \sum_m \sum_n O_{mn} Z_m(k_{mn} r) e^{i m \varphi} \right] \\ & \quad - N(r) \left[\sum_m \sum_n \frac{i m}{k_{mn} r} B_{mn} e^{k_{mn} d} e^{i m \varphi} \right. \\ & \quad \left. - \sum_m \sum_n \frac{i m}{k_{mn} r} C_{mn} Z_m(k_{mn} r) e^{-k_{mn} d} e^{i m \varphi} \right] \quad (D-2) \end{aligned}$$

For a single wave in r and φ the following would then be true:

$$\begin{aligned} \frac{i m}{k_{mn} r} D_{mn} e^{-k_{mn} d} = & -M(r) e^{k_{mn} d} B_{mn} - M(r) e^{-k_{mn} d} C_{mn} \\ & + M(r) O_{mn} - N(r) \frac{i m}{k_{mn} r} e^{k_{mn} d} B_{mn} \\ & + N(r) \frac{i m}{k_{mn} r} e^{-k_{mn} d} C_{mn} \end{aligned} \quad (D-3)$$

It is probably most convenient to substitute into this equation so that it is put in terms of one unknown, C_{mn} . Equation (21) can be used for B_{mn} , Equation (31) for D_{mn} , and Equation (34) for O_{mn} . When these substitutions are made, the following equation results:

$$\begin{aligned} \frac{i m}{k_{mn} r} e^{-k_{mn} d} (1 - 2 e^{2k_{mn} d} + e^{4k_{mn} d}) C_{mn} + \frac{i m}{k_{mn} r} \left(\frac{i}{m} \right) (e^{2k_{mn} d} - 1) P_{mn} \\ + \frac{i m}{k_{mn} r} e^{-k_{mn} d} A_{mn} = & -M(r) e^{k_{mn} d} (e^{2k_{mn} d} C_{mn}) \\ & - M(r) e^{k_{mn} d} \left(\frac{i}{m} e^{k_{mn} d} P_{mn} \right) - M(r) e^{-k_{mn} d} C_{mn} \\ & + 2 M(r) e^{k_{mn} d} C_{mn} + \frac{i}{m} M(r) P_{mn} - M(r) e^{-k_{mn} d} A_{mn} \\ & - N(r) \frac{i m}{k_{mn} r} e^{3k_{mn} d} C_{mn} - N(r) \frac{i m}{k_{mn} r} \left(\frac{i}{m} \right) e^{2k_{mn} d} P_{mn} \\ & + N(r) \frac{i m}{k_{mn} r} e^{-k_{mn} d} C_{mn} \end{aligned} \quad (D-4)$$

By combining terms and defining the following:

$$\begin{aligned} S &= (1 - 2 e^{2k_{mn}d} + e^{4k_{mn}d}) e^{-k_{mn}d} \\ T &= (e^{4k_{mn}d} - 1) e^{-k_{mn}d} \\ U &= (e^{2k_{mn}d} - 1) \end{aligned} \quad (D-5)$$

Equation (D-4) can be altered to read:

$$\begin{aligned} &\left\{ [M(r) \cdot S] + i \left[\frac{1}{r} S + \frac{N(r)}{r} T \right] \frac{m}{k_{mn}} \right\} C_{mn} \\ &= \left[\left(\frac{1}{r} \frac{U}{k_{mn}} + \frac{N(r)}{r} \cdot \frac{e^{2k_{mn}d}}{k_{mn}} \right) P_{mn} - M(r) e^{-k_{mn}d} A_{mn} \right] \\ &\quad - i \left[M(r) \frac{U}{m} P_{mn} + \frac{1}{r} \cdot \frac{m}{k_{mn}} e^{-k_{mn}d} A_{mn} \right] \end{aligned} \quad (D-6)$$

Functions of r must be eliminated in Equation (D-6) so that C_{mn} will be independent of r . To do this the following are assumed:

$$\begin{aligned} M(r) &= \sum_l \alpha_{l2} Z_l(k_{l2} r) \\ \frac{N(r)}{r} &= \sum_l \gamma_{l2} Z_l(k_{l2} r) \\ \frac{1}{r} &= \sum_l \lambda_{l2} Z_l(k_{l2} r) \end{aligned} \quad (D-7)$$

in which case:

$$\begin{aligned}\alpha_{le} &= \frac{1}{\frac{r_0^2}{2} [Z_2(k_{le}r_0)]^2 + \frac{1-k_{le}^2r_h^2}{2k_{le}^2} [Z_1(k_{le}r_h)]^2} \int_{r_h}^{r_0} r M(r) Z_1(k_{le}r) dr \\ \gamma_{le} &= \frac{1}{\frac{r_0^2}{2} [Z_2(k_{le}r_0)]^2 + \frac{1-k_{le}^2r_h^2}{2k_{le}^2} [Z_1(k_{le}r_h)]^2} \int_{r_h}^{r_0} N(r) Z_1(k_{le}r) dr \\ \lambda_{le} &= \frac{1}{\frac{r_0^2}{2} [Z_2(k_{le}r_0)]^2 + \frac{1-k_{le}^2r_h^2}{2k_{le}^2} [Z_1(k_{le}r_h)]^2} \int_{r_h}^{r_0} Z_1(k_{le}r) dr\end{aligned}\quad (D-8)$$

The Eigenvalues could be the same as those calculated for the first order when finding the P_{mn} and A'_{mn} coefficients.

Substituting Equations (D-7) into Equation (D-6) and replacing A_{mn} by A'_{mn} as defined by Equation (46), leads to:

$$\begin{aligned}& \left\{ \left[S \sum_l \alpha_{le} \right] + i \left[S \sum_l \lambda_{le} + T \sum_l \gamma_{le} \right] \frac{m}{k_{mn}} \right\} C_{mn} \\ &= \left[\left(\frac{U}{k_{mn}} \sum_l \lambda_{le} + \frac{C^{2k_{mn}d}}{k_{mn}} \sum_l \gamma_{le} \right) P_{mn} - \frac{1}{k_{mn}} \sum_l \lambda_{le} A'_{mn} \right] \\ & \quad - i \left[\frac{U}{m} \sum_l \alpha_{le} P_{mn} - \frac{1}{m} \sum_l \alpha_{le} A'_{mn} \right]\end{aligned}\quad (D-9)$$

Consider Equation (D-9) of the form:

$$(A + iB) C_{mn} = C - iD \quad (\text{D-10})$$

C_{mn} can then be written:

$$C_{mn} = E - iF \quad (\text{D-11})$$

where:

$$E = \left[\frac{AC - BD}{A^2 + B^2} \right] \quad (\text{D-12})$$

and

$$F = \left[\frac{AD + BC}{A^2 + B^2} \right] \quad (\text{D-13})$$

APPENDIX E

COMPUTATIONAL PROCEDURES

Bessel Function Subroutine

To effectively program the theoretical calculations on the computer, a Bessel function subroutine was necessary. Because the range of arguments was so large this subroutine would have to switch from the regular expansions to the asymptotic expansions at some prescribed argument. Finally the subroutine would have to be able to compute the Bessel functions for any order.

The regular expansions for Bessel functions of both kinds are given as:

$$J_m(x) = \sum_{s=0}^{\infty} (-1)^s \frac{(\frac{1}{2}x)^{m+2s}}{s!(m+s)!} \quad (\text{E-1})$$

and

$$\begin{aligned} \pi Y_m(x) = & 2 \left\{ \gamma + \ln\left(\frac{1}{2}x\right) \right\} J_m(x) \\ & - \sum_{s=0}^{m-1} \frac{(m-s-1)}{s!} \left(\frac{1}{2}x\right)^{-m+2s} \\ & - \sum_{s=0}^{\infty} (-1)^s \frac{(\frac{1}{2}x)^{m+2s}}{s!(m+s)!} \left(1 + \frac{1}{2} + \dots + \frac{1}{s} \right. \\ & \quad \left. + 1 + \frac{1}{2} + \dots + \frac{1}{m+s} \right) \quad (\text{E-2}) \end{aligned}$$

where $\gamma = 0.577216$.

These expansions were programmed to include terms up to the point where the absolute value of additional terms was less than 0.000001. With this accuracy it was determined that these expansions were useable up to an argument of 7.0. Beyond that point asymptotic expansions were adequate. The asymptotic expansions are given as:

$$J_m(x) = \sqrt{2/\pi x} \left\{ P_m(x) \cos \xi_m - Q_m(x) \sin \xi_m \right\} \quad (\text{E-3})$$

$$Y_m(x) = \sqrt{2/\pi x} \left\{ Q_m(x) \cos \xi_m + P_m(x) \sin \xi_m \right\} \quad (\text{E-4})$$

where:

$$\xi_m = x - \frac{1}{2} \left(m + \frac{1}{2} \right) \pi \quad (\text{E-5})$$

$$P_m(x) \sim 1 - \frac{(m-1)(m-9)}{2!(8x)^2} + \frac{(m-1)(m-9)(m-25)(m-49)}{4!(8x)^4} - \dots \quad (\text{E-6})$$

$$Q_m(x) \sim \frac{(M-1)}{8x} - \frac{(M-1)(M-9)(M-17)}{3! (8x)^3} + \dots \quad (\text{E-7})$$

$$\mu = 4 m^2 \quad (\text{E-8})$$

The specific procedure followed was to compute the Bessel functions of both kinds by the expansion commensurate with the argument for orders of 0 and 1. The following recurrence formulae were then used to successively increase the order of the Bessel functions to the one desired:

$$J_{m+1}(x) = (2m/x) J_m(x) - J_{m-1}(x) \quad (\text{E-9})$$

$$Y_{m+1}(x) = (2m/x) Y_m(x) - Y_{m-1}(x) \quad (\text{E-10})$$

Integrations

All integrations in the computational procedure were performed on the basis of the trapezoidal rule. In other words for a definite integral of the type:

$$\int_{x_0}^{x_n} y \, dx \quad (\text{E-11})$$

the integration was interpreted geometrically as an area.

The area was taken as the sum of n trapezoids so that:

$$\int_{x_0}^{x_n} y \, dx = \int_0^x y \, dx + \int_{x_1}^{x_2} y \, dx + \dots + \int_{x_{n-1}}^{x_n} y \, dx \quad (\text{E-12})$$

or

$$\int_{x_0}^{x_n} y \, dx = \frac{\Delta x}{2} (y_0 + 2y_1 + 2y_2 + \dots + 2y_{n-1} + y_n) \quad (\text{E-13})$$

Equation (E-13) implies a constant Δx or a series of trapezoids of equal height. All integrations that were performed were for constant Δx values that were sufficiently small to insure an accurate summation.

Other Computations

The rest of the computations that were performed were of a straightforward nature. The only deviations that arose were with large exponential values. This aspect of the computations is discussed separately in Appendix F.

APPENDIX F

REDUCTION OF C_{mn} EQUATION

For reasons of handling ease the following definitions are made:

$$\begin{aligned}\alpha &= \sum_l \alpha_{l2} \\ \gamma &= \sum_l \gamma_{l2} \\ \lambda &= \sum_l \lambda_{l2}\end{aligned}\tag{F-1}$$

In Equation (D-12) and AC and BD terms in the numerator can be written as follows:

$$\begin{aligned}AC &= \frac{S\lambda\alpha}{k_{mn}} e^{2k_{mn}d} P_{mn} - \frac{S\lambda\alpha}{k_{mn}} P_{mn} \\ &\quad + \frac{S\gamma\alpha}{k_{mn}} e^{2k_{mn}d} P_{mn} - \frac{S\lambda\alpha}{k_{mn}} A'_{mn}\end{aligned}\tag{F-2}$$

$$\begin{aligned}BD &= \frac{S\lambda\alpha}{k_{mn}} e^{2k_{mn}d} P_{mn} - \frac{S\lambda\alpha}{k_{mn}} P_{mn} \\ &\quad - \frac{S\lambda\alpha}{k_{mn}} A'_{mn} + \frac{UT\alpha\gamma}{k_{mn}} P_{mn} - \frac{T\alpha\gamma}{k_{mn}} A'_{mn}\end{aligned}\tag{F-3}$$

A number of like terms cancel when BD is subtracted from AC and upon substituting for S, T, and U from Equations (D-5):

$$AC - BD = -e^{2k_{mn}d} (e^{k_{mn}d} - 2e^{-k_{mn}d} + e^{-3k_{mn}d}) \frac{\alpha \gamma}{k_{mn}} P_{mn} \\ + e^{2k_{mn}d} (e^{k_{mn}d} - e^{-3k_{mn}d}) \frac{\alpha \gamma}{k_{mn}} A'_{mn} \quad (F-4)$$

The $e^{2k_{mn}d}$ term outside the parentheses will cancel with a similar term in the denominator of Equation (D-12) so that at the higher $k_{mn}d$ values the level of the AC - BD term is governed very much by $e^{k_{mn}d}$ and not by the extremely high values resulting from S, T, and U.

In the case of Equation (D-13) AD + BC does not provide any fortunate term cancellation. However, when considering higher values of $k_{mn}d$, certain terms become so large compared to others that they can be considered alone.

The AD and BC terms can be expanded to the following form:

$$AD = e^{5k_{mn}d} \left(\frac{\alpha^2}{m} \right) P_{mn} - e^{3k_{mn}d} \left(\frac{\alpha^2}{m} \right) (3P_{mn} + A'_{mn}) \quad (F-5)$$

$$BC = e^{5k_{mn}d} \left(\frac{m}{k_{mn}^2} P_{mn} \right) (\lambda^2 + 2\lambda\gamma + \gamma^2) - e^{3k_{mn}d} \left(\frac{m}{k_{mn}^2} P_{mn} \right) (2\lambda^2 + 3\lambda\gamma) \\ - e^{3k_{mn}d} \left(\frac{m}{k_{mn}^2} A'_{mn} \right) (\lambda^2 + \lambda\gamma) \quad (F-6)$$

In both Equation (F-5) and Equation (F-6) terms multiplied by exponentials smaller than $e^{3k_{mn}d}$ were dropped. In fact when $k_{mn}d$ is large enough, terms multiplied by $e^{3k_{mn}d}$ will have no significance compared to terms multiplied by $e^{5k_{mn}d}$. AD + BC could then finally be written as:

$$AD + BC = e^{5k_{mn}d} \frac{P_{mn}}{m} \left[\alpha^2 + \frac{m^2}{k_{mn}^2} (\lambda + \gamma)^2 \right] \quad (\text{F-7})$$

A similar reduction of terms can be performed for the denominator so that

$$A^2 + B^2 = e^{6k_{mn}d} \left[\alpha^2 + \frac{m^2}{k_{mn}^2} (\lambda + \gamma)^2 \right] \quad (\text{F-8})$$

This leads finally to the expression:

$$F = e^{-k_{mn}d} \frac{P_{mn}}{m} \quad (\text{F-9})$$

when $e^{k_{mn}d}$ is sufficiently large.

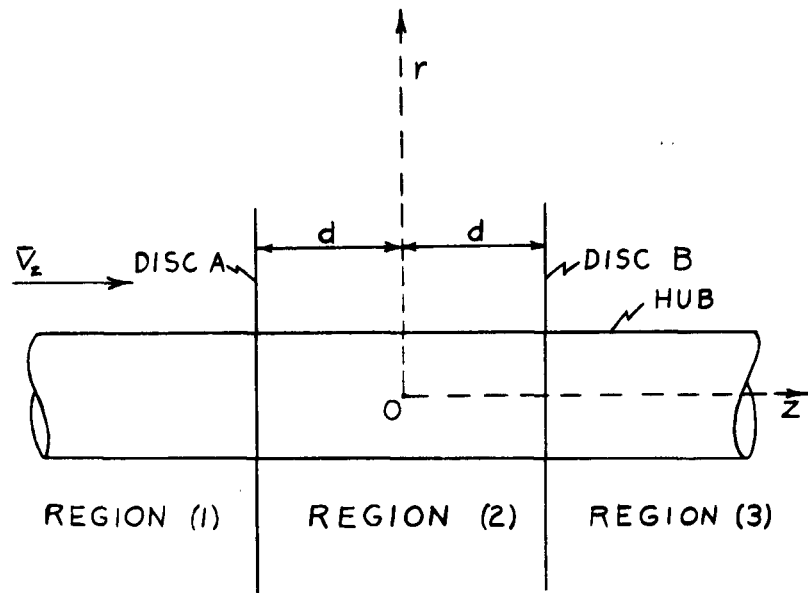


Fig. 1 Theoretical Model for Flow Distortion Study

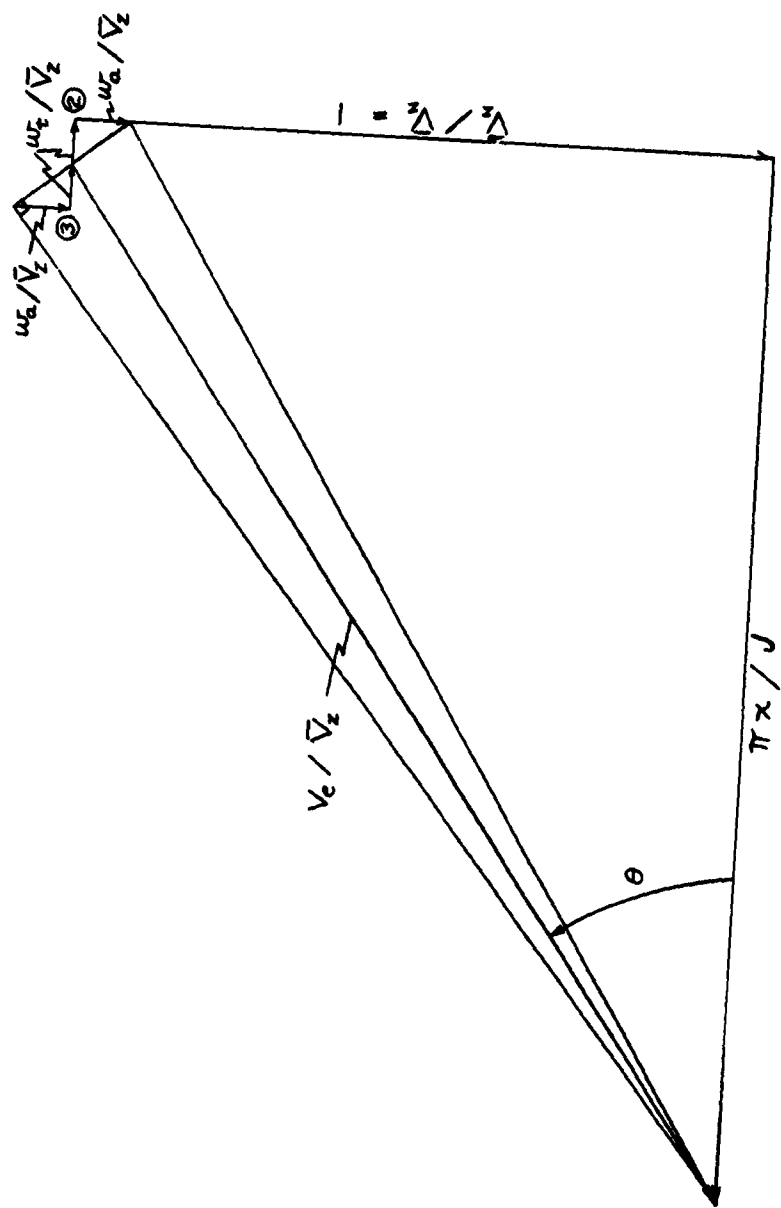


Fig. 2 Normal Velocity Diagram for Blade Section

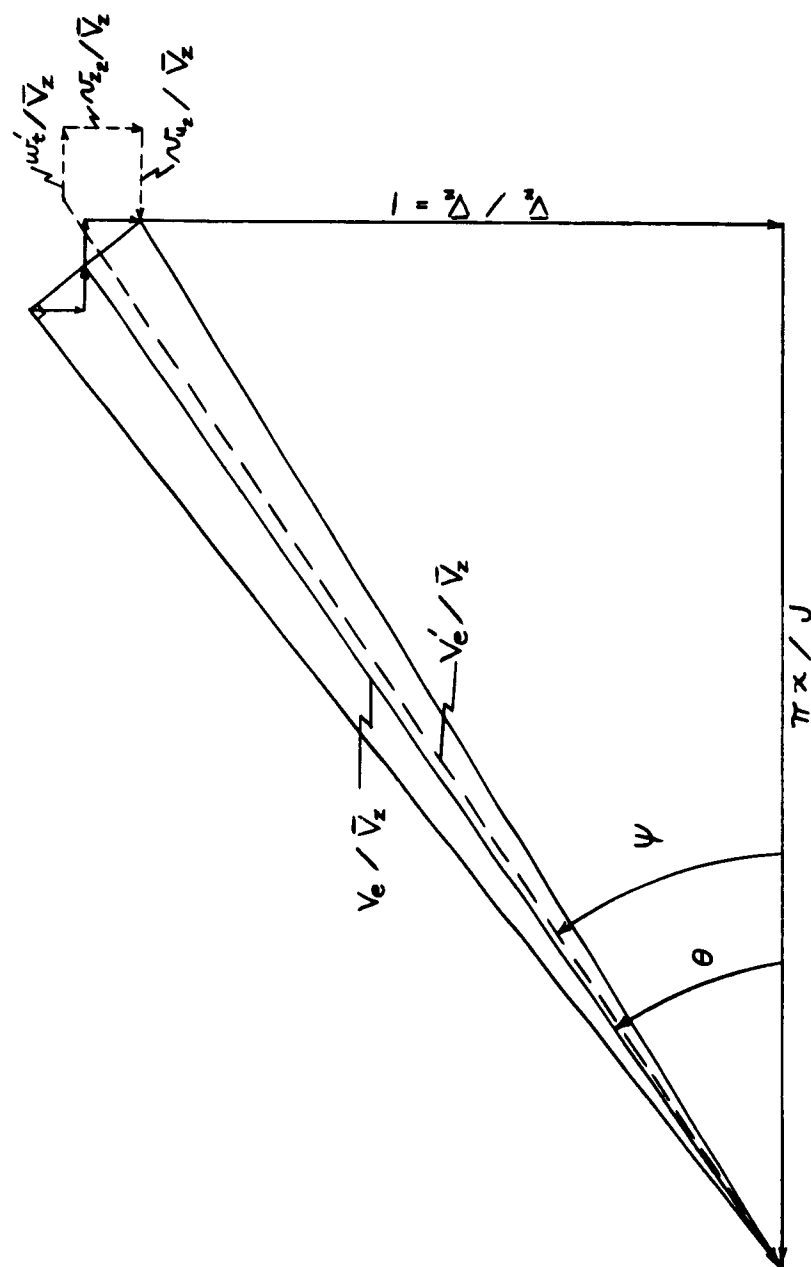


Fig. 3 Velocity Diagram of Blade Section in Distorted Flow

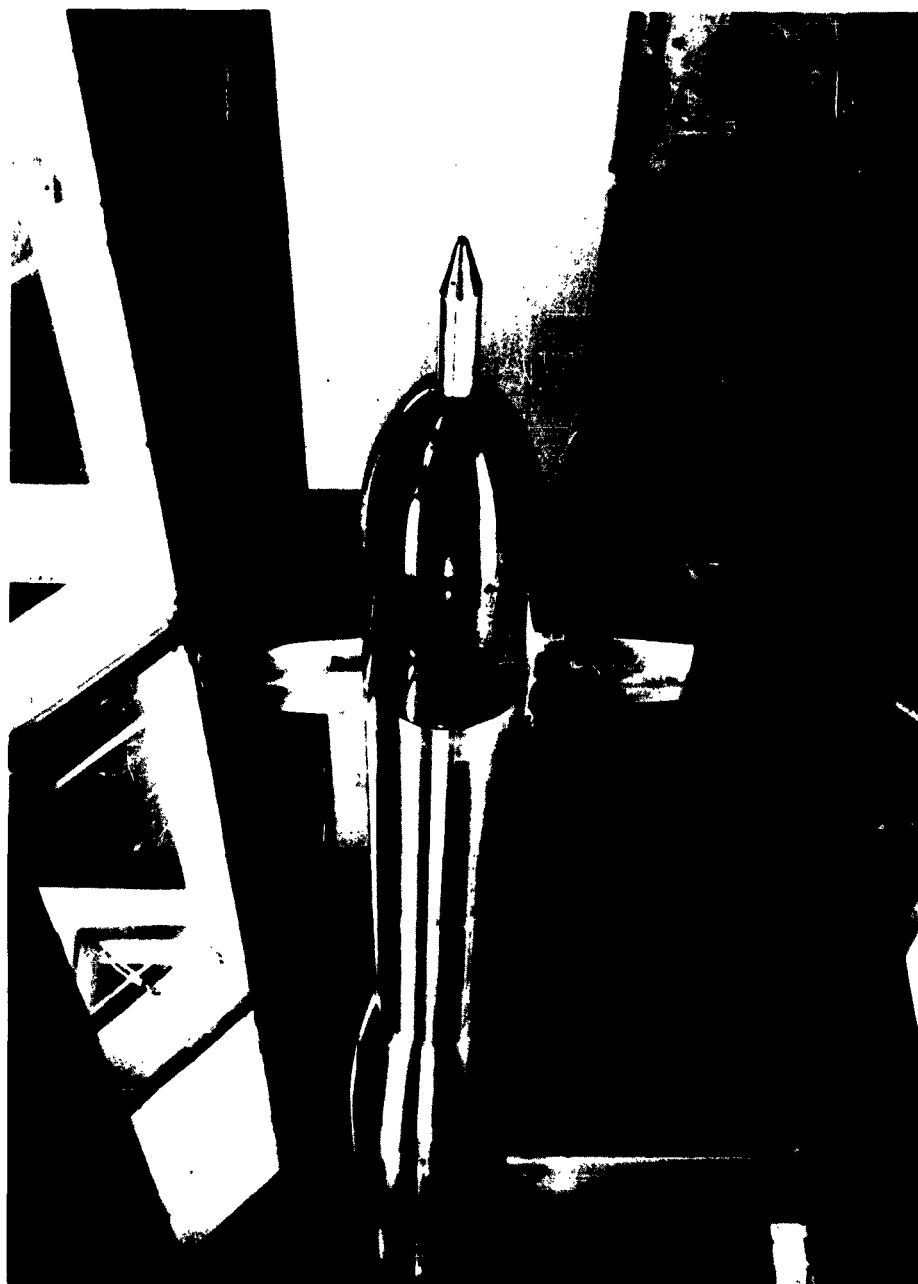


Fig. 4 Interim Model with Velocity Probe

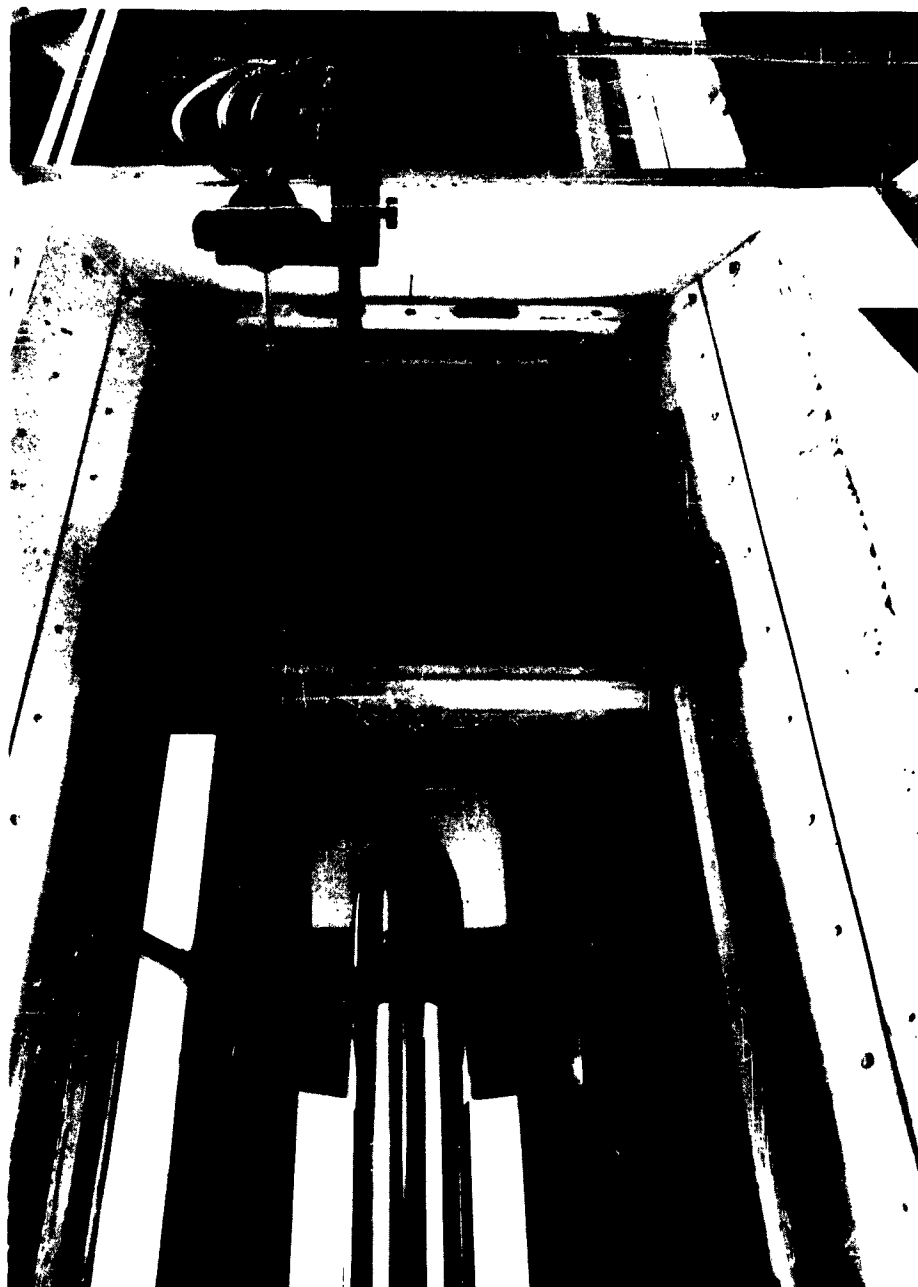


Fig. 5 Interim Model with Velocity Probe and Traversing Unit

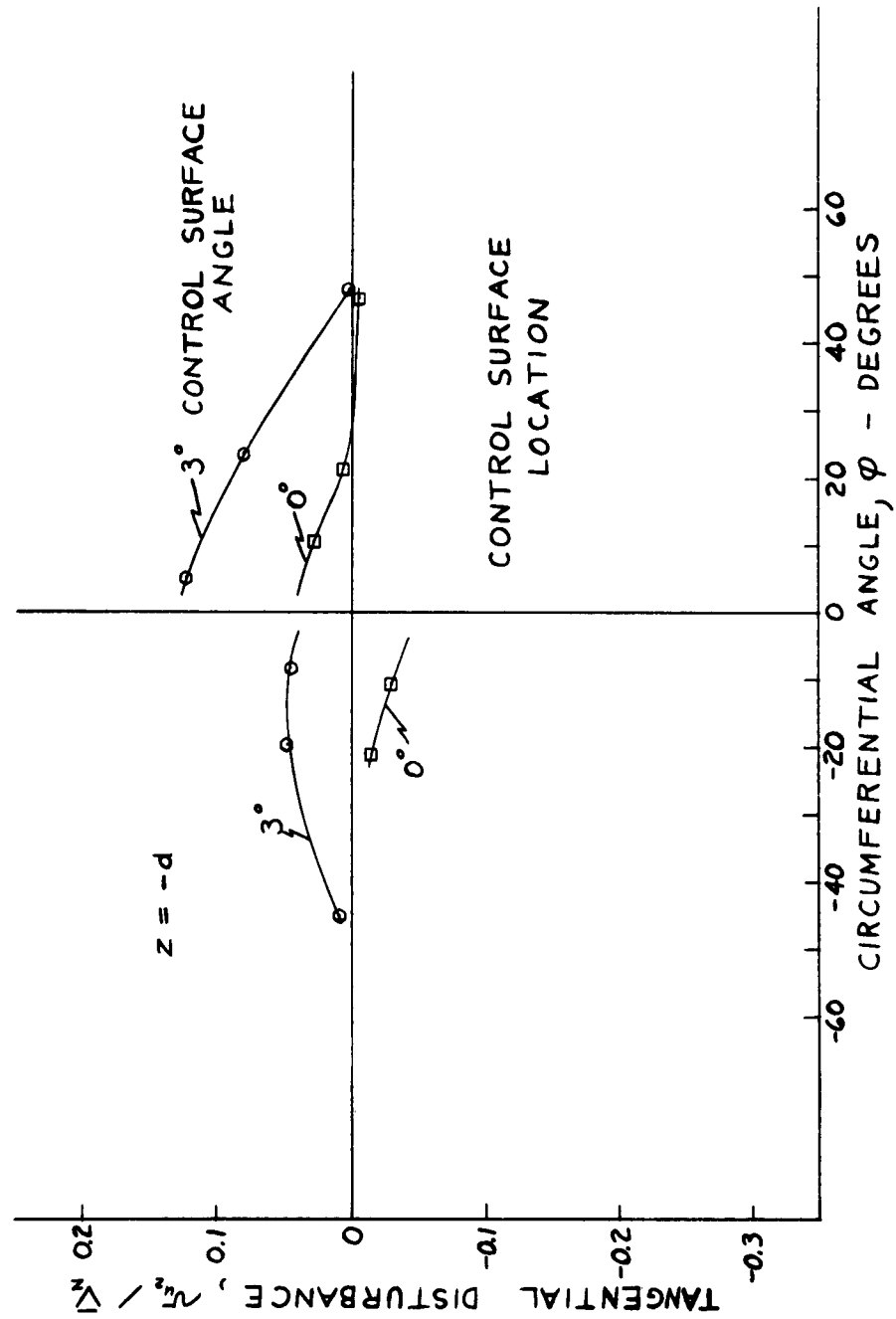


Fig. 6 Typical Results of Velocity Survey

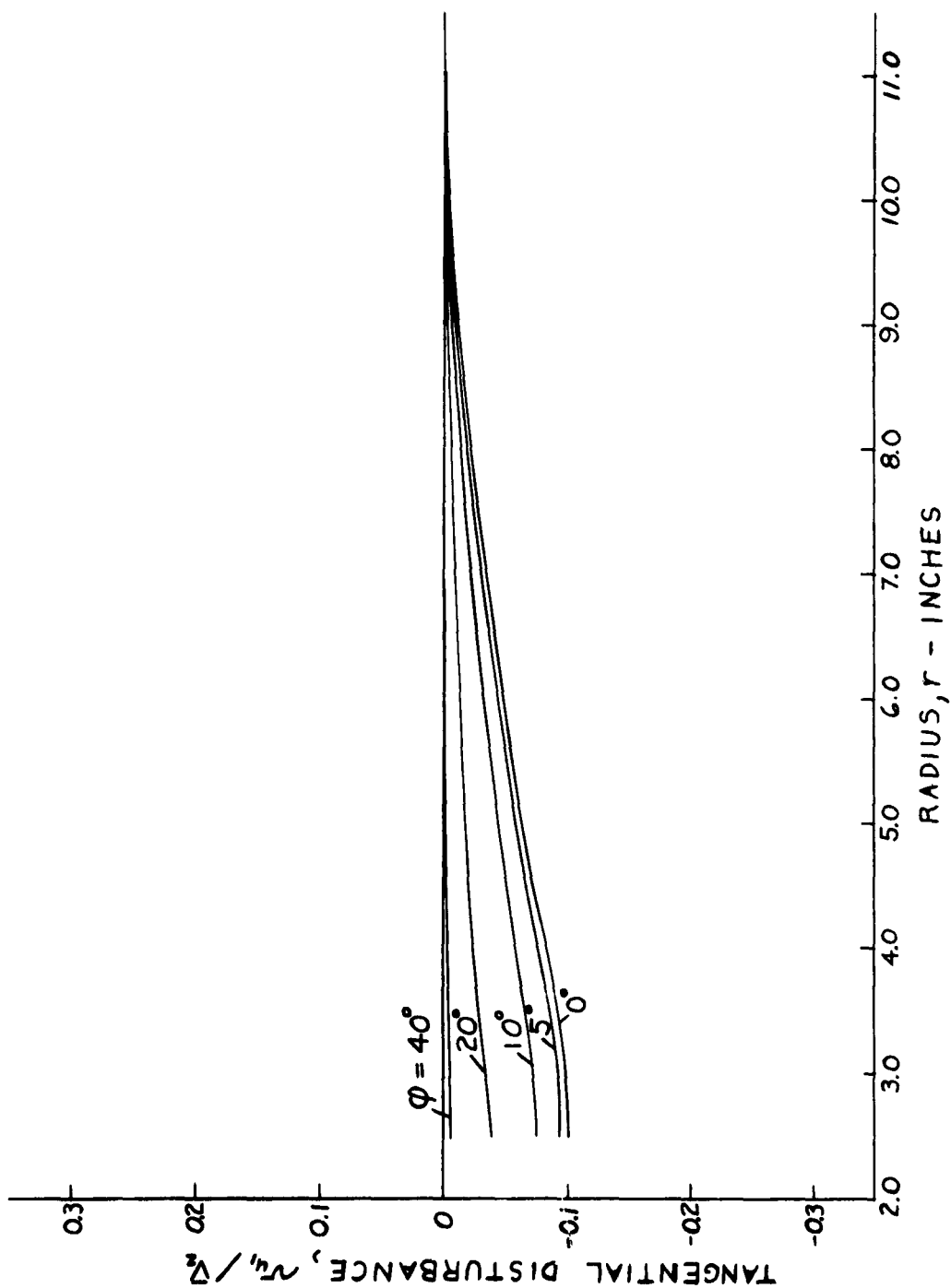


Fig. 7 Measured Distribution of v_{u1} at $z = -d$

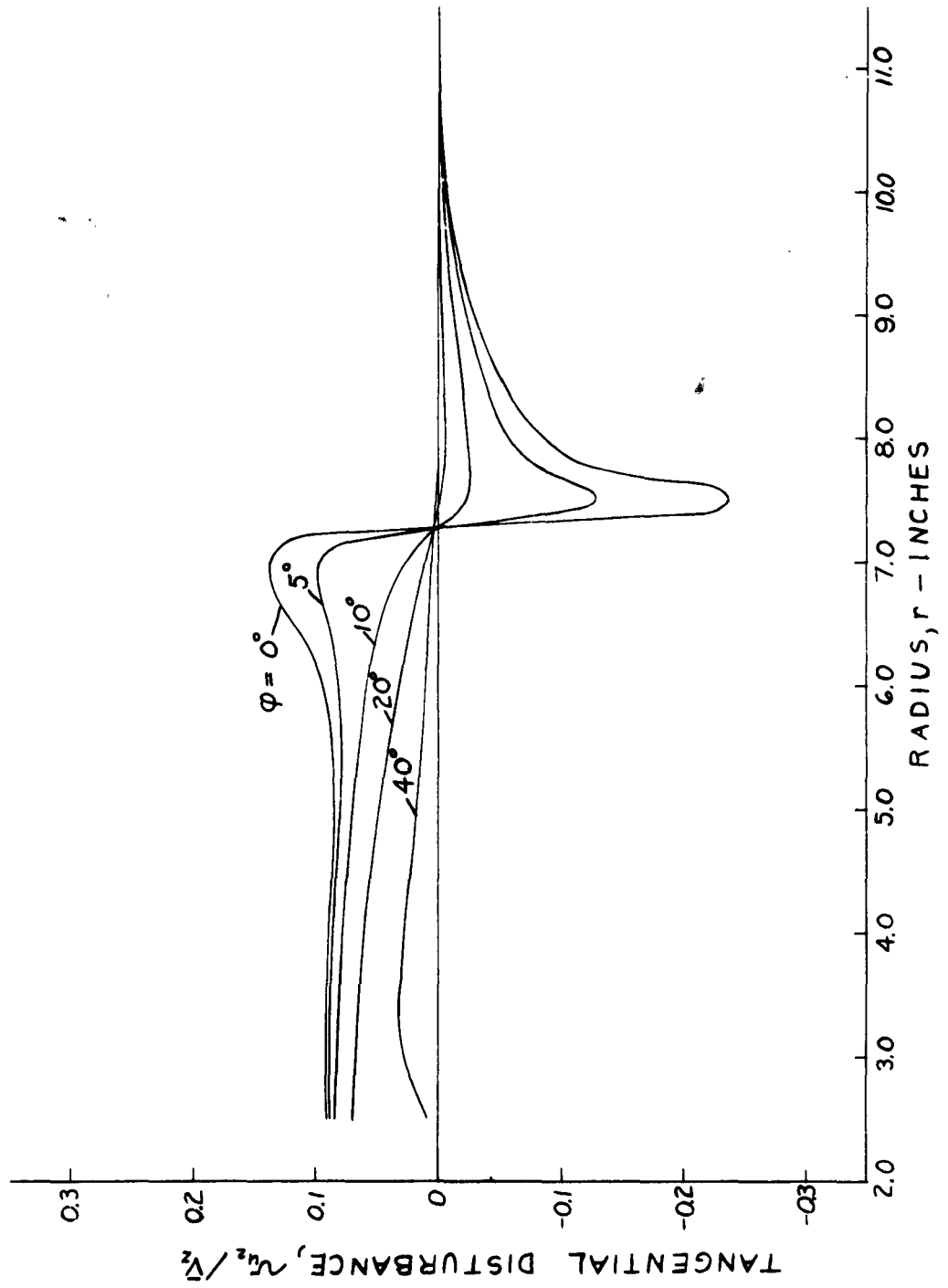


Fig. 8 Measured Distribution of v_{u_2} at $z = -d$

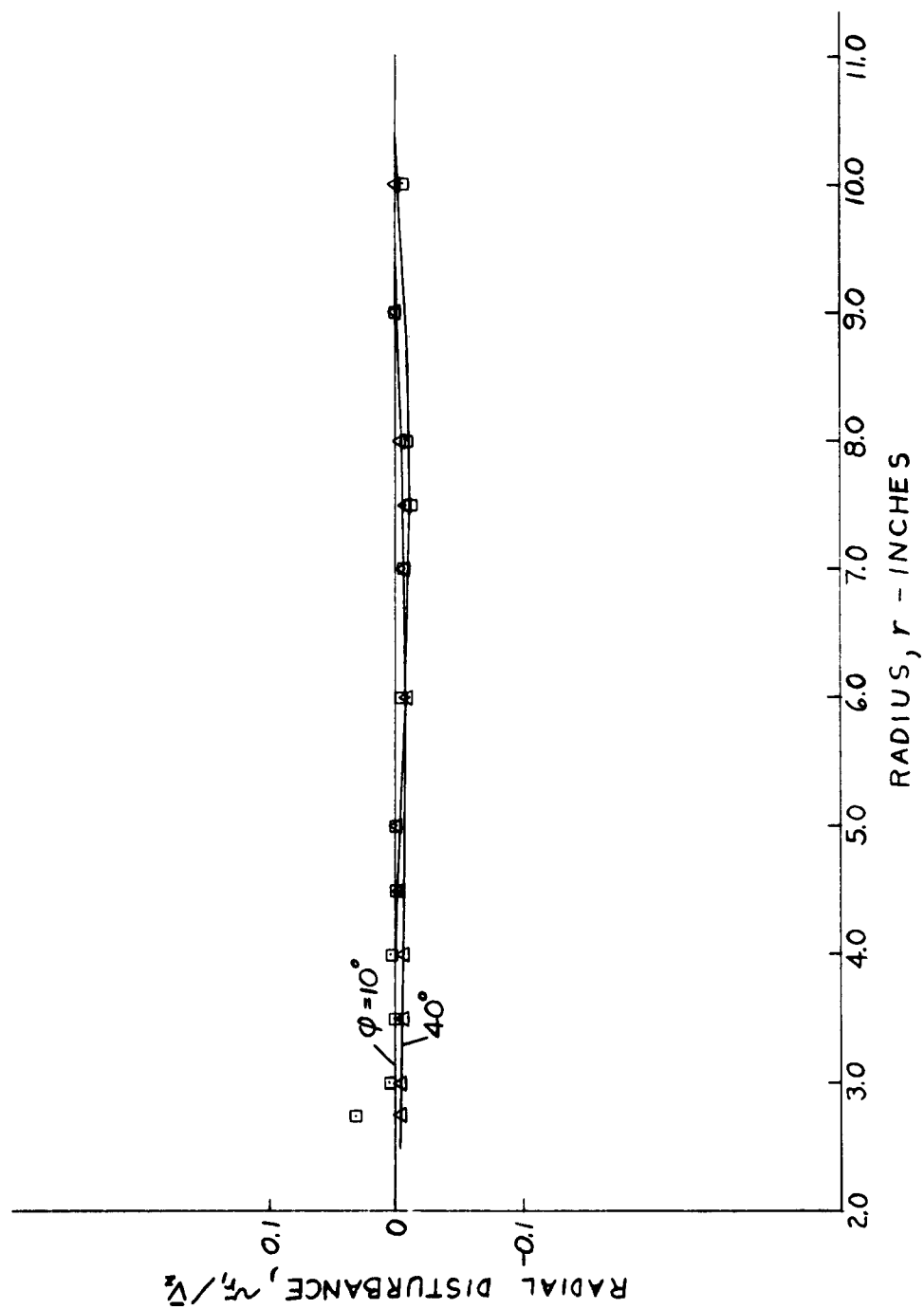


Fig. 9 Measured Distribution of v_{r_1} at $z = -d$

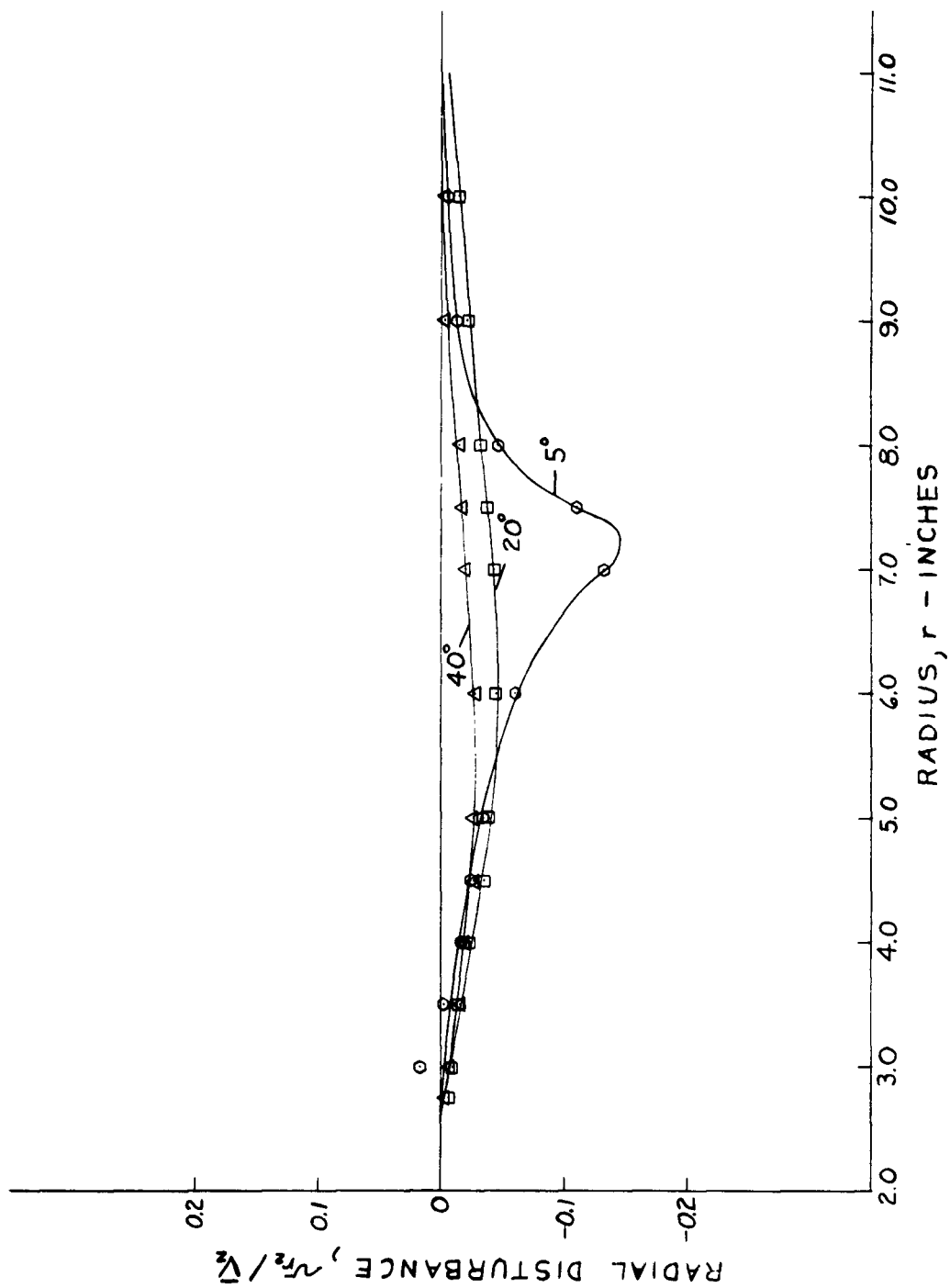


Fig. 10 Measured Distribution of v_{r2} at $z = -d$

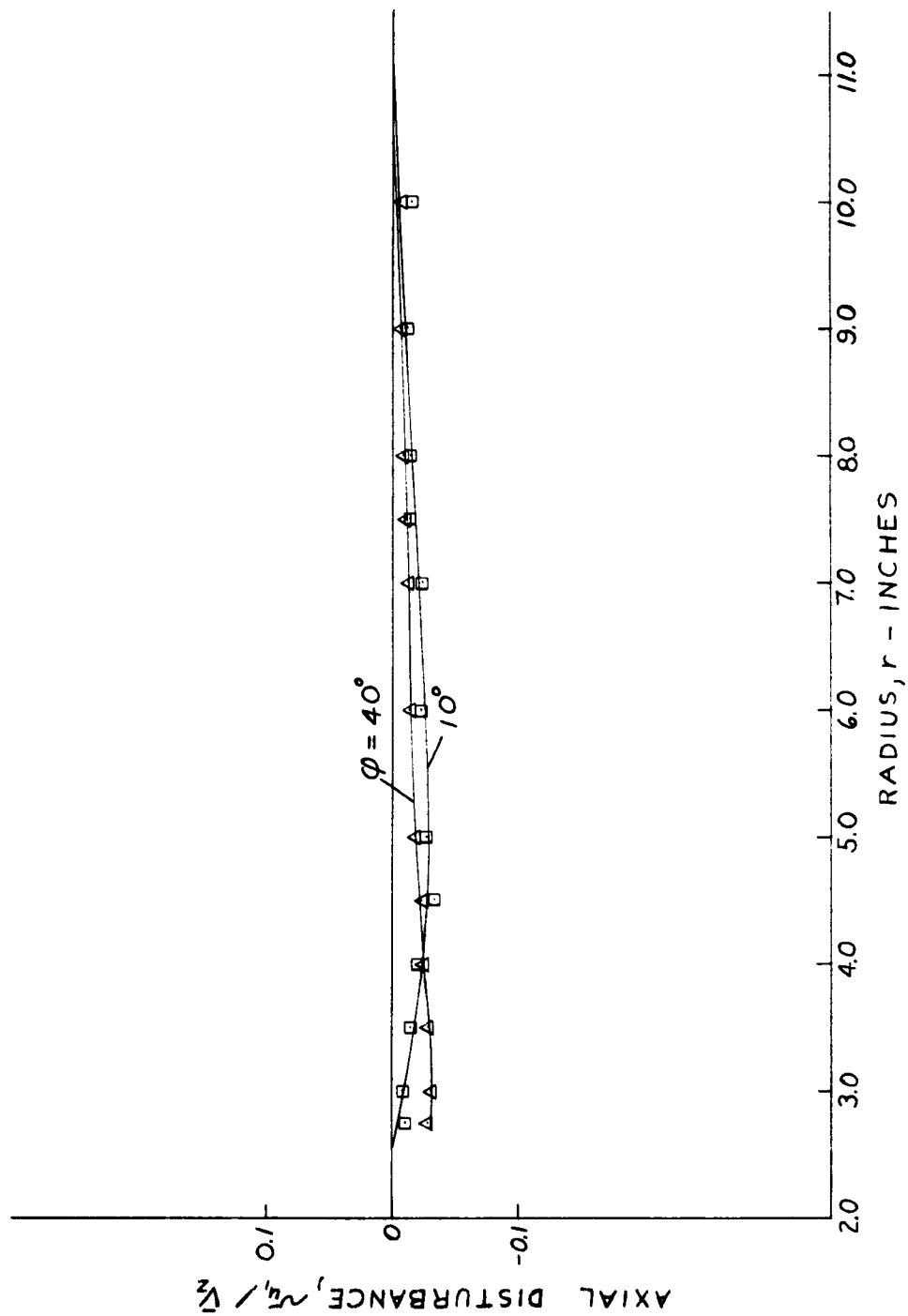


Fig. 11 Measured Distribution of v_{z_1} at $z = -d$

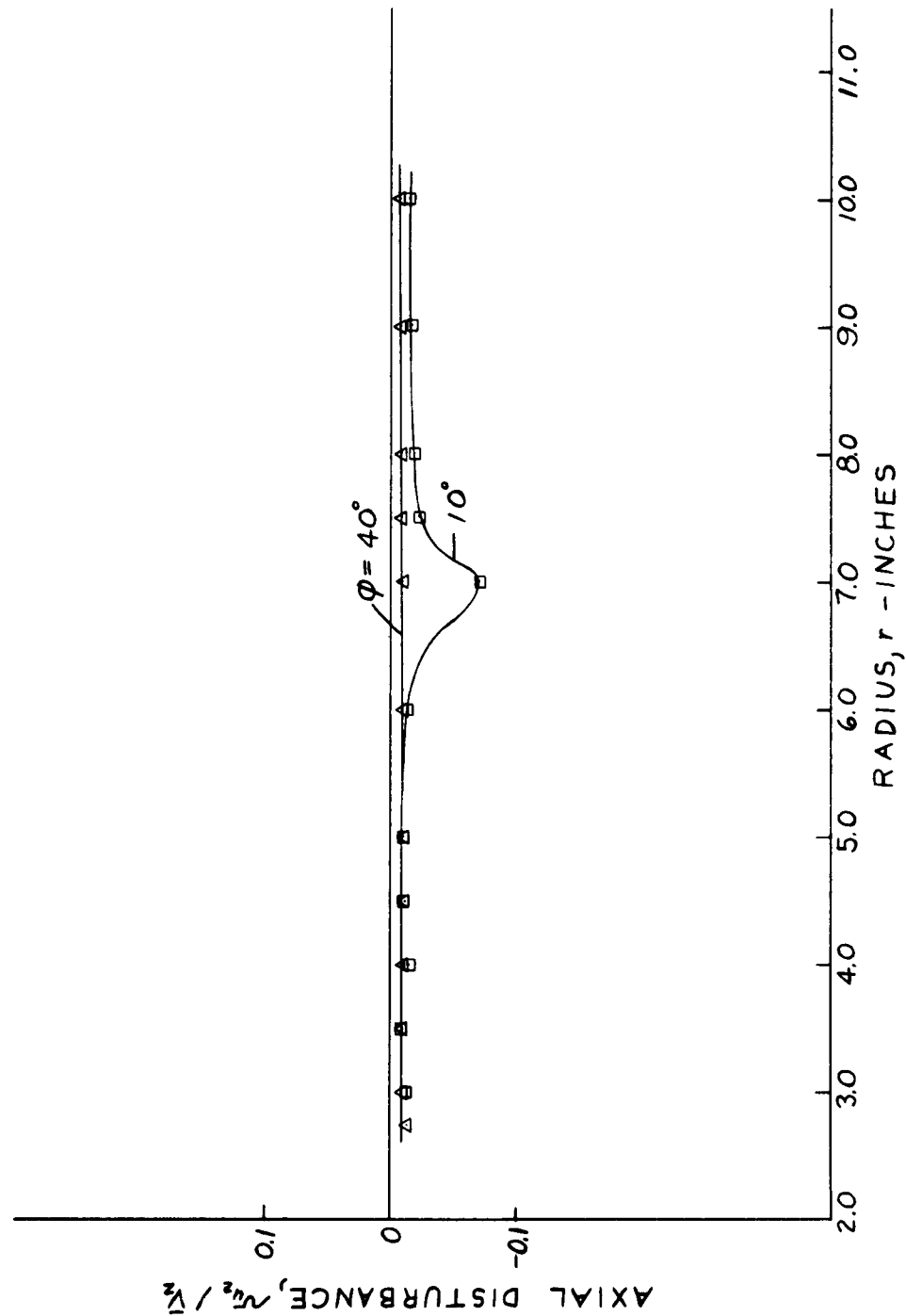


Fig. 12 Measured Distribution of v_{z_2} at $z = -d$

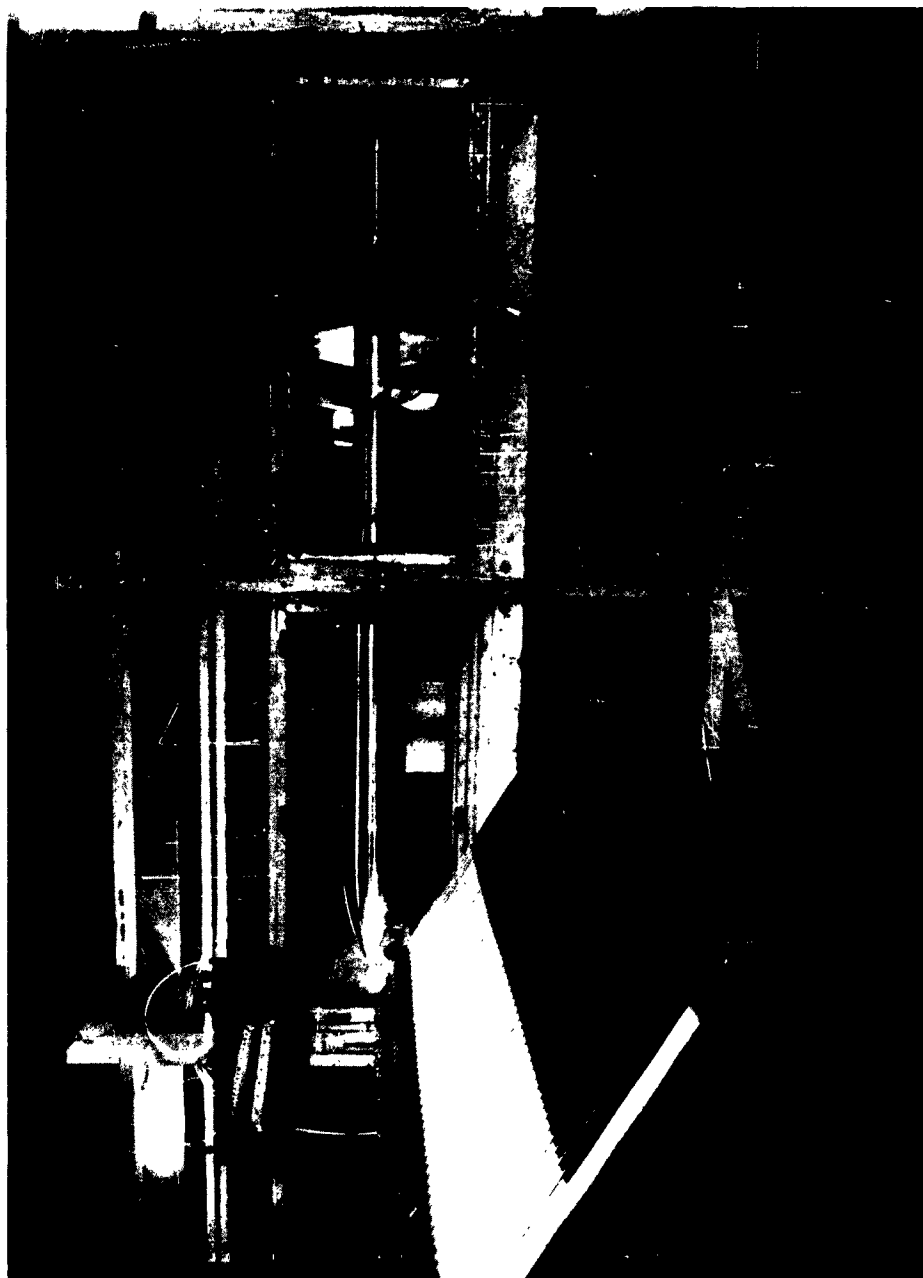


Fig. 13 Flow Distortion Model with 10-Bladed Propeller

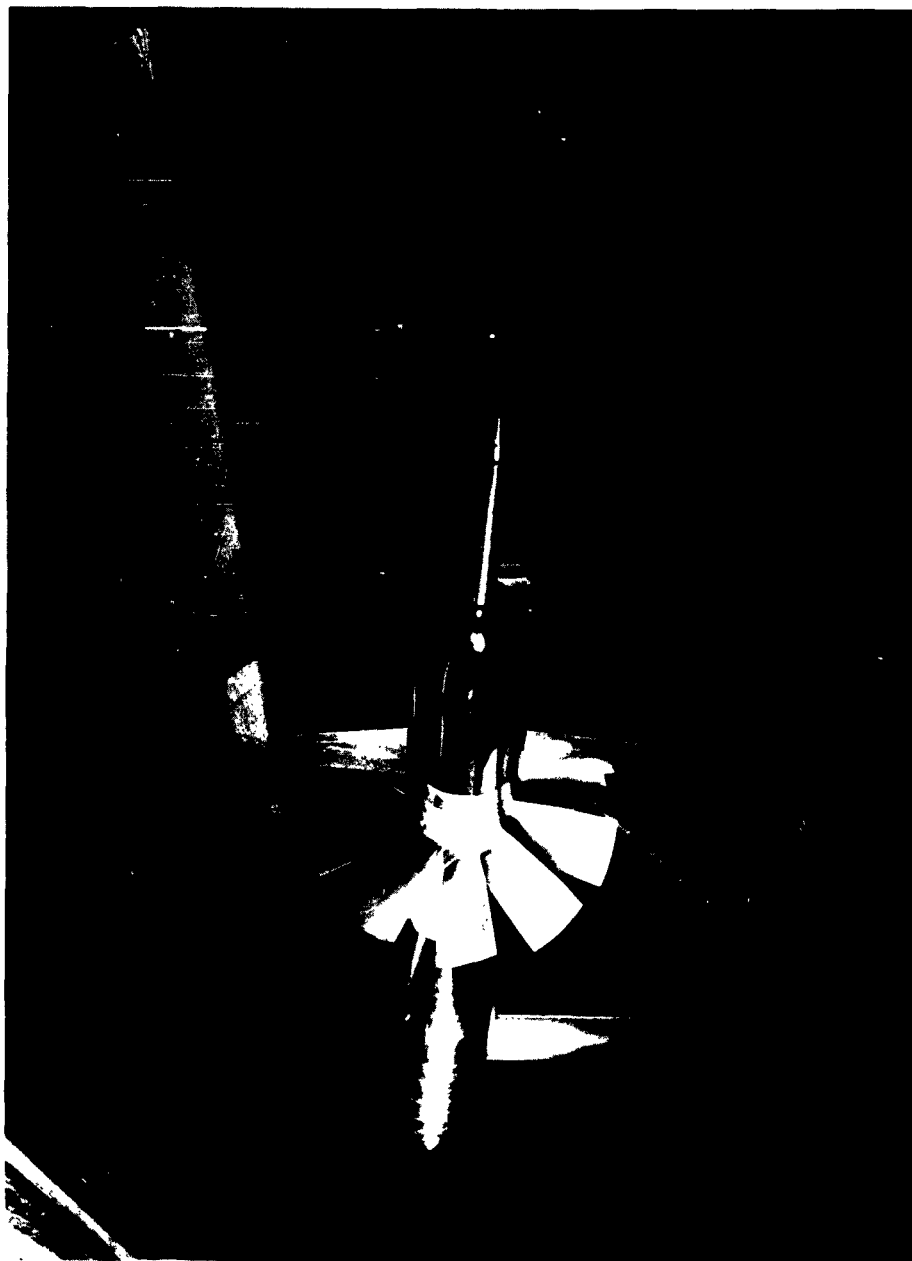


Fig. 14 View of Flow Distortion Model from Upstream
to Downstream

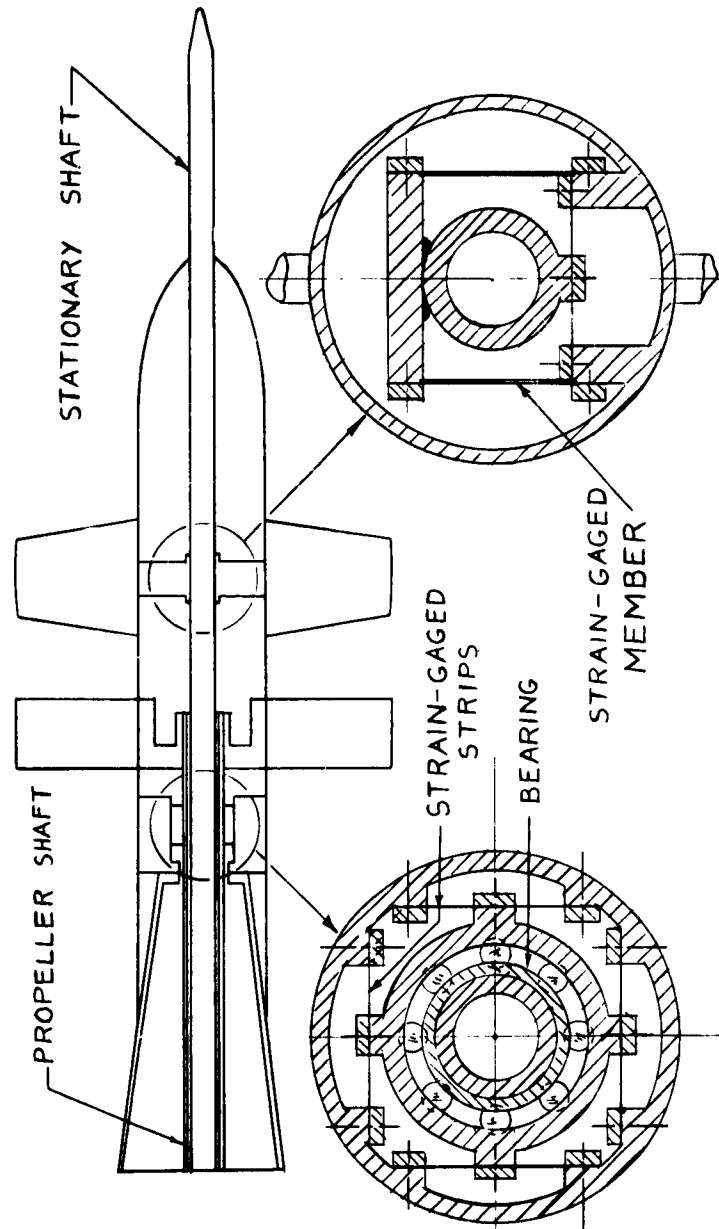


Fig. 15 Strain-Gaged Assemblies for Force Measurements

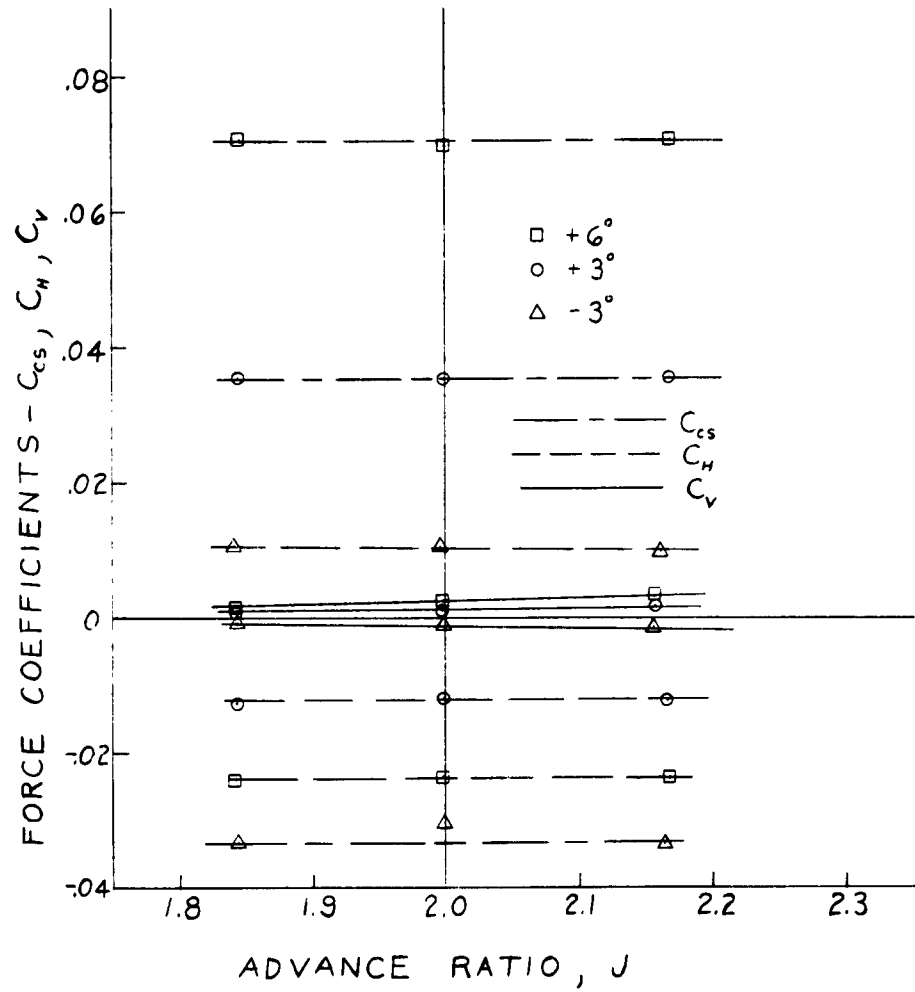


Fig. 16 Measured Force Coefficients for $d/R_p = 0.267$,
 $B = 10$

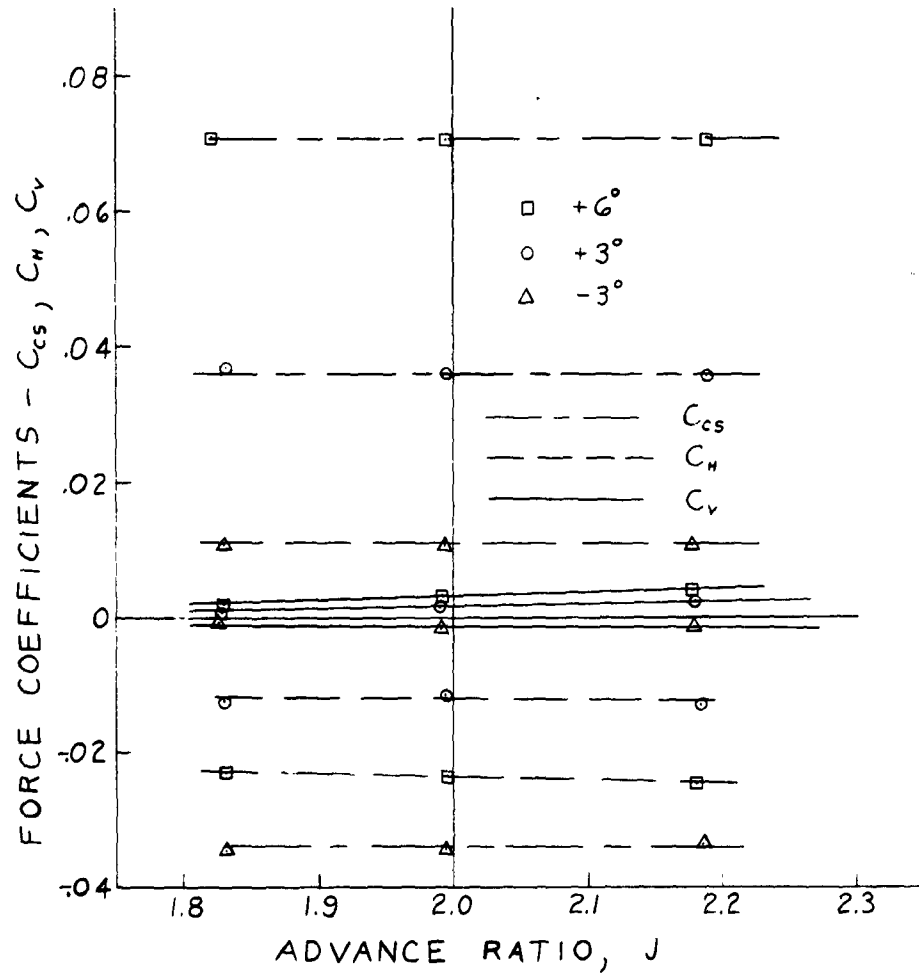


Fig. 17 Measured Force Coefficients for $d/R_p = 0.667$,
 $B = 10$

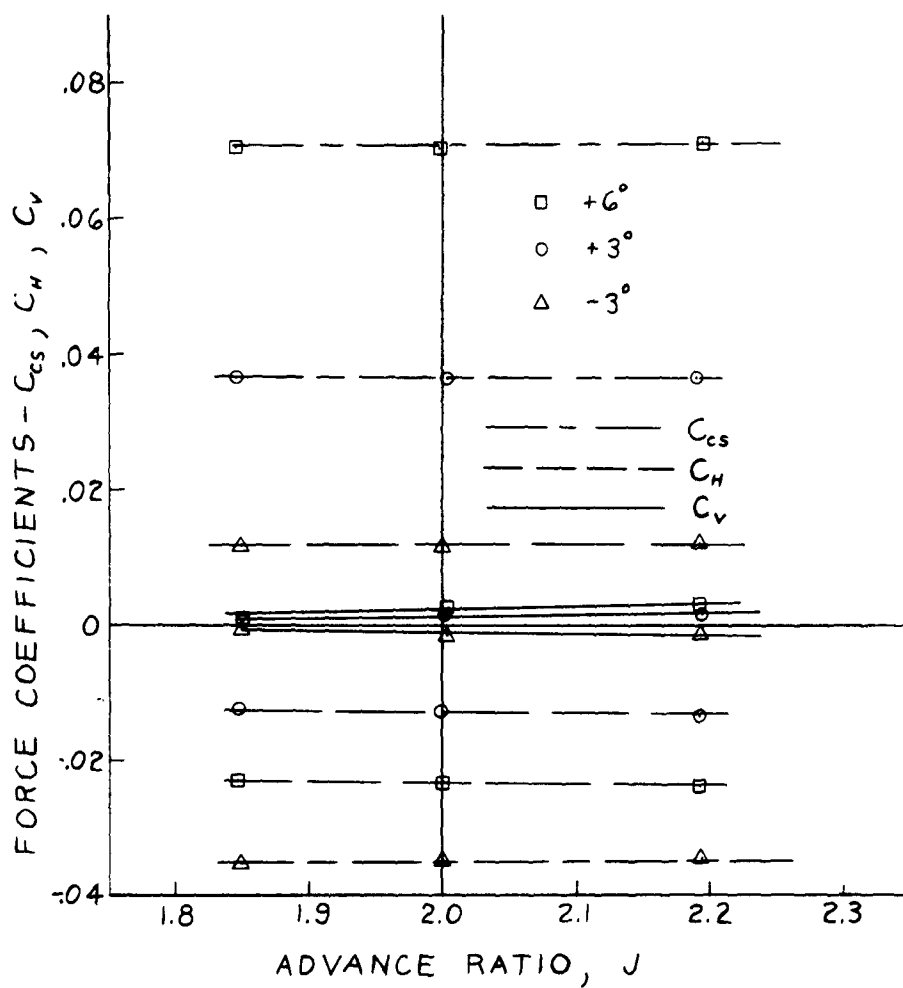


Fig. 18 Measured Force Coefficients for $d/R_p = 1.067$,
 $B = 10$

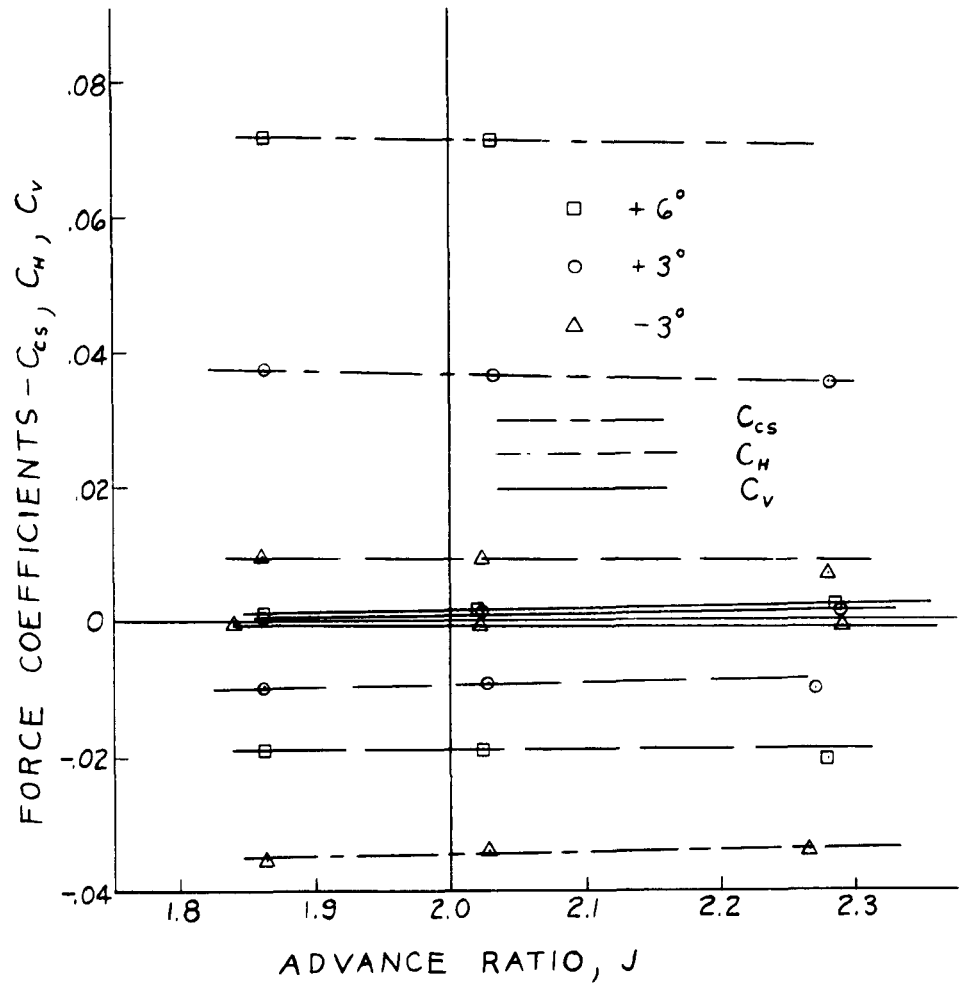


Fig. 19 Measured Force Coefficients for $d/R_p = 0.267$,
 $B = 5$

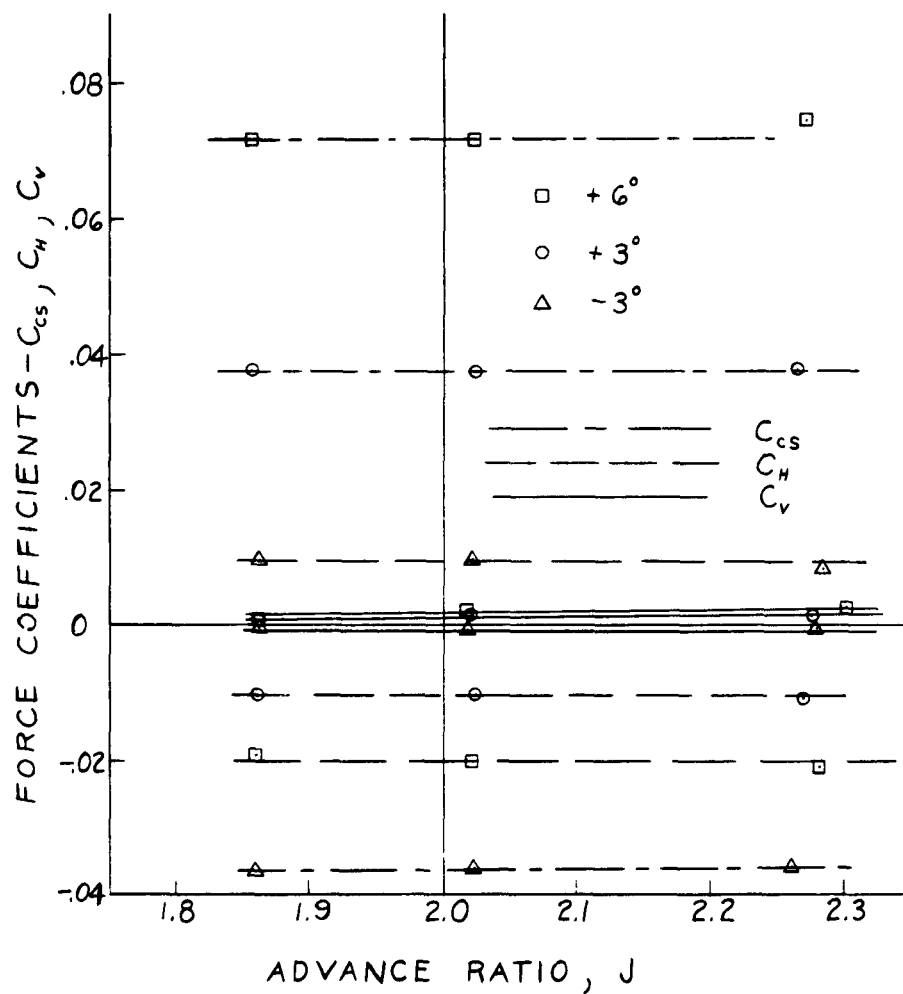


Fig. 20 Measured Force Coefficients for $d/R_p = 0.667$,
 $B = 5$

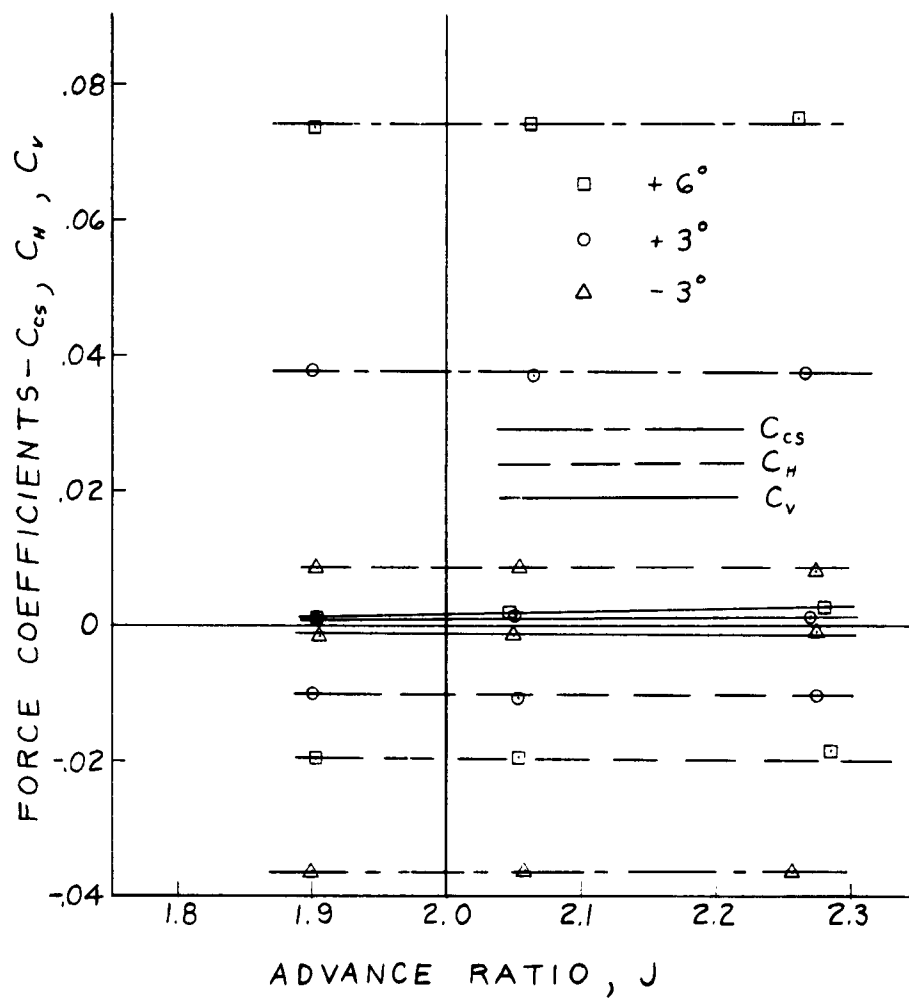


Fig. 21 Measured Force Coefficients for $d/R_p = 1.067$,
 $B = 5$

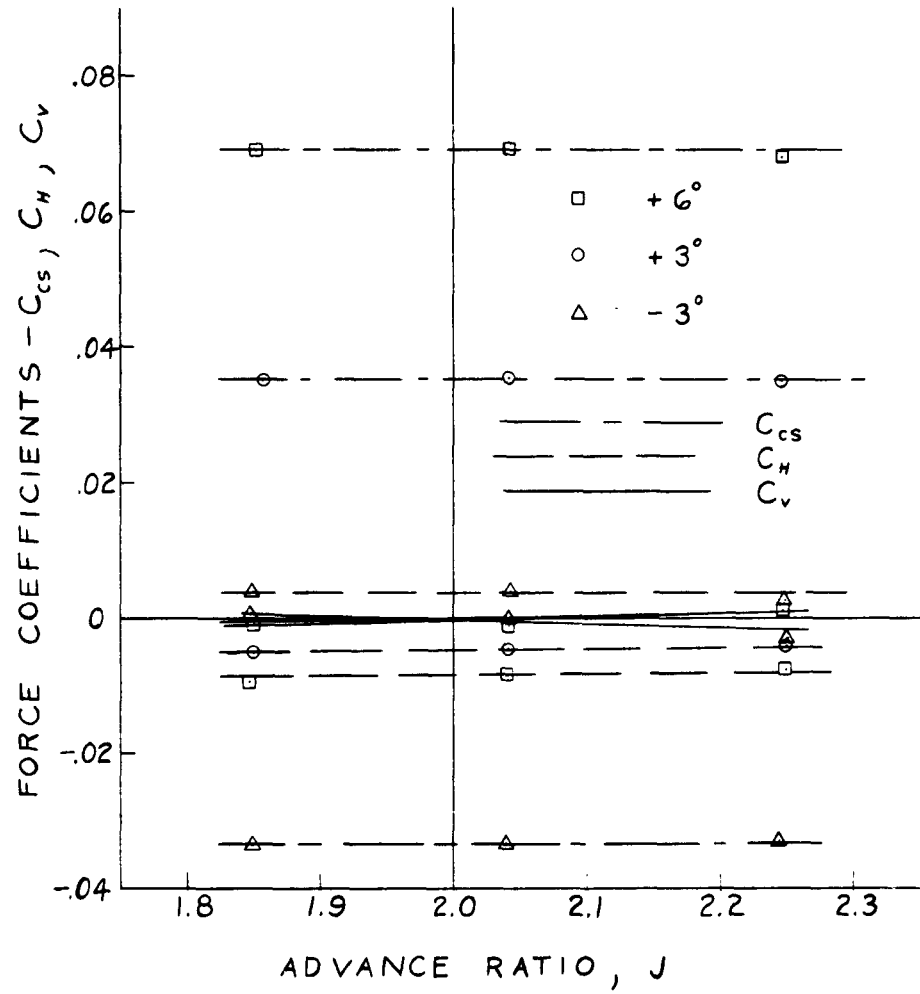


Fig. 22 Measured Force Coefficients for $d/R_p = 0.267$,
 $B = 2$

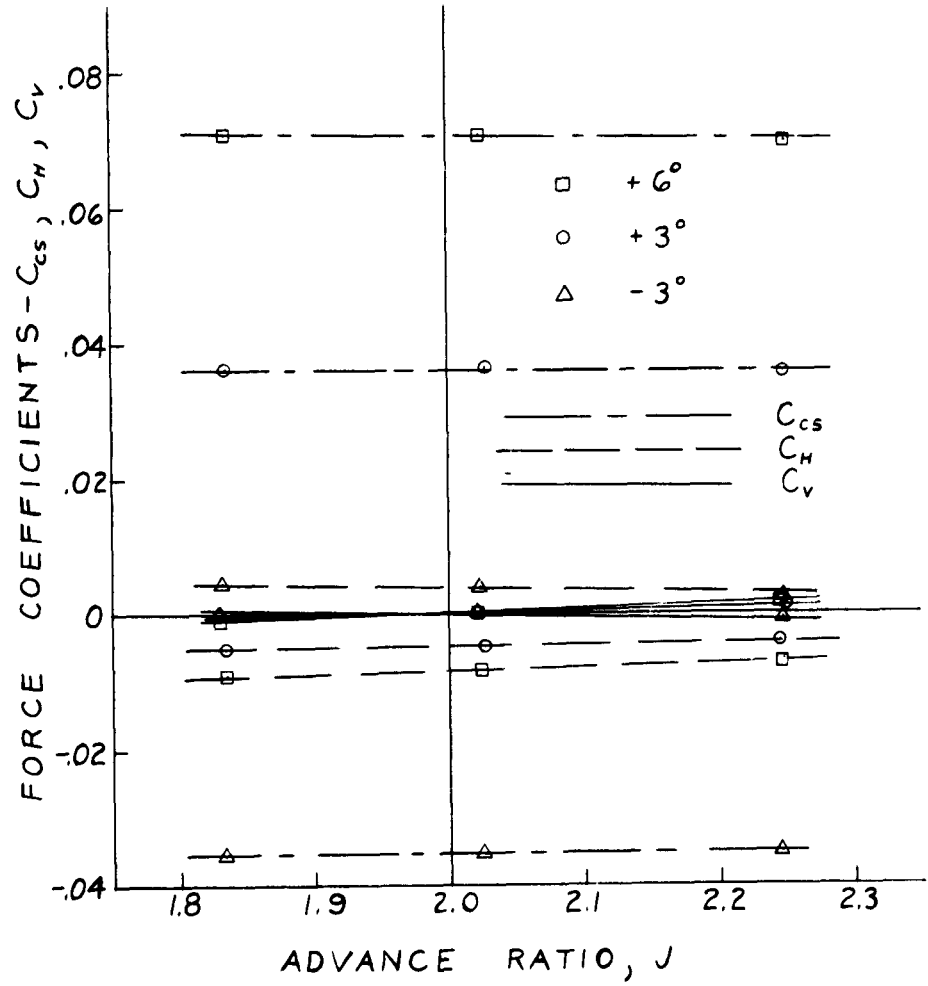


Fig. 23 Measured Force Coefficients for $d/R_p = 0.667$,
 $B = 2$

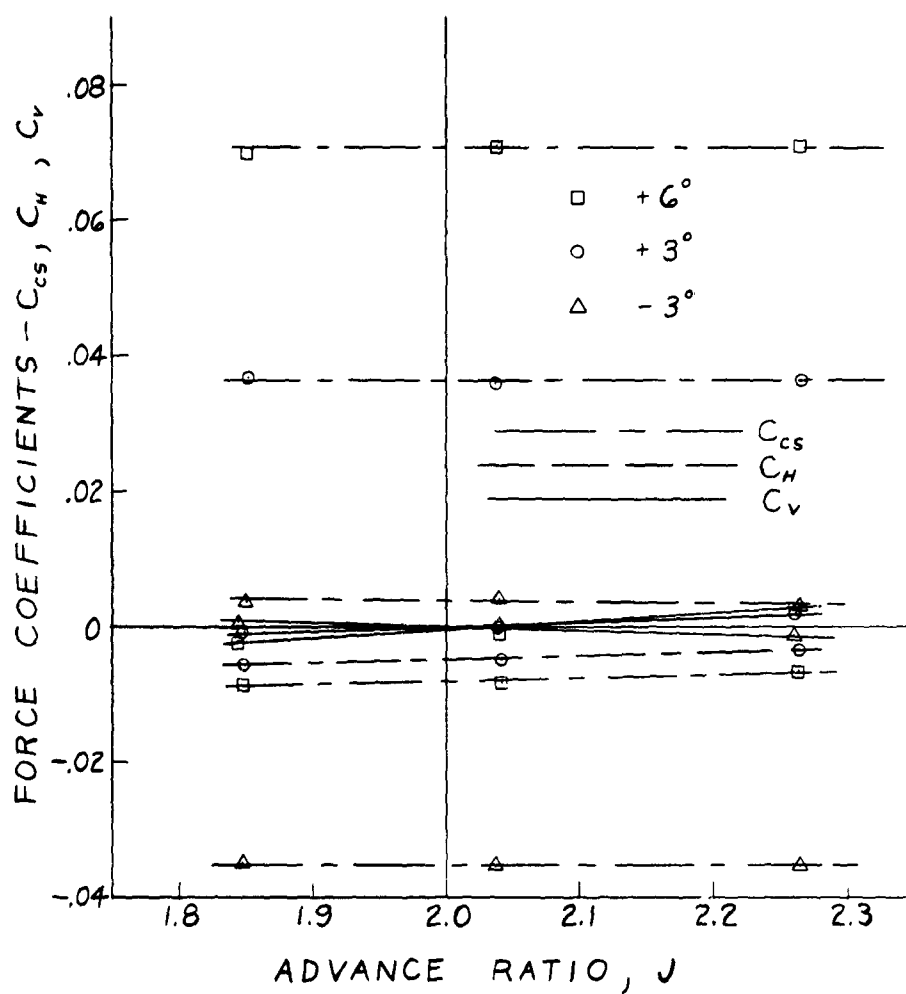


Fig. 24 Measured Force Coefficients for $d/R_p = 1.067$,
 $B = 2$

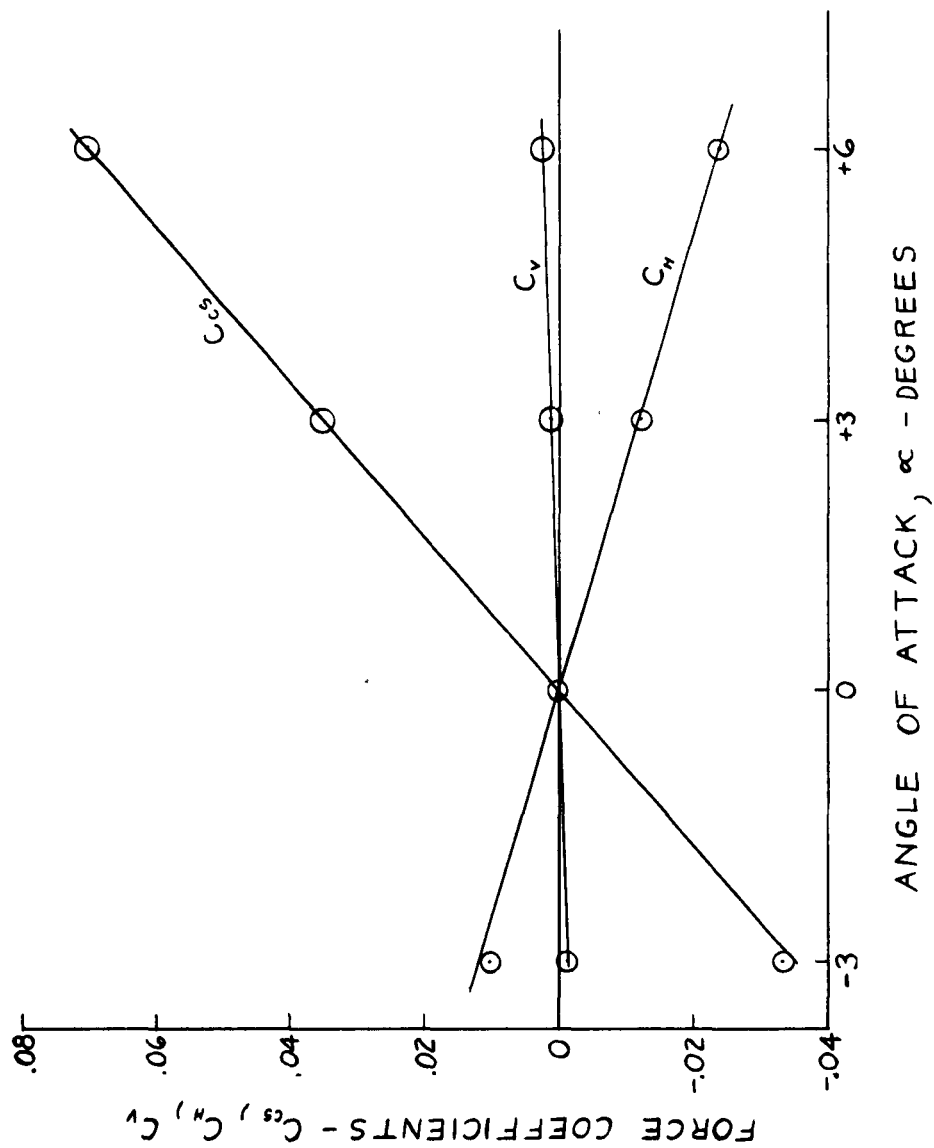


Fig. 25 Measured Force Coefficients for $d/R_p = 0.267$,
 $B = 10$, $J = 2.0$

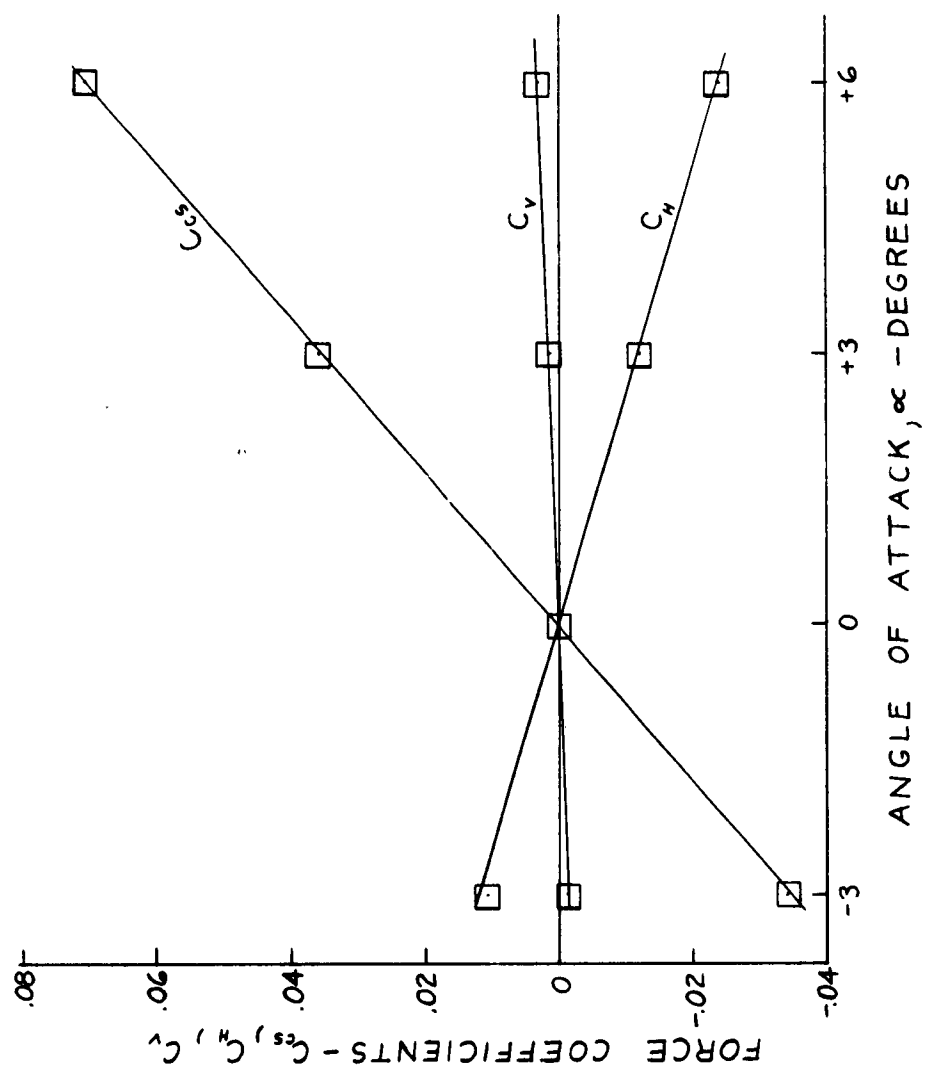


Fig. 26 Measured Force Coefficients for $d/R_p = 0.667$, $B = 10$, $J = 2.0$

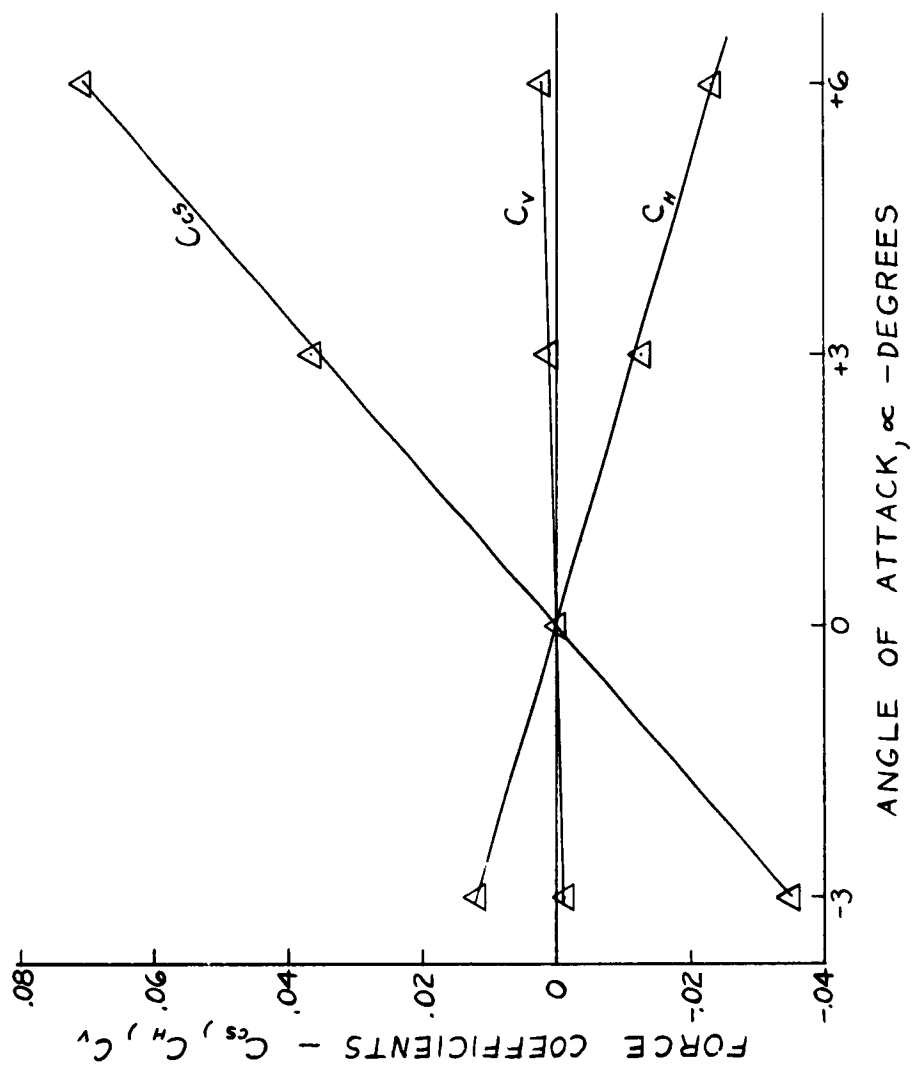


Fig. 27 Measured Force Coefficients for $d/R_p = 1.067$,
 $B = 10$, $J = 2.0$

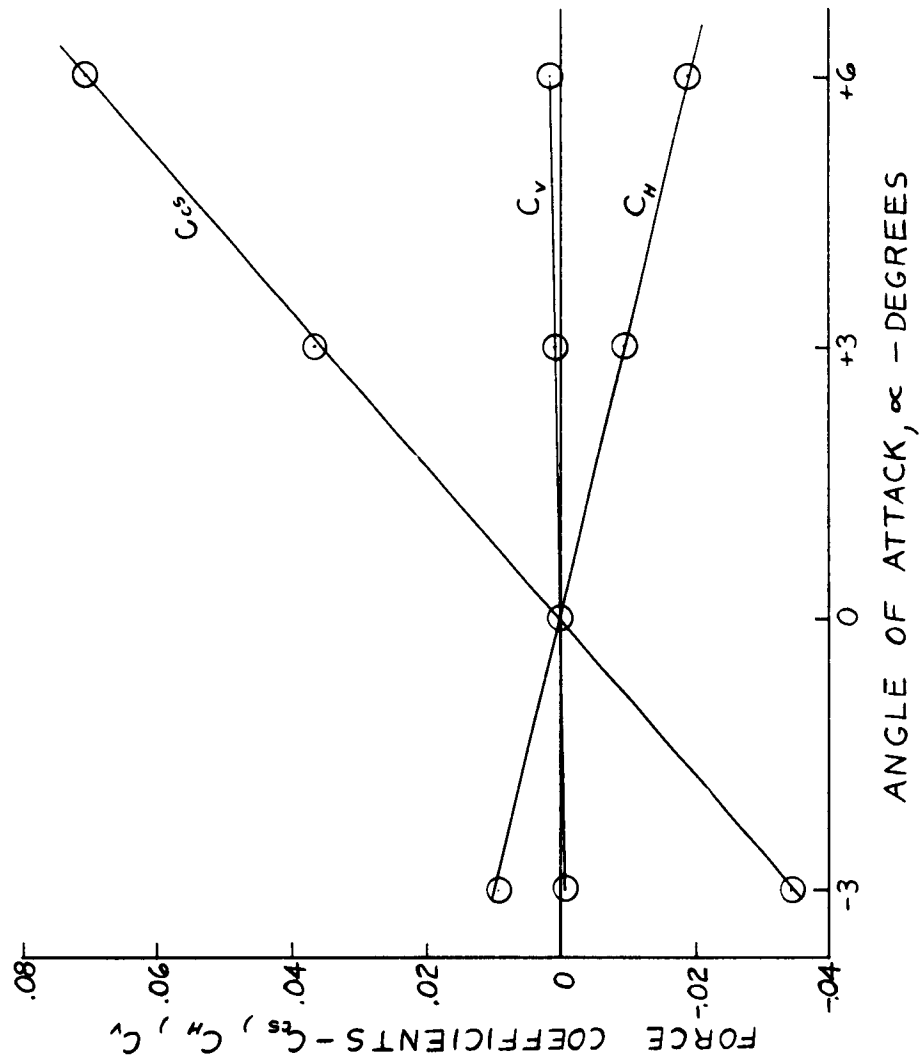


Fig. 28 Measured Force Coefficients for $d/R_p = 0.267$,
 $B = 5$, $J = 2.0$

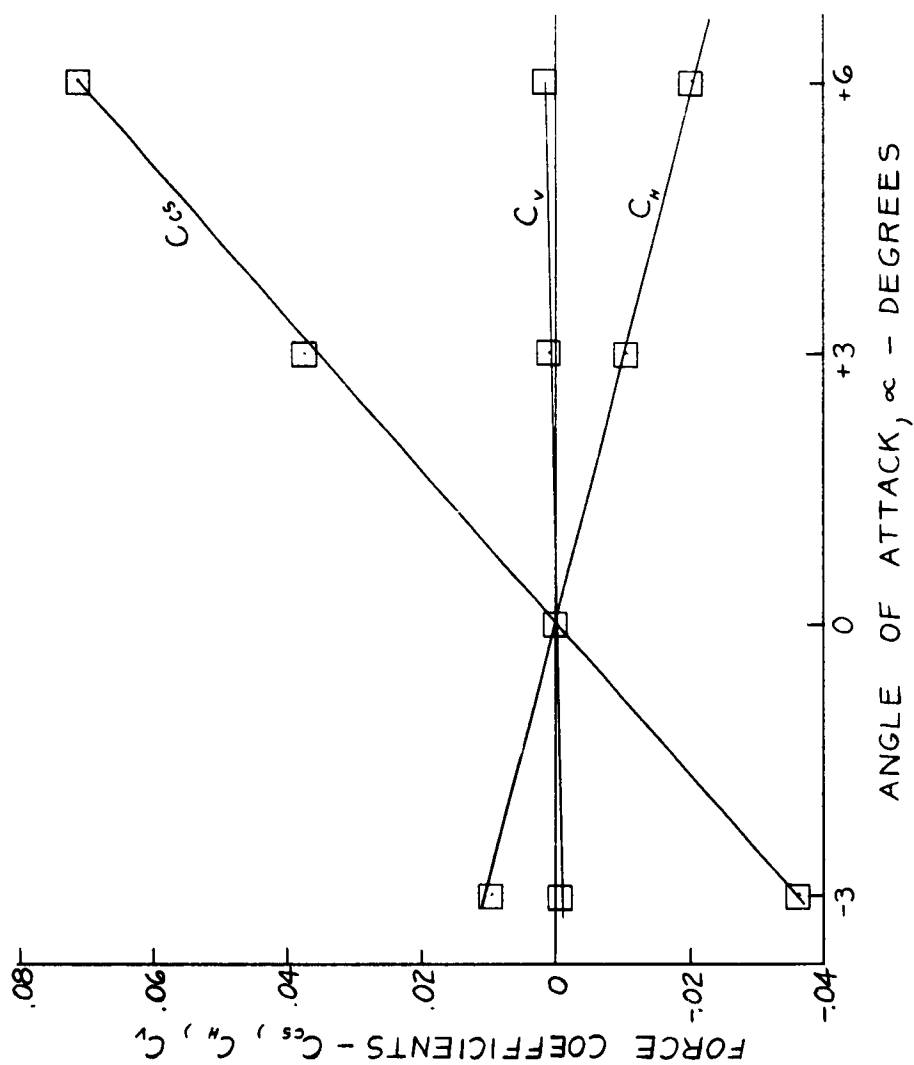


Fig. 29 Measured Force Coefficients for $d/R_p = 0.667$,
 $B = 5$, $J = 2.0$

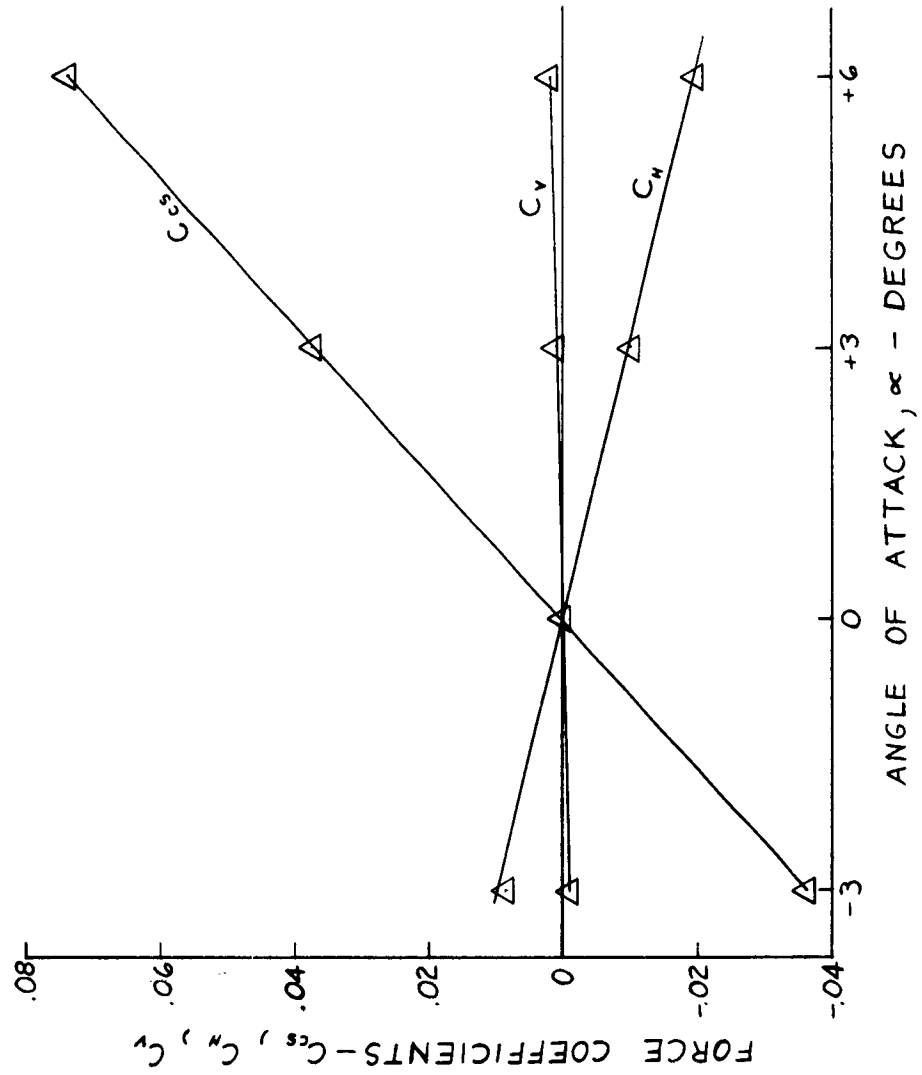


Fig. 30 Measured Force Coefficients for $d/R_p = 1.067$,
 $B = 5$, $J = 2.0$

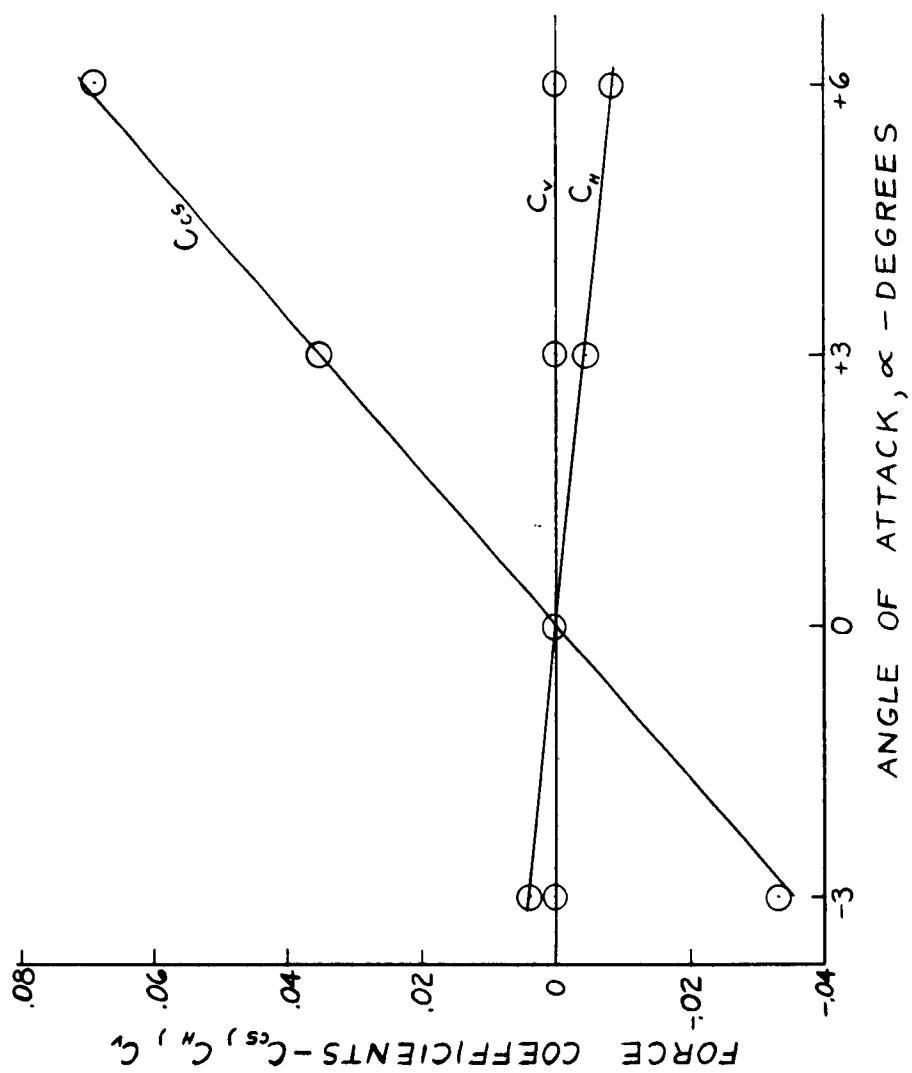


Fig. 31 Measured Force Coefficients for $d/R_p = 0.267$,
 $B = 2$, $J = 2.0$

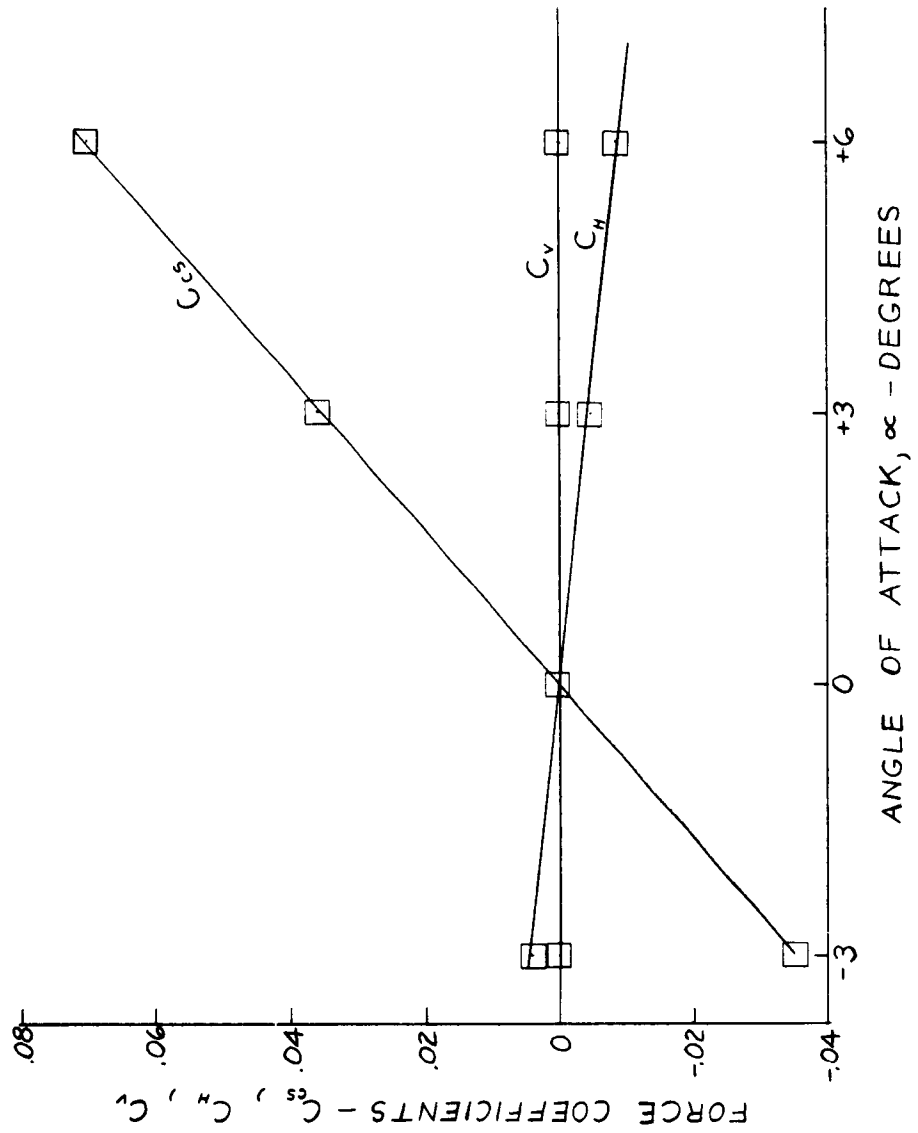


Fig. 32 Measured Force Coefficients for $d/R_p = 0.667$,
 $B = 2$, $J = 2.0$

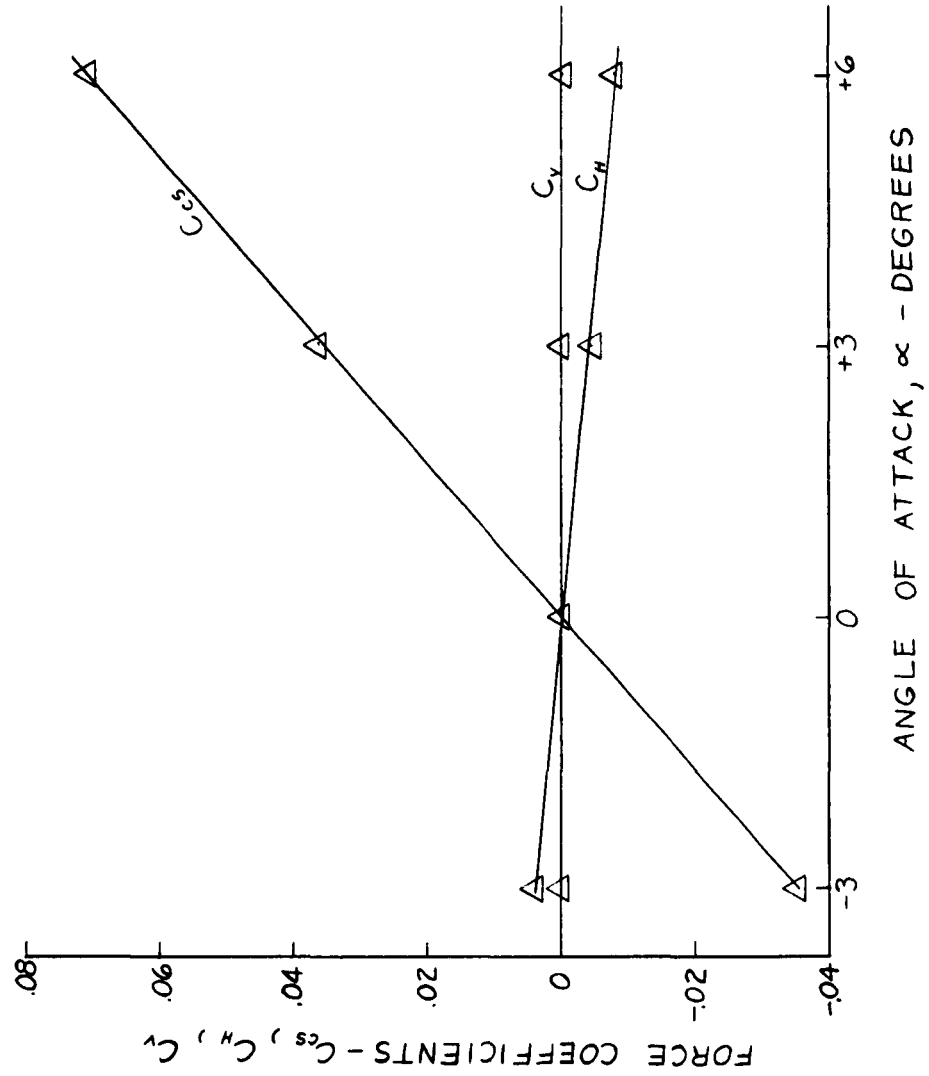


Fig. 33 Measured Force Coefficients for $d/R_p = 1.067$,
 $B = 2$, $J = 2.0$

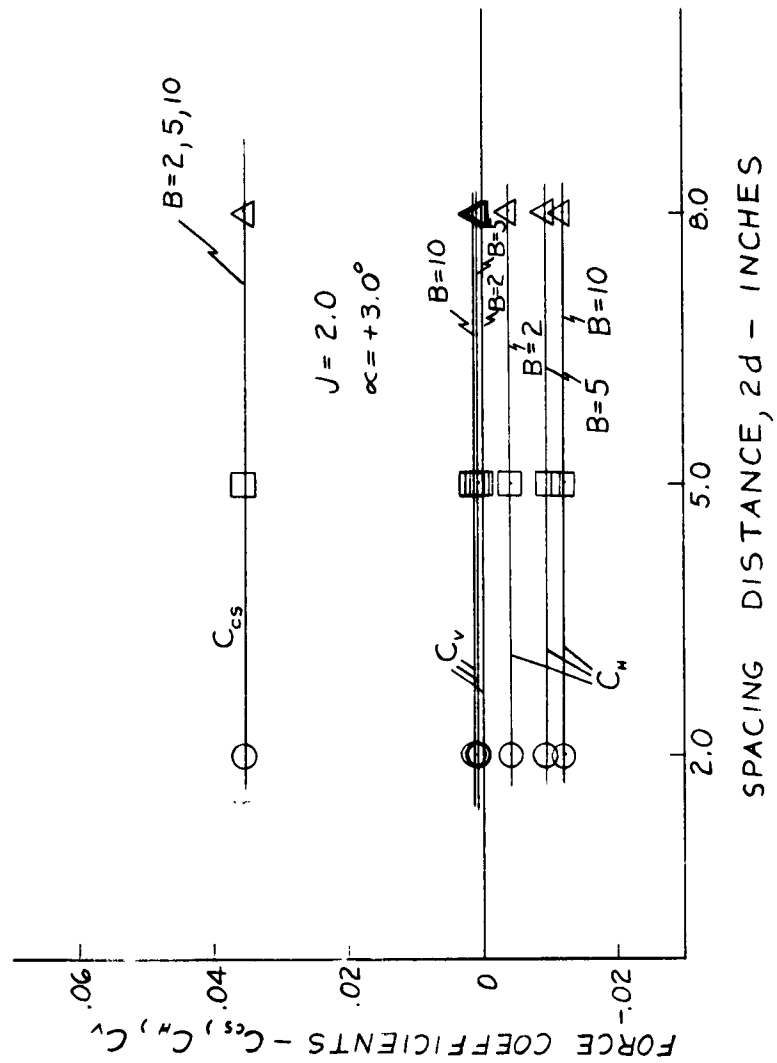


Fig. 34 Effect of Spacing Distance on Force Coefficients

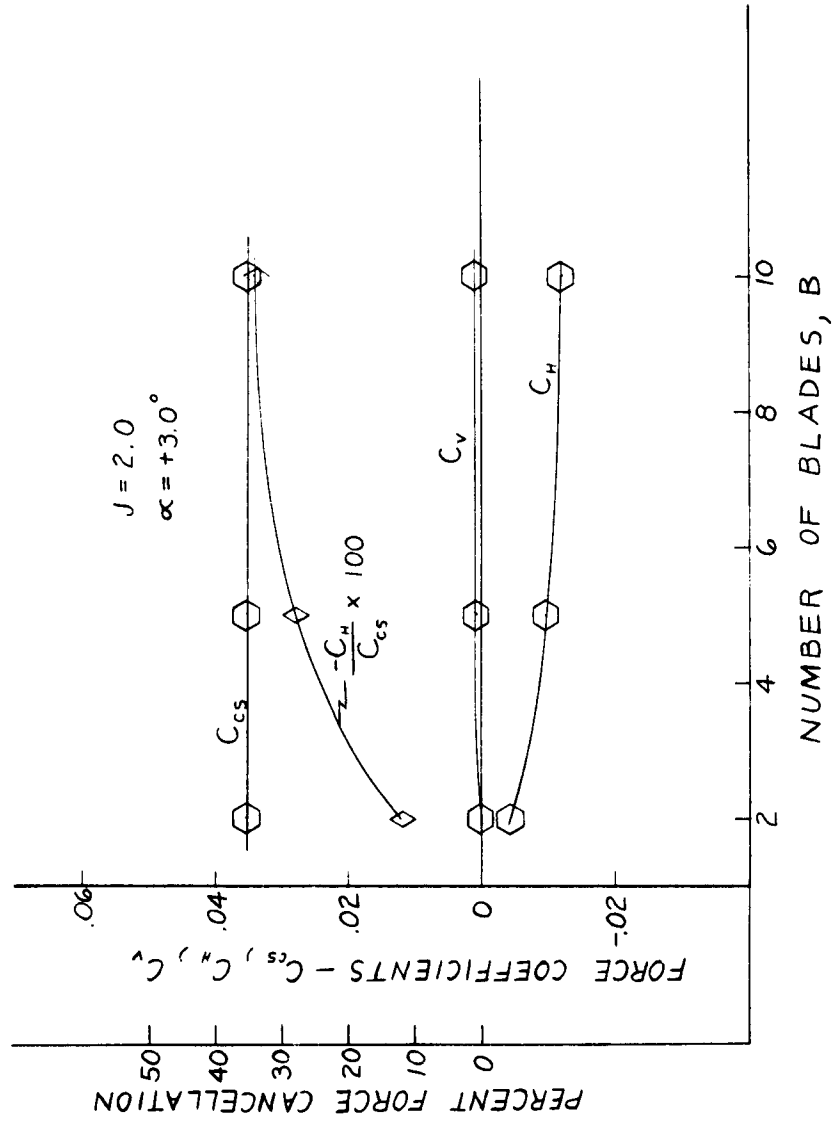


Fig. 35 Effect of Blade Number on Force Coefficients

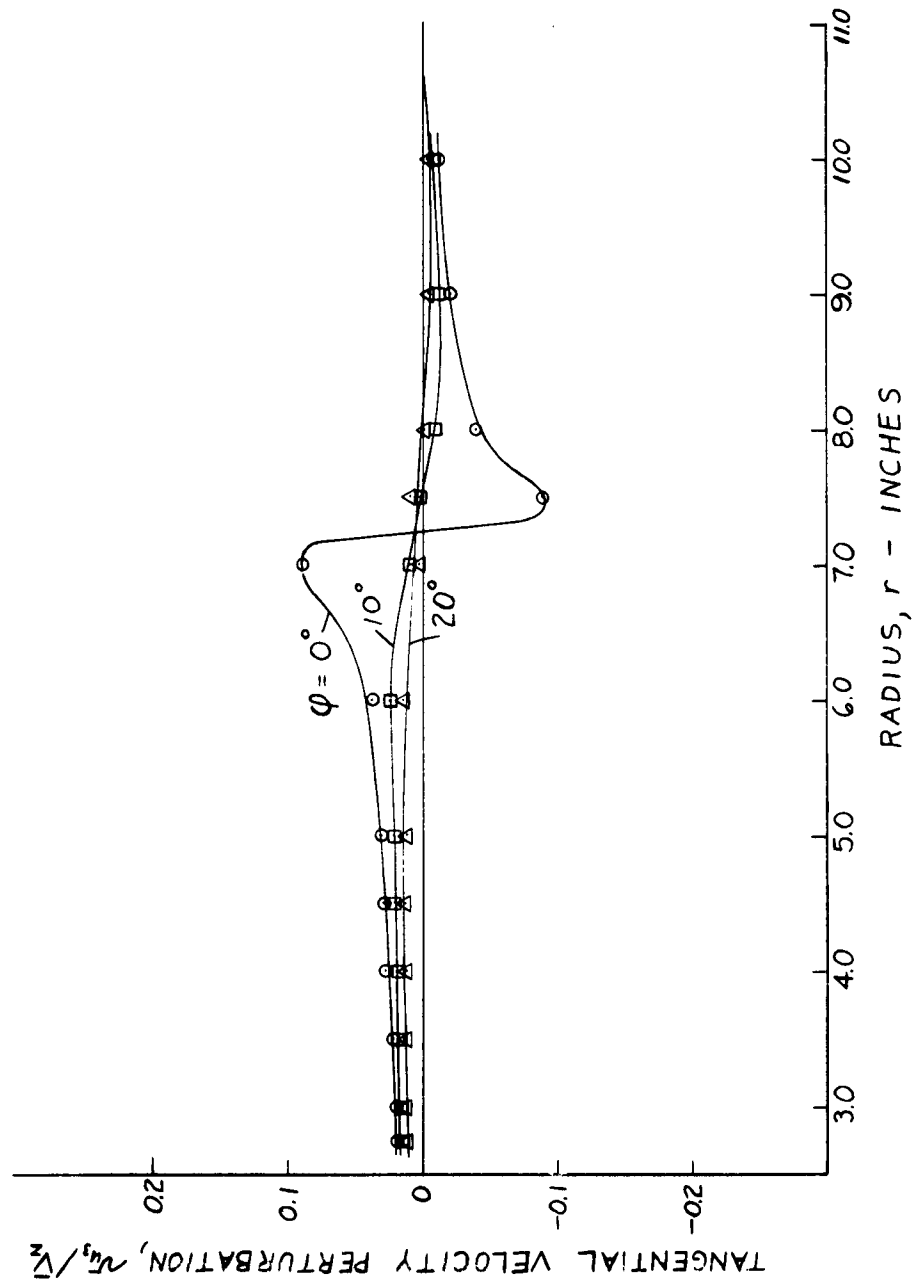


Fig. 36 Measured Distribution of v_{u3} at $z/R_p = 0.267$
 ($d/R_p = 0.267$, $B = 10$)

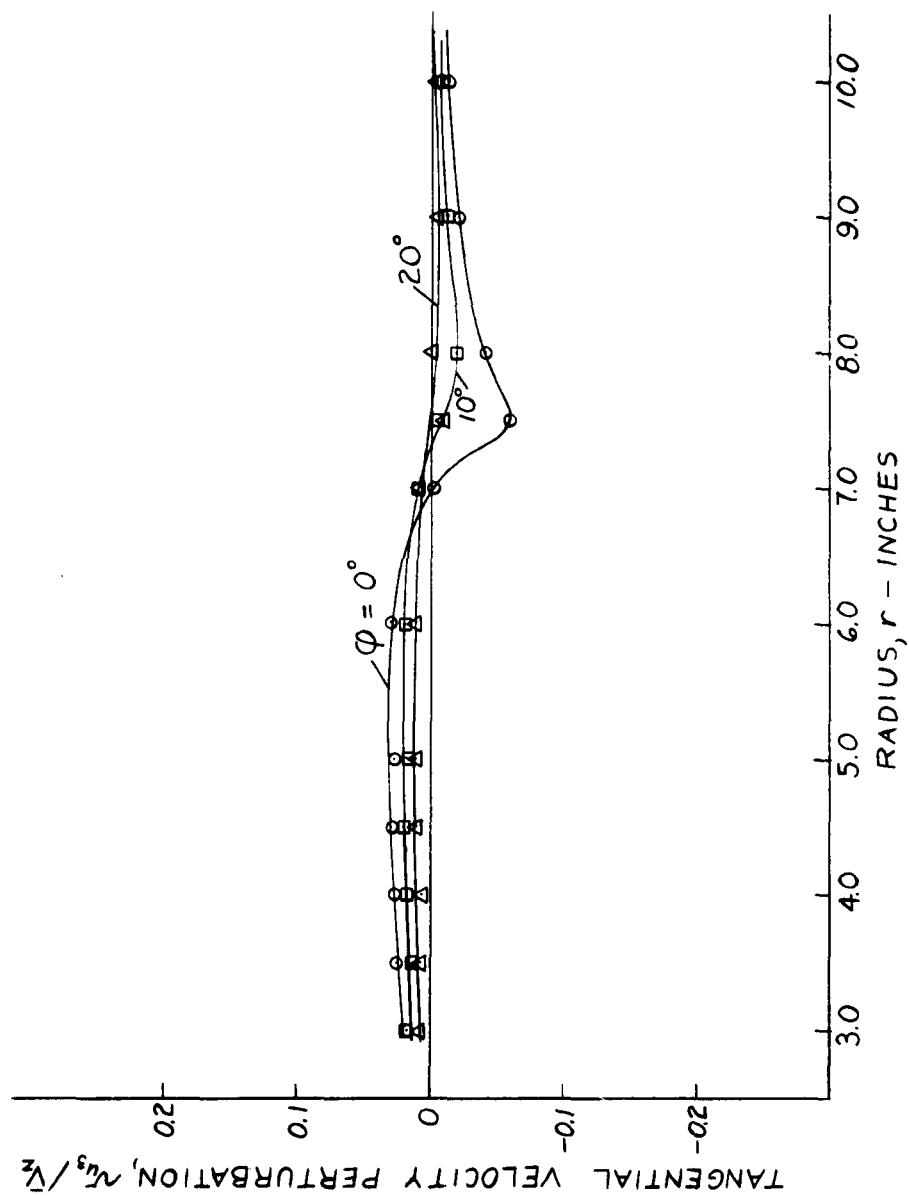


Fig. 37 Measured Distribution of u_3 at $z/R_p = 2.667$
 ($d/R_p = 0.267$, $B = 10$)

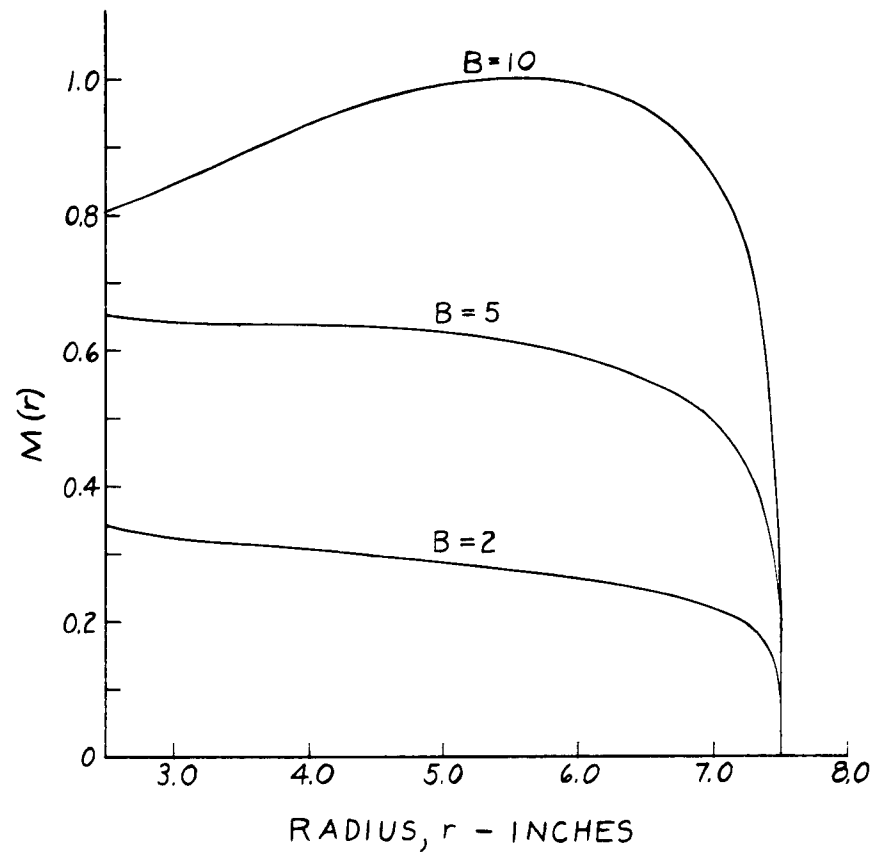


Fig. 38 Radial Distribution of $M(r)$

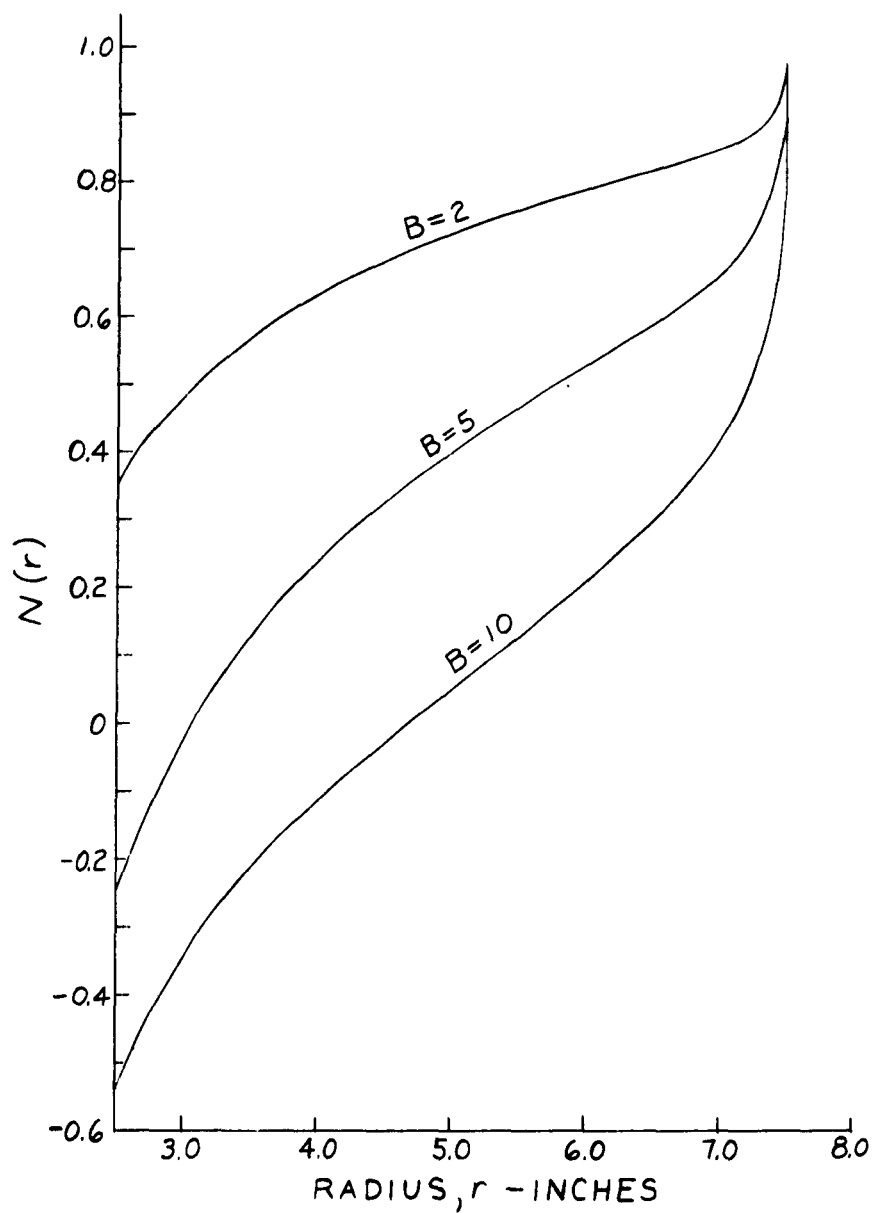


Fig. 39 Radial Distribution of $N(r)$

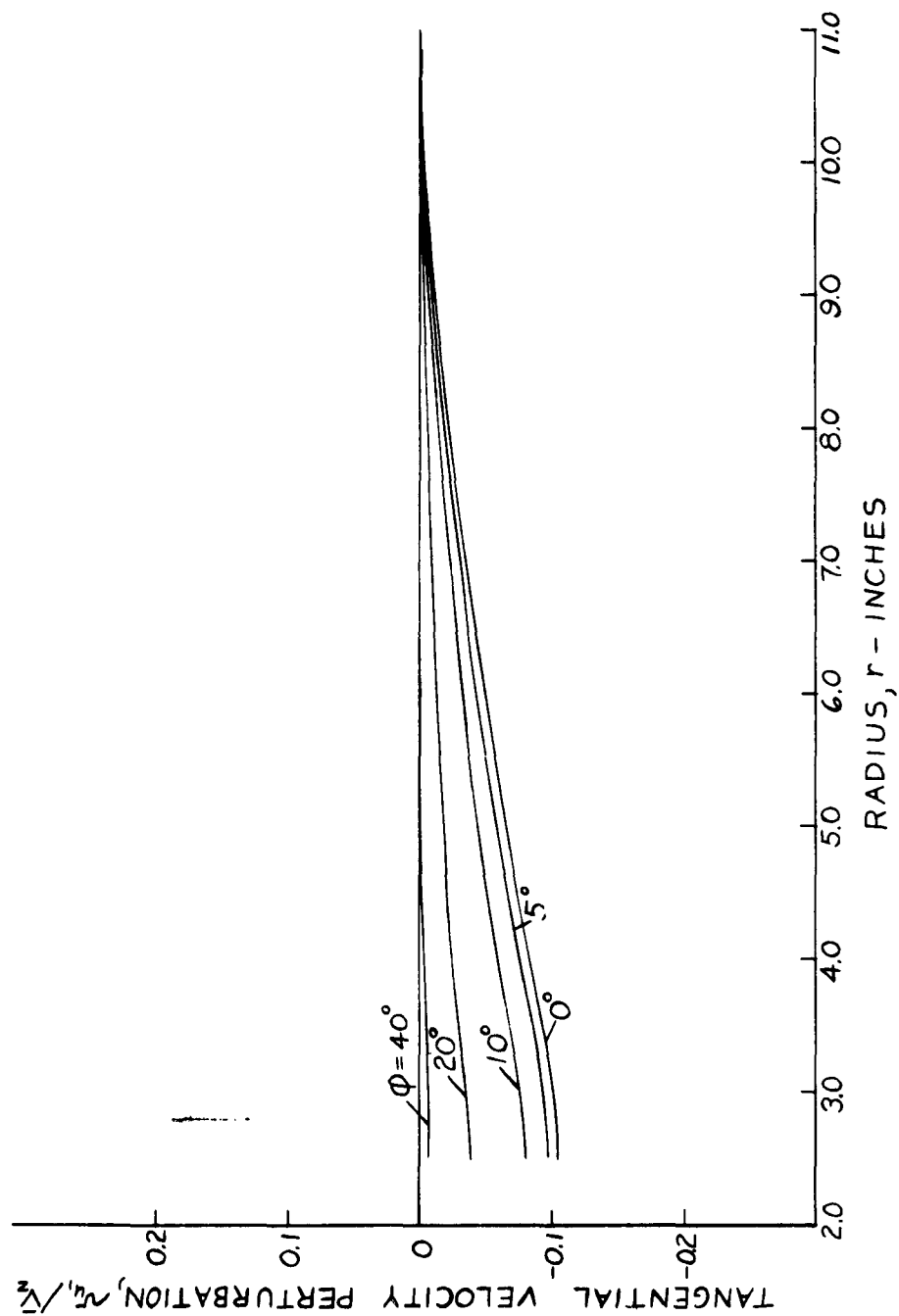


Fig. 40 Calculated Distribution of v_{u1} at $z = -d$
 ($d/R_p = 0.267$, $B = 10$)

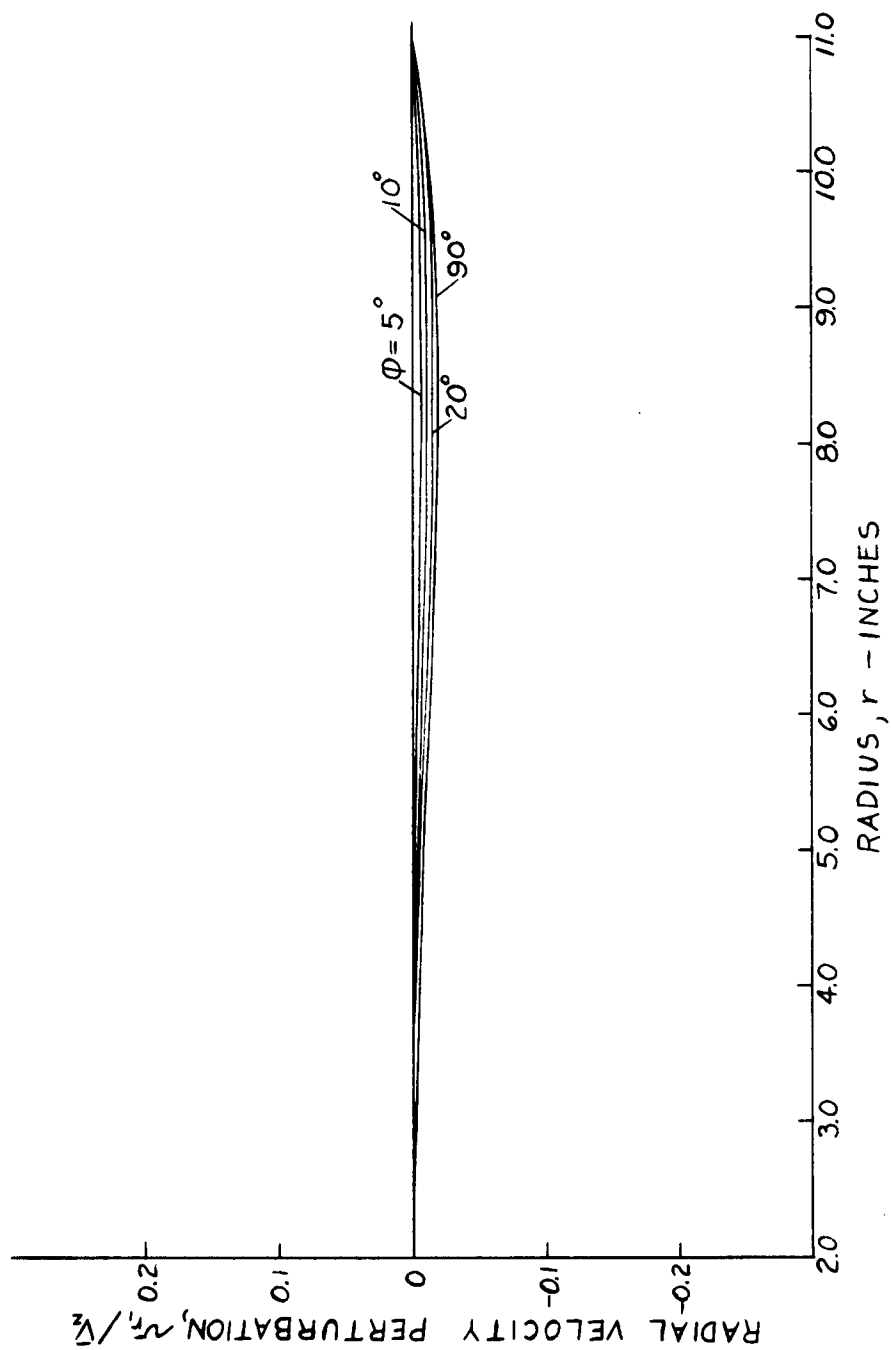


Fig. 41 Calculated Distribution of v_{r1} at $z = -d$
 ($d/R_p = 0.267$, $B = 10$)

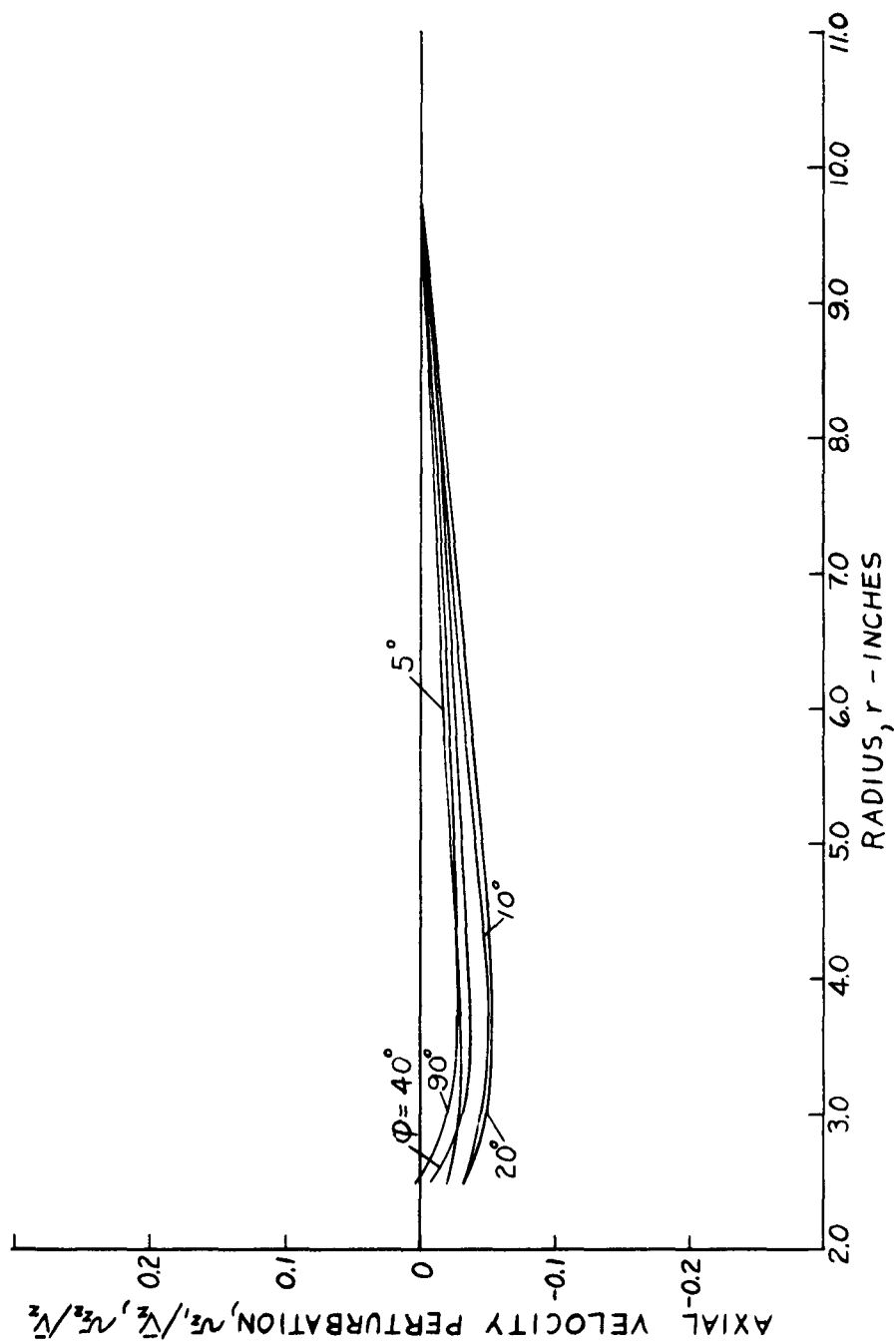


Fig. 42 Calculated Distribution of v_z and v_{z2} at $z = -d$ ($d/R_p = 0.267$, $B = 10^3$)

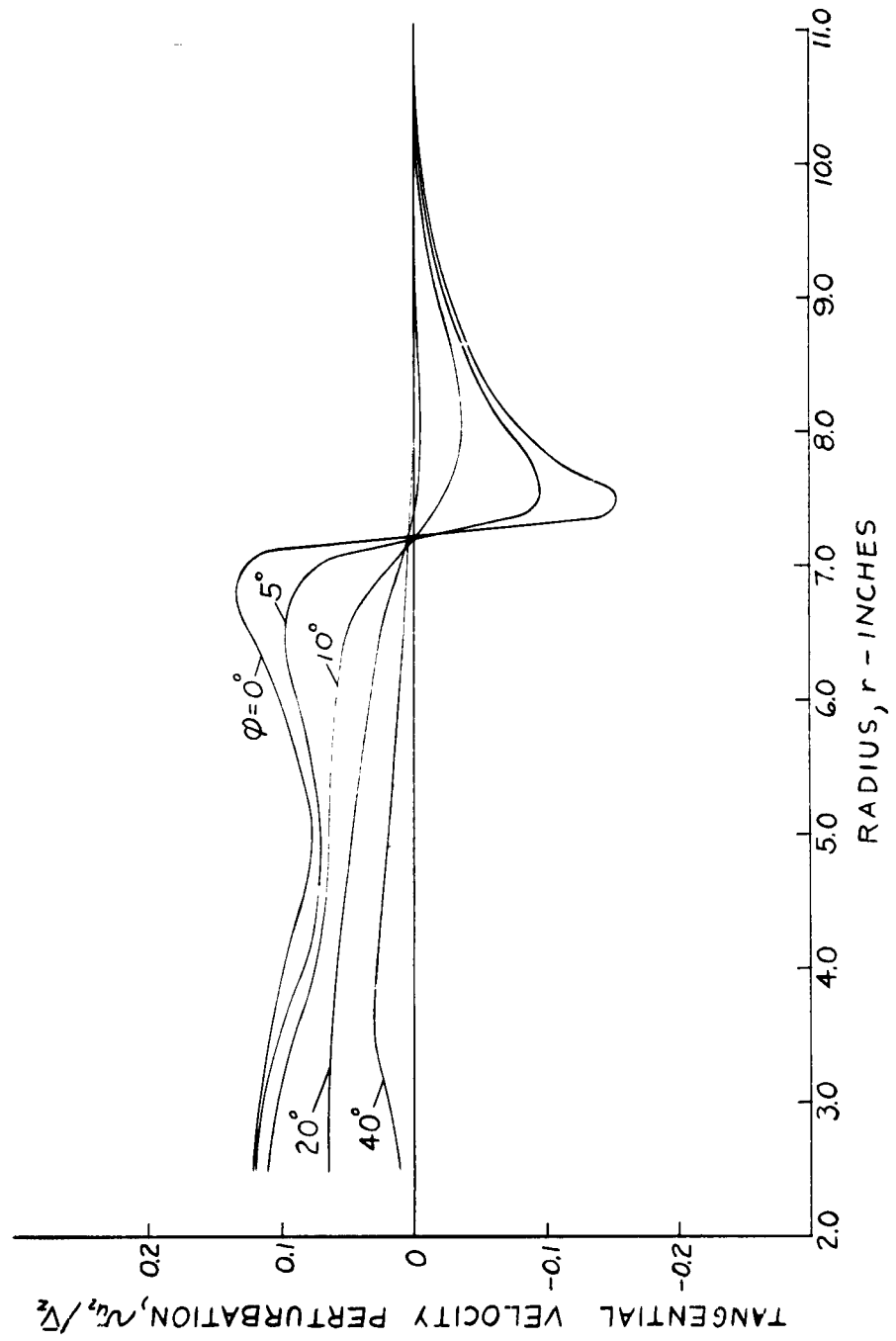


Fig. 43 Calculated Distribution of v_{u2} at $z = -d$
($d/R_p = 0.267$, $B = 10$)

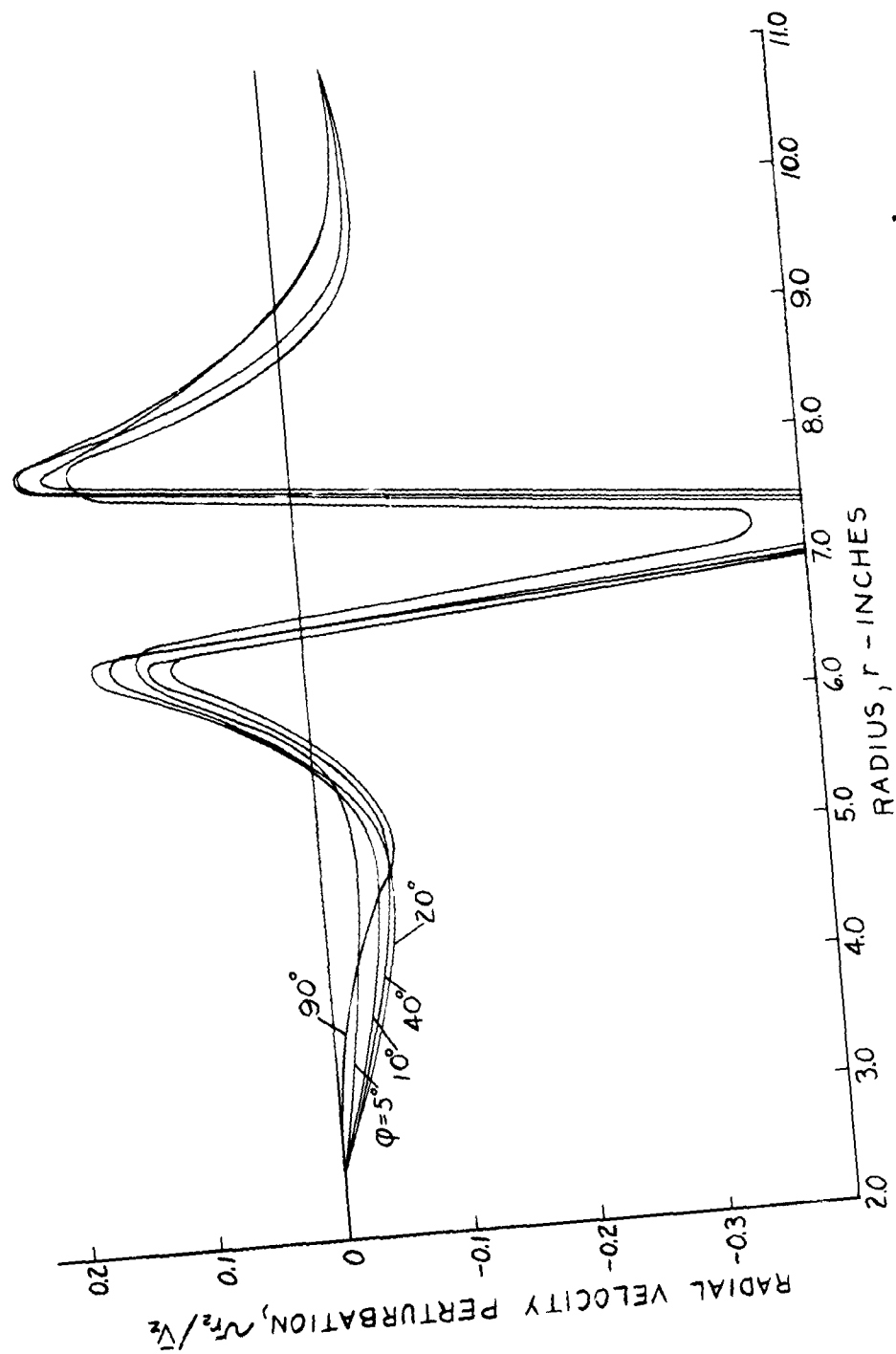


Fig. 44 Calculated Distribution of v_{r2} at $z = -d$
 ($d/R_p = 0.267$, $B = 10$)

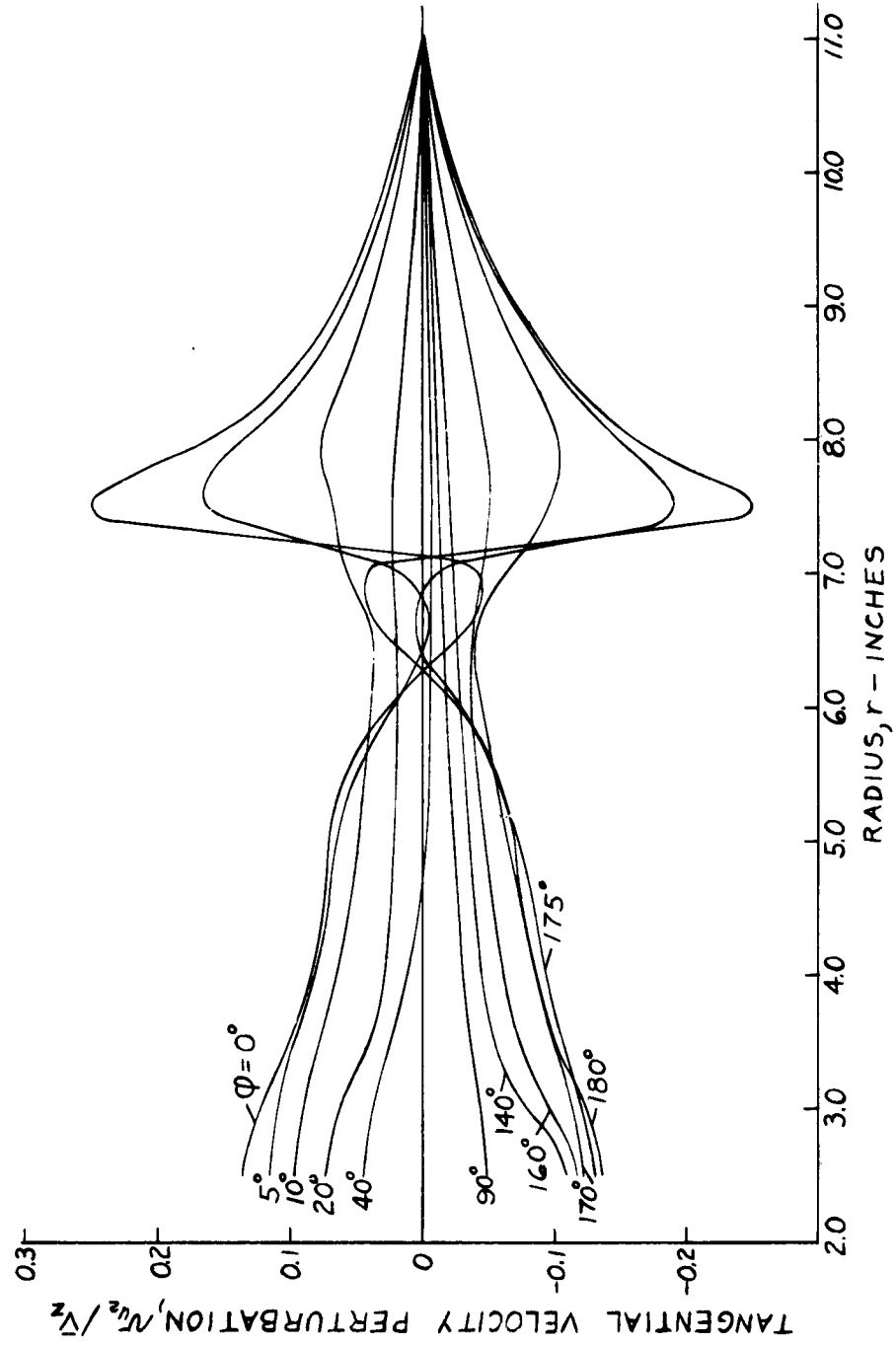


Fig. 45 Calculated Distribution of v_{u2} at $z = d$
($d/R_p = 0.267$, $B = 10$)

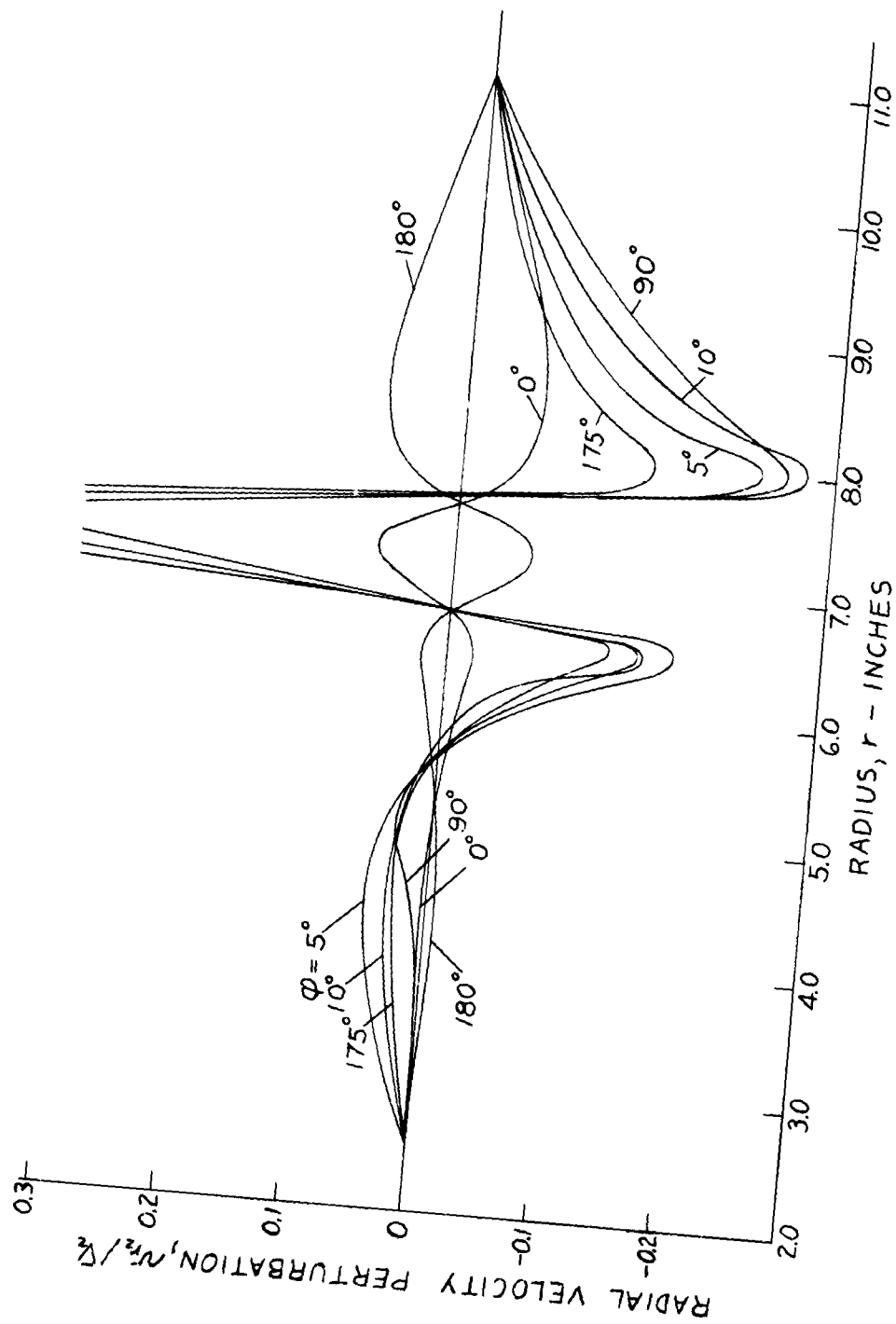


Fig. 46 Calculated Distribution of v_{r2} at $z = d$
 ($d/R_p = 0.267$, $B = 10$)

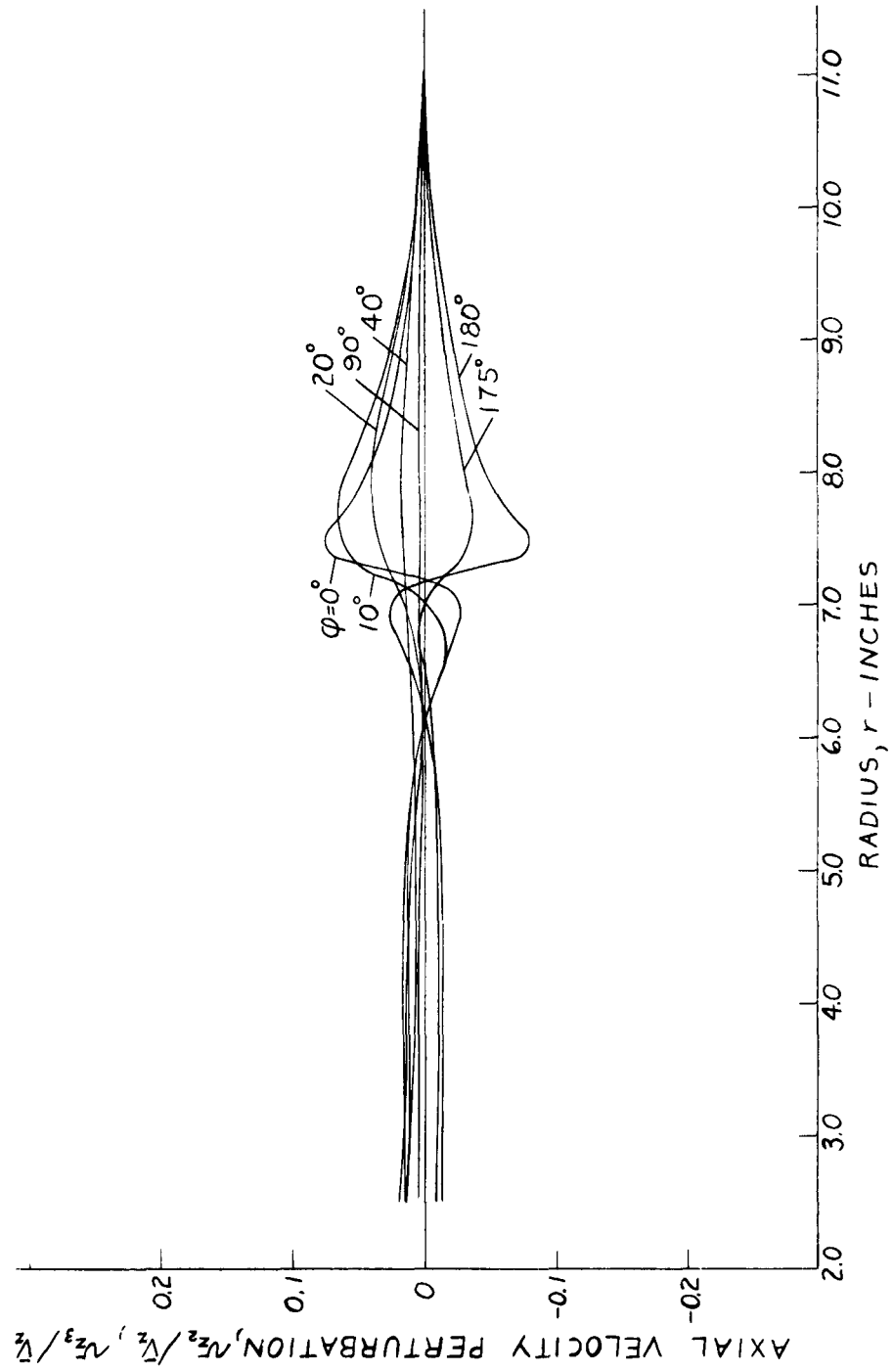


Fig. 47 Calculated Distribution of v_{z2} and v_{z3} at $z = d$ ($d/R_p = 0.267$, $B = 10$)

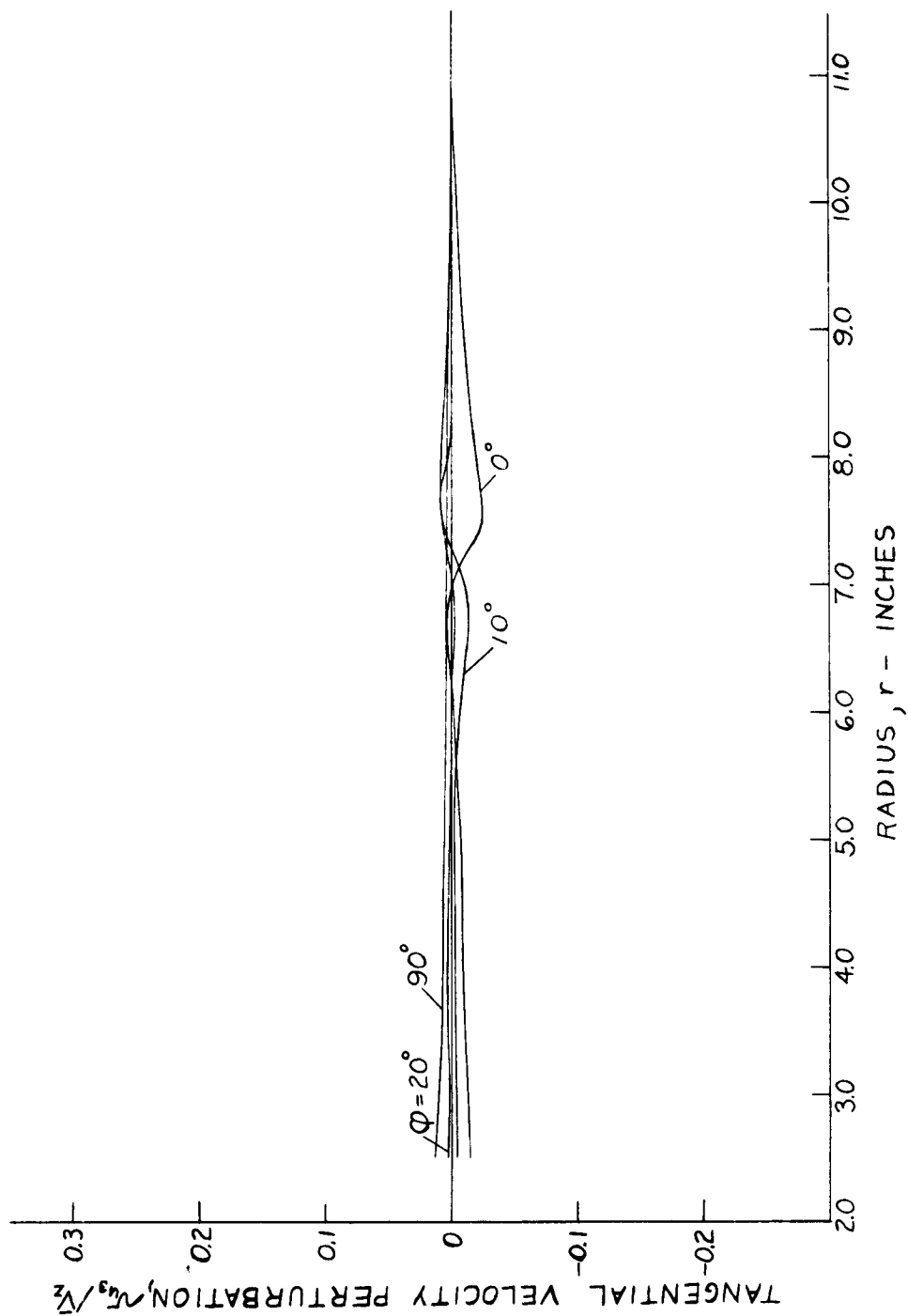


Fig. 48 Calculated Distribution of v_{u3} at $z = d$
($d/R_p = 0.267$, $B = 10$)

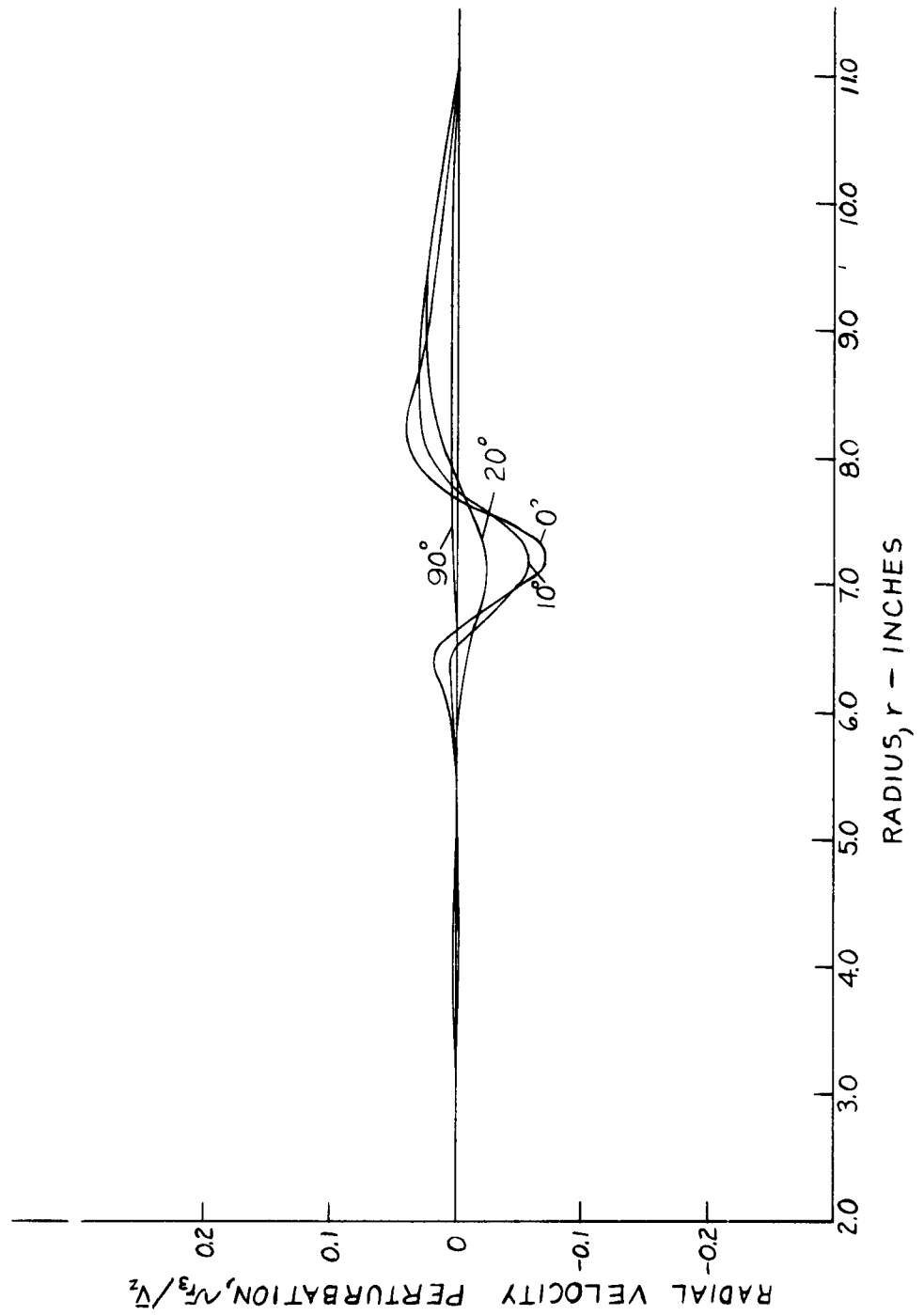


Fig. 49 Calculated Distribution of v_{r3} at $z = d$
($d/R_p = 0.267$, $B = 10$)

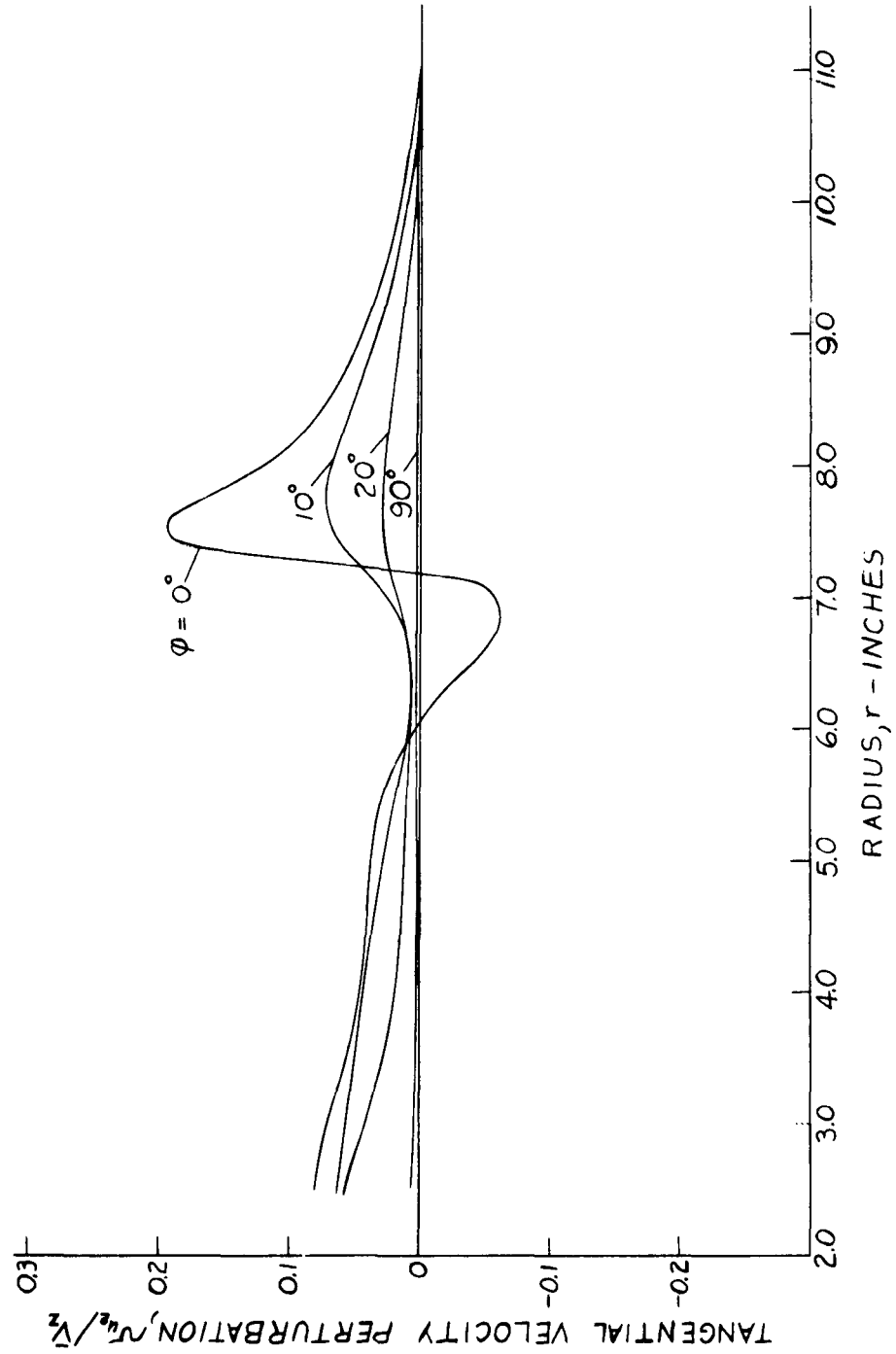


Fig. 50 Calculated Distribution of v_{u2} at $z = d$
 ($d/R_p = 0.267$, $B = 5$)

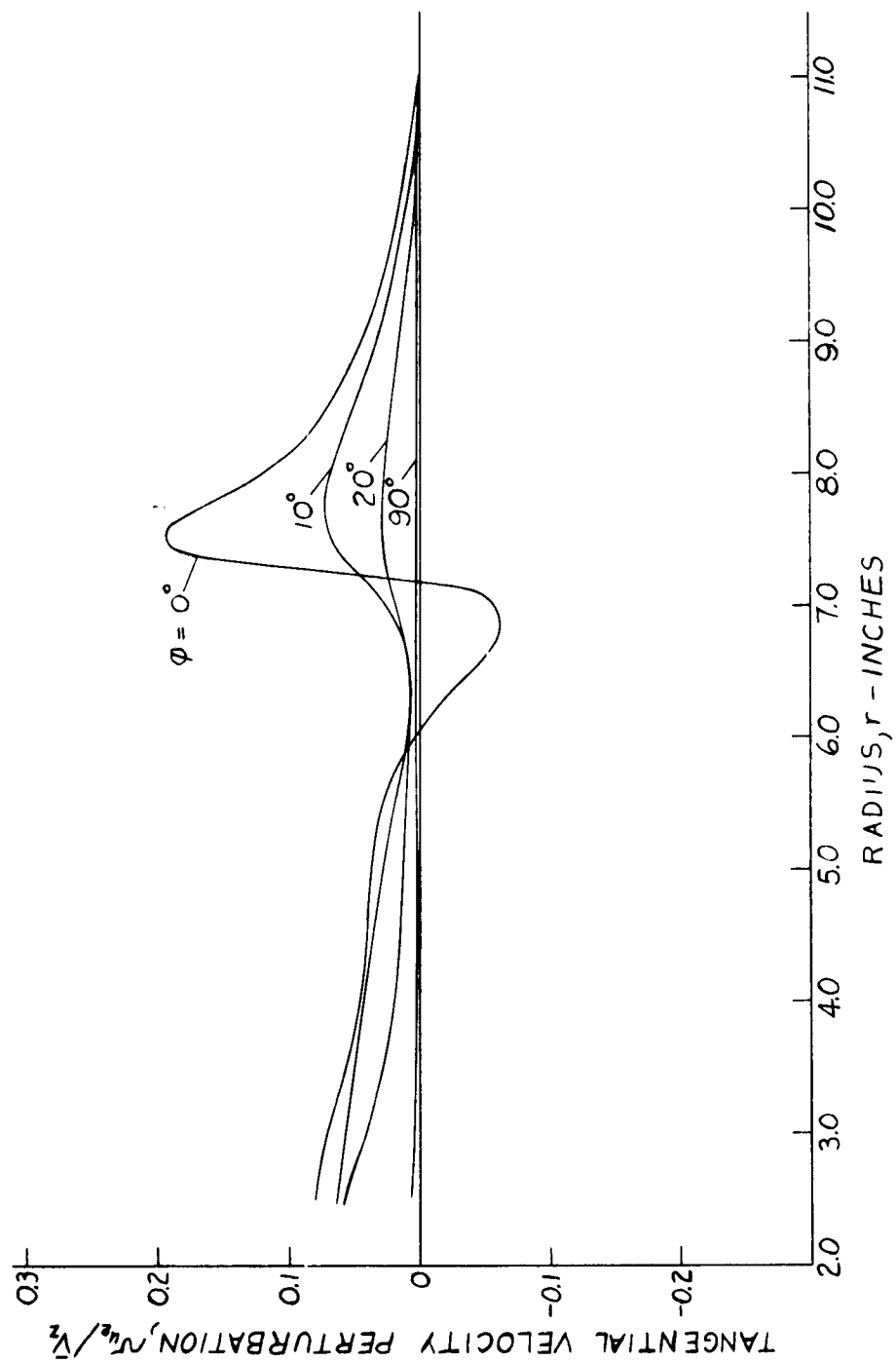


Fig. 50 Calculated Distribution of v_{u_2} at $z = d$
 ($d/R_p = 0.267$, $B = 5$)

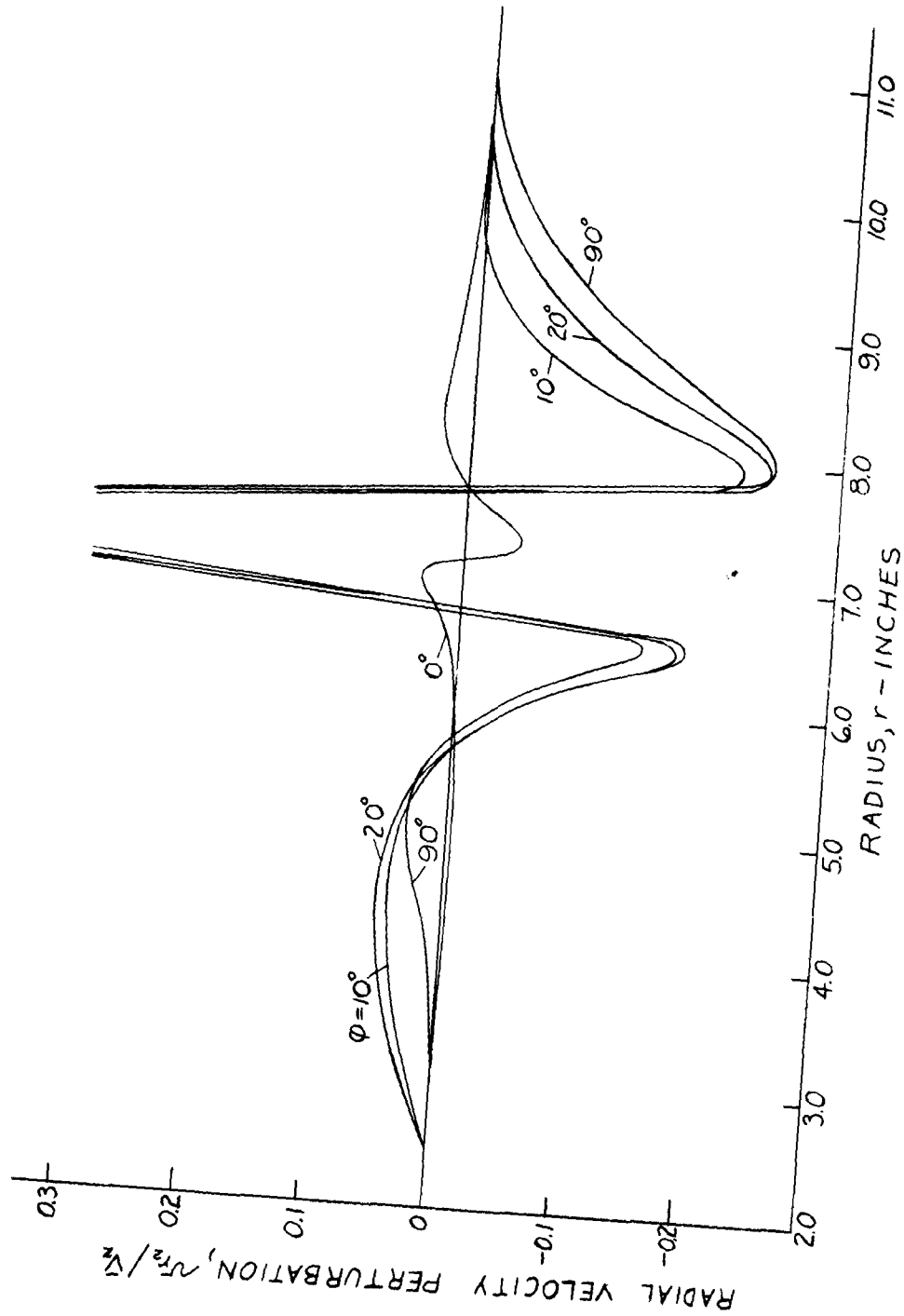


Fig. 51 Calculated Distribution of v_{r2} at $z = d$
($d/R_p = 0.267$, $B = 5$)

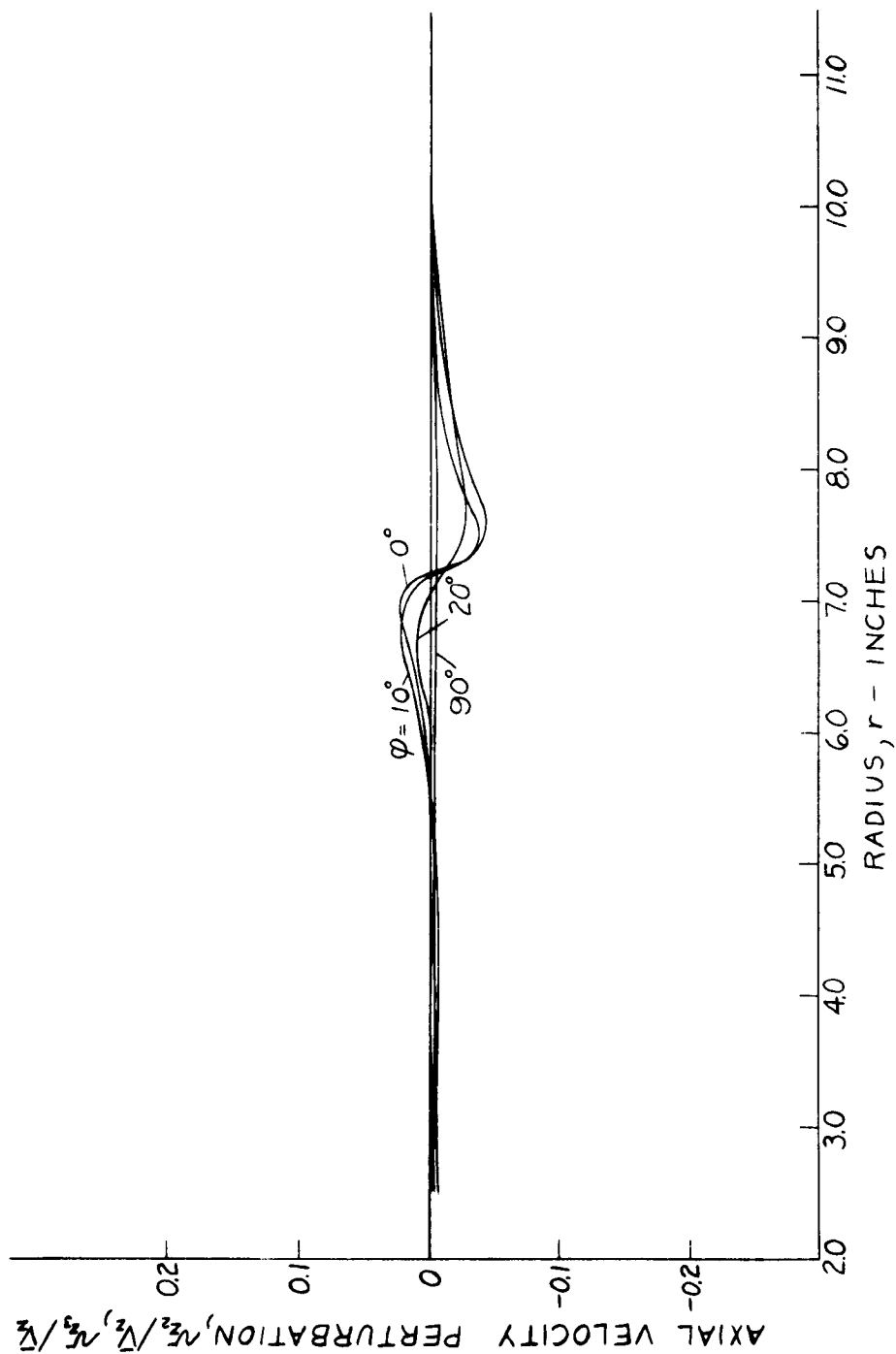


Fig. 52 Calculated Distribution of v_{z2} and v_{z3} at $z = d$ ($d/R_p = 0.267$, $B = 5$)

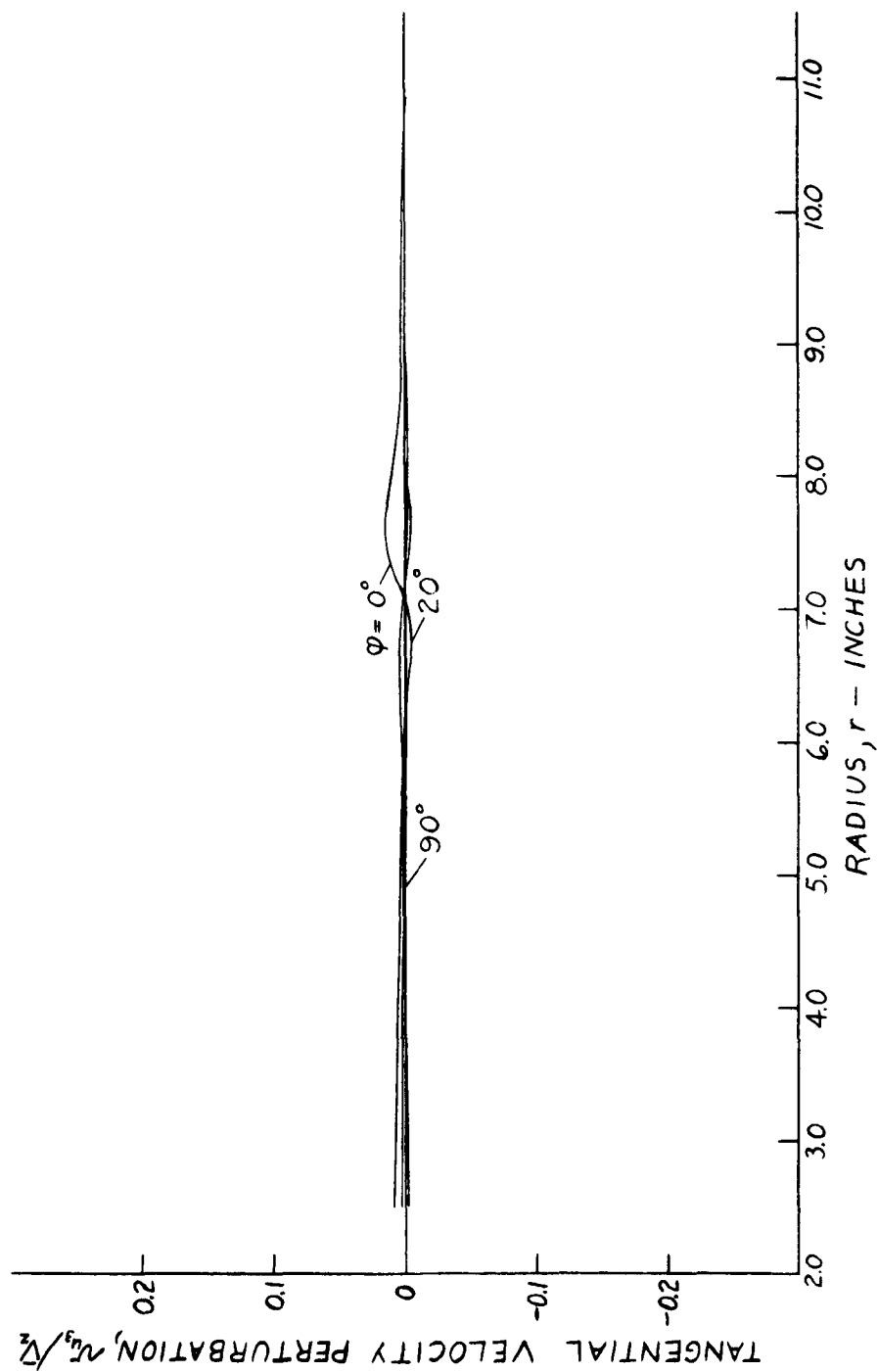


Fig. 53 Calculated Distribution of v_{u_3} at $z = d$
 ($d/R_p = 0.267$, $B = 5$)

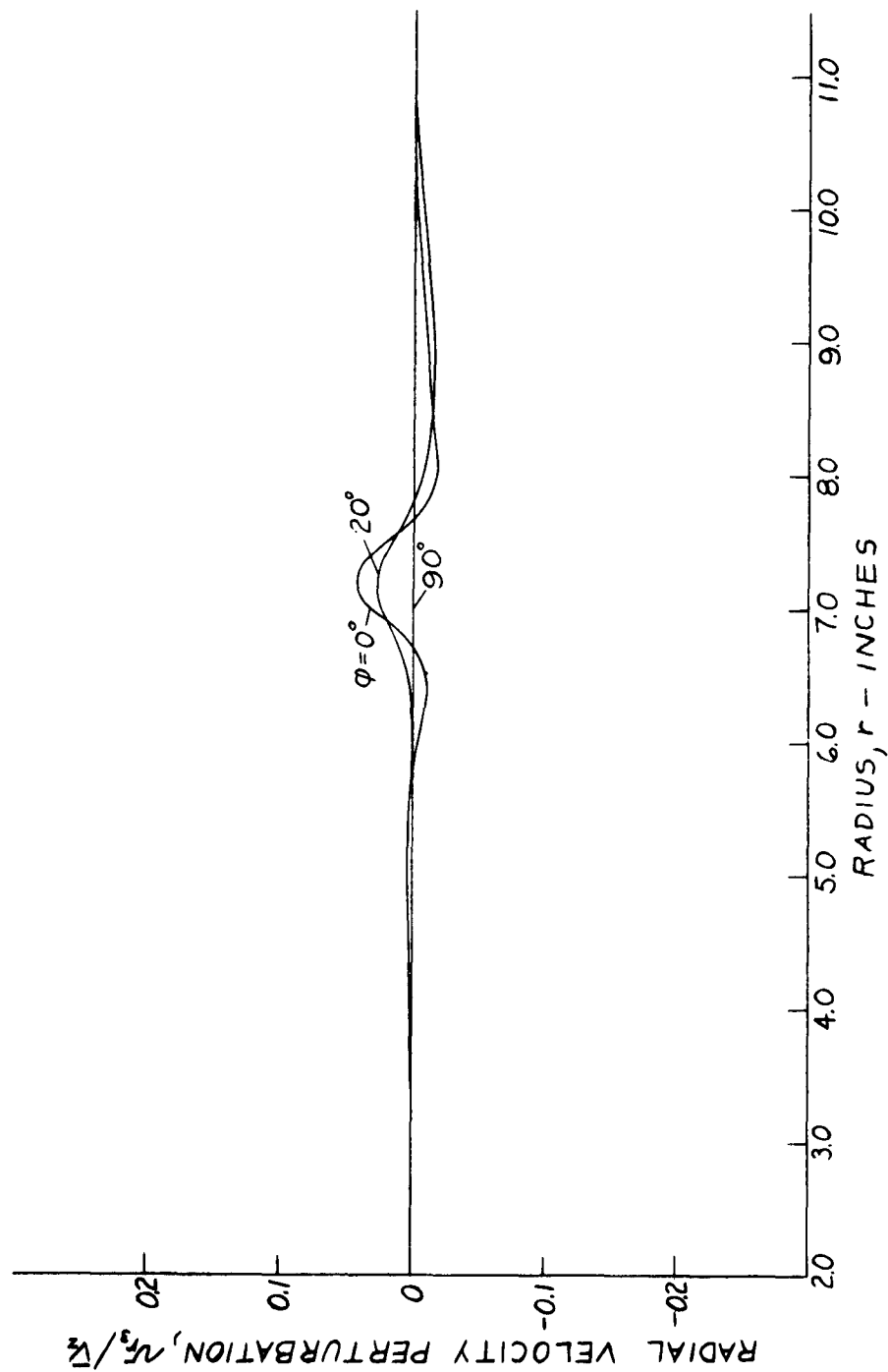


Fig. 54 Calculated Distribution of v_{r3} at $z = d$
 ($d/R_p = 0.267$, $B = 5$)

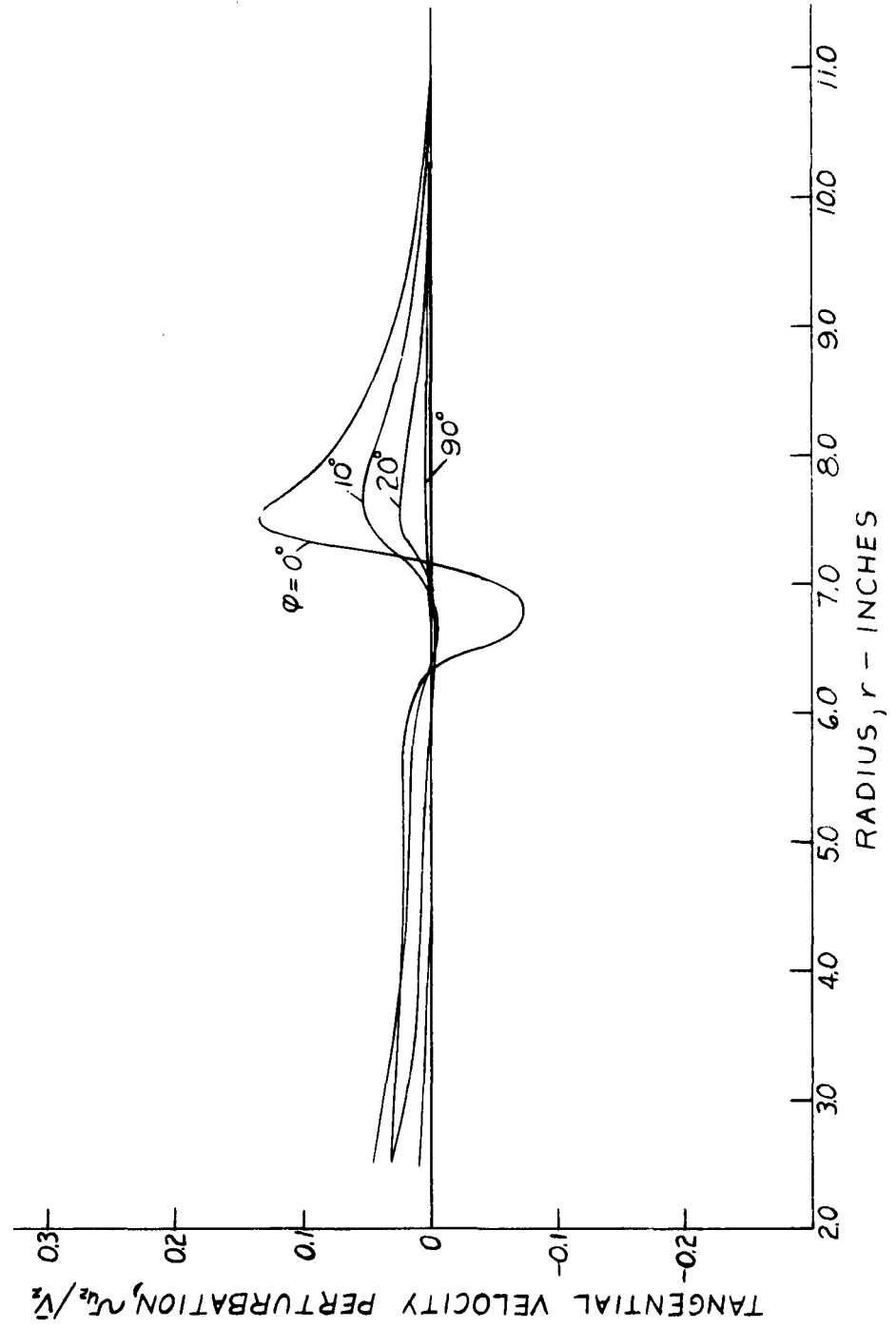


Fig. 55 Calculated Distribution of v_{u2} at $z = d$
 ($d/R_p = 0.267$, $B = 2$)

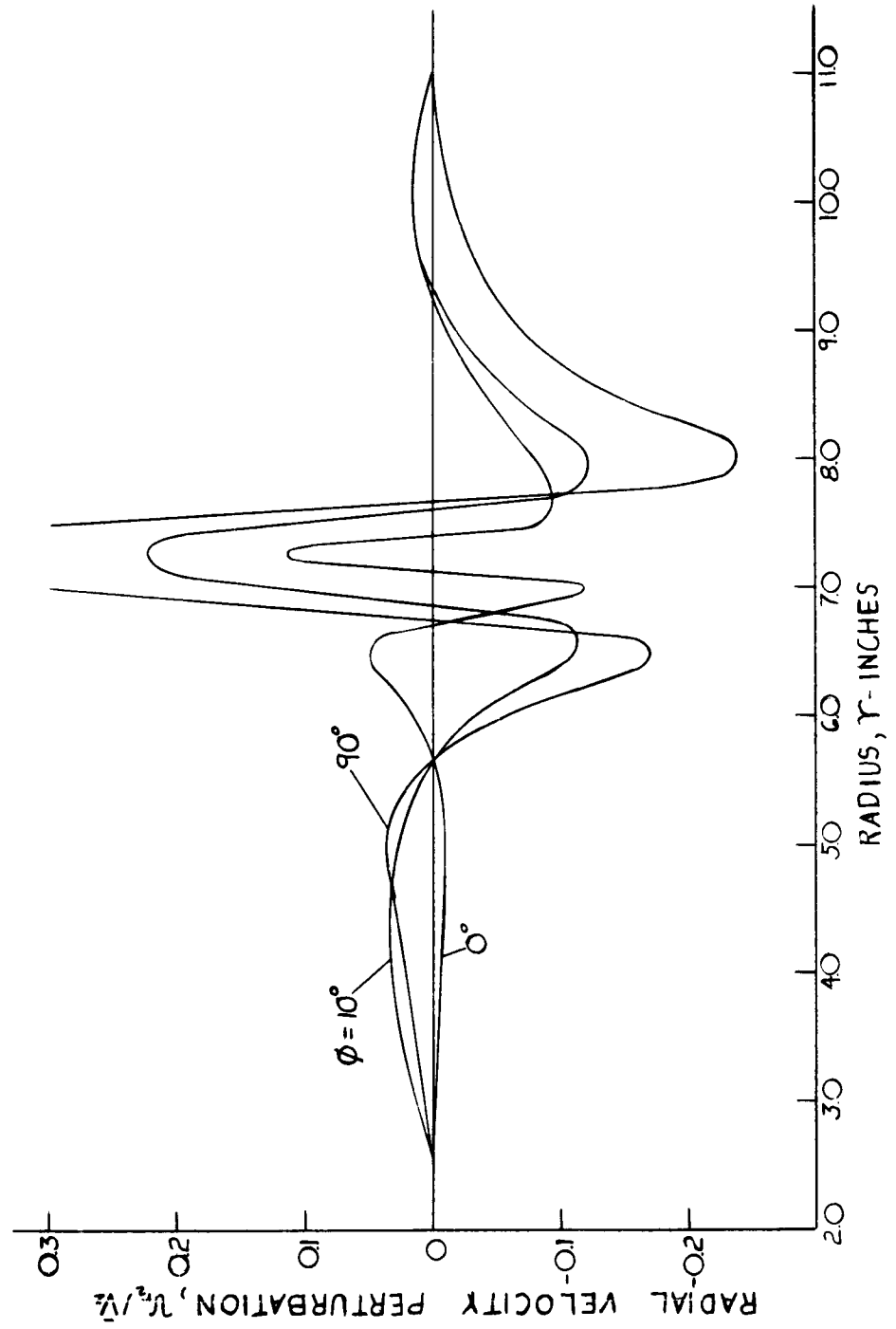


Fig. 56 Calculated Distribution of v_{r2} at $z = d$
 ($d/R_p = 0.267$, $B = 2$)

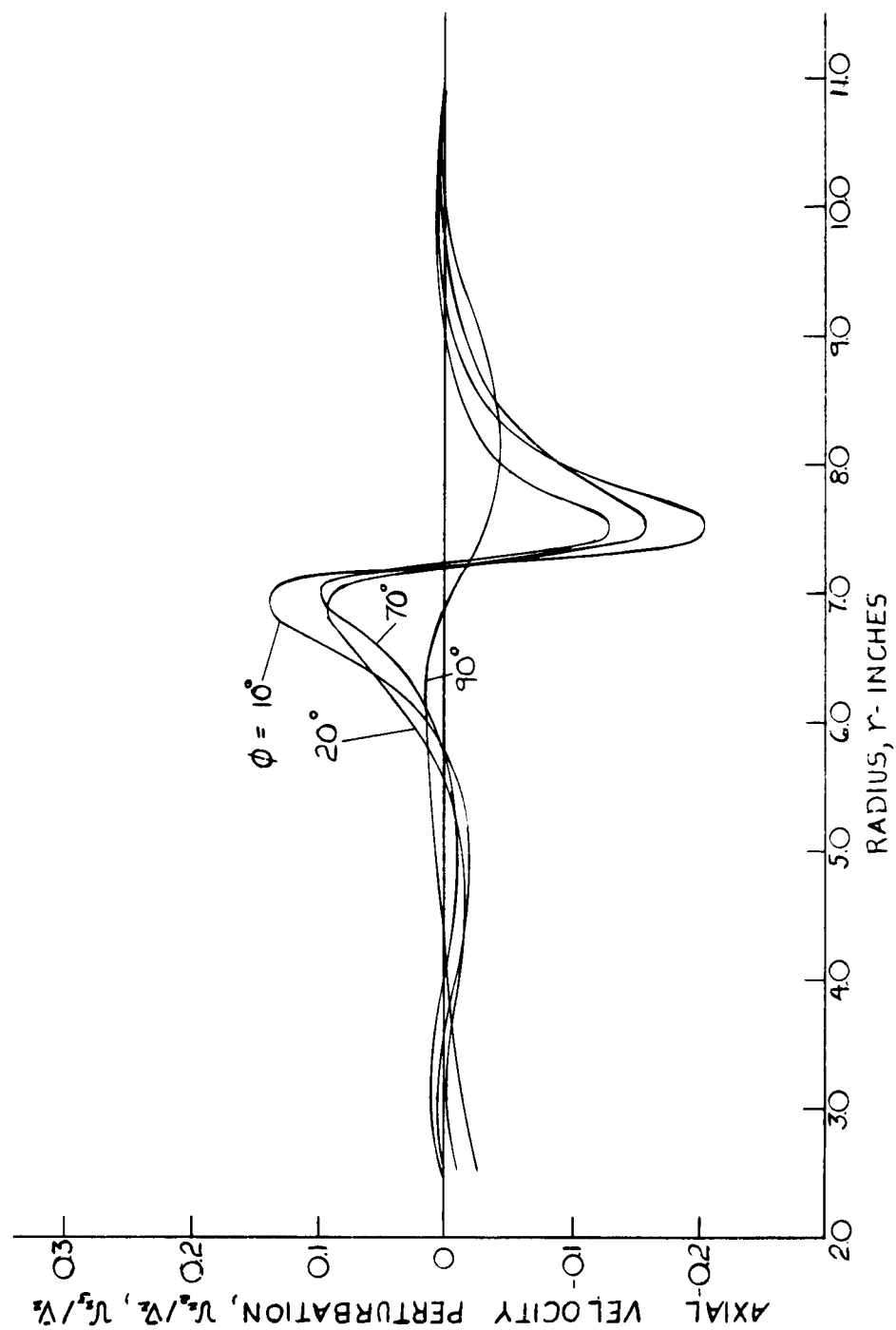


Fig. 57 Calculated Distribution of v_{z2} and v_{z3} at $z = d$
 $(d/R_p = 0.267, B = 2)$

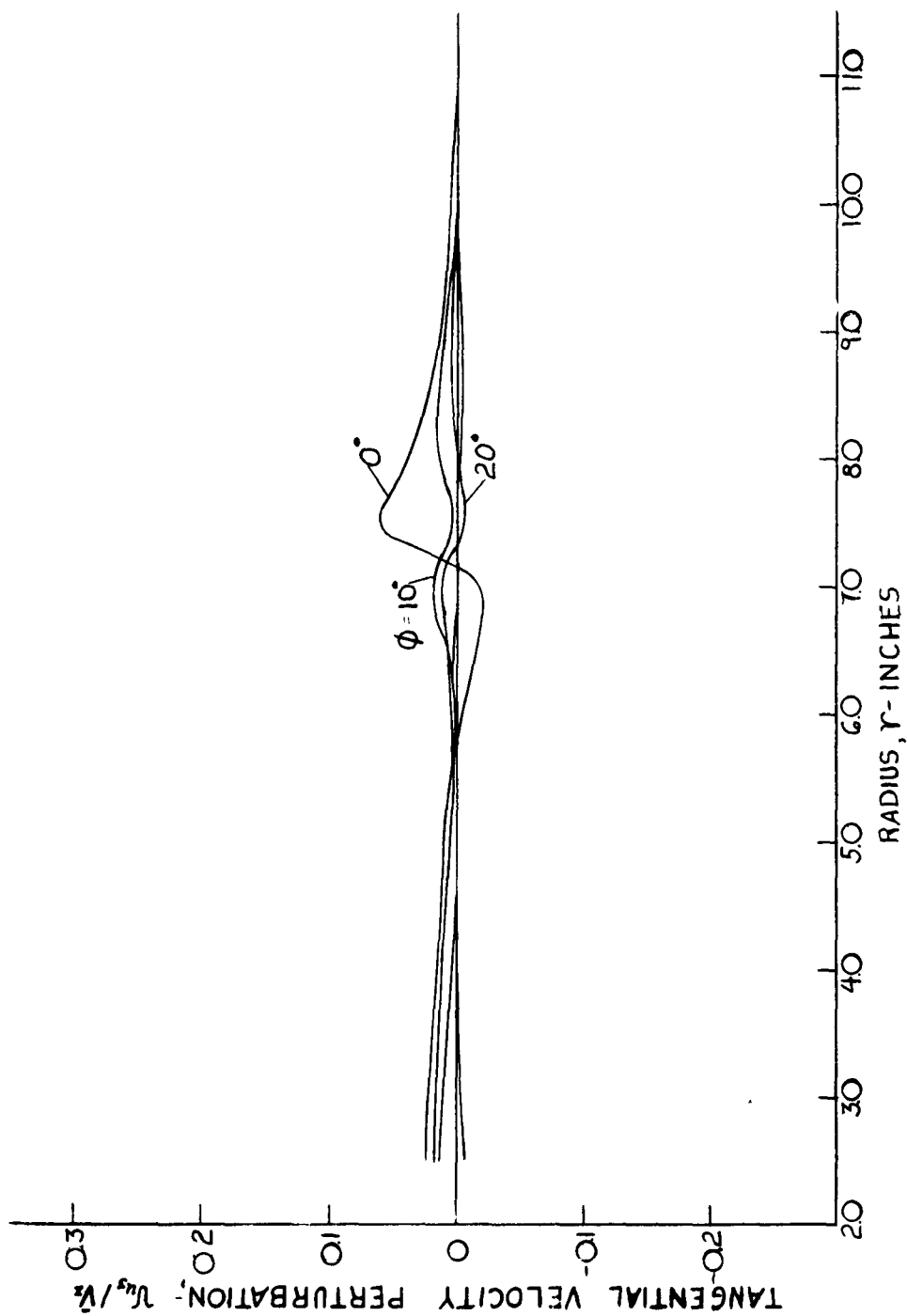


Fig. 58 Calculated Distribution of v_{u_3} at $z = d$
($d/R_p = 0.267$, $B = 2$)

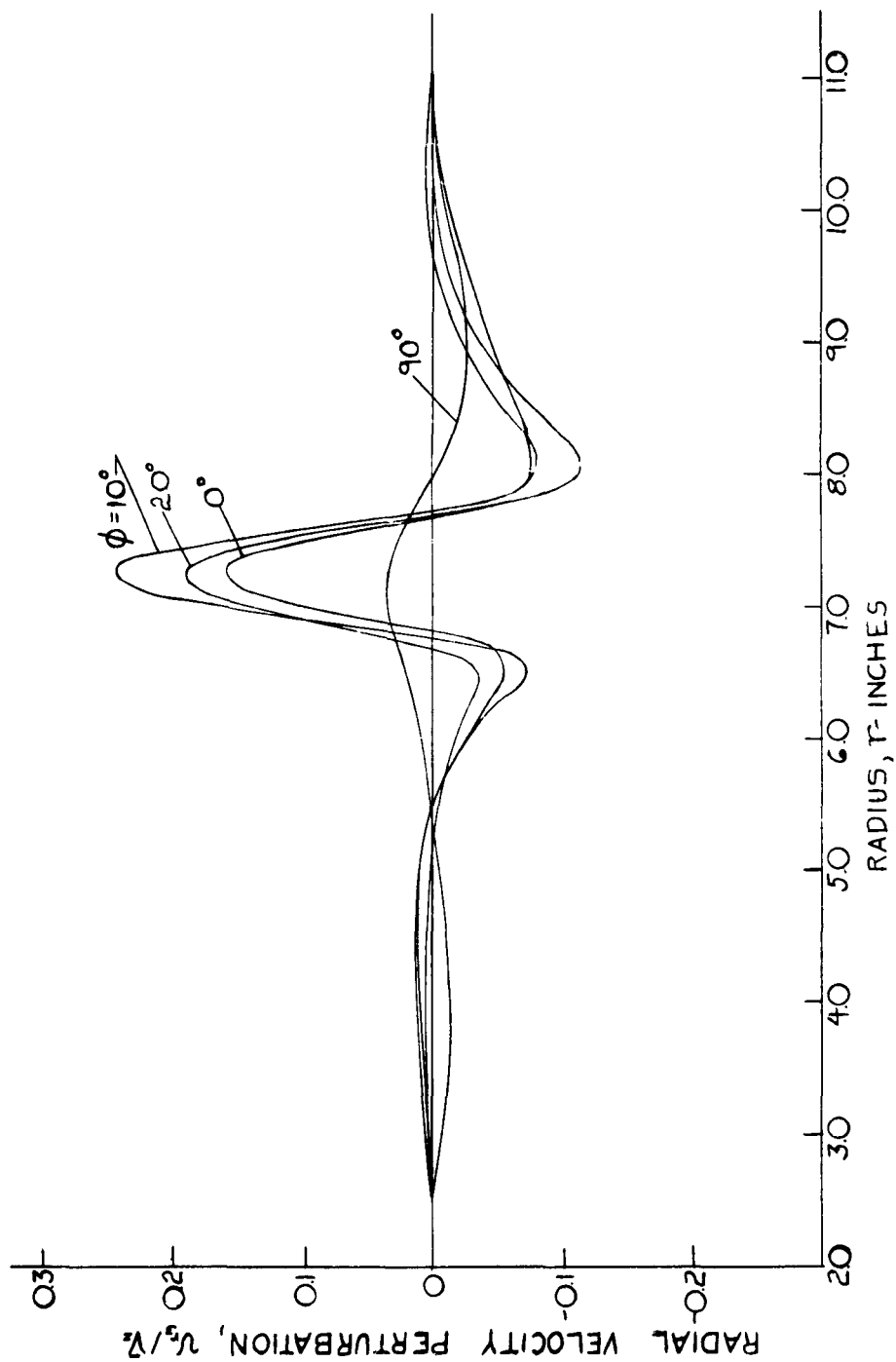


Fig. 59 Calculated Distribution of v_r at $z = d$
($d/R_p = 0.267$, $B = 2$)

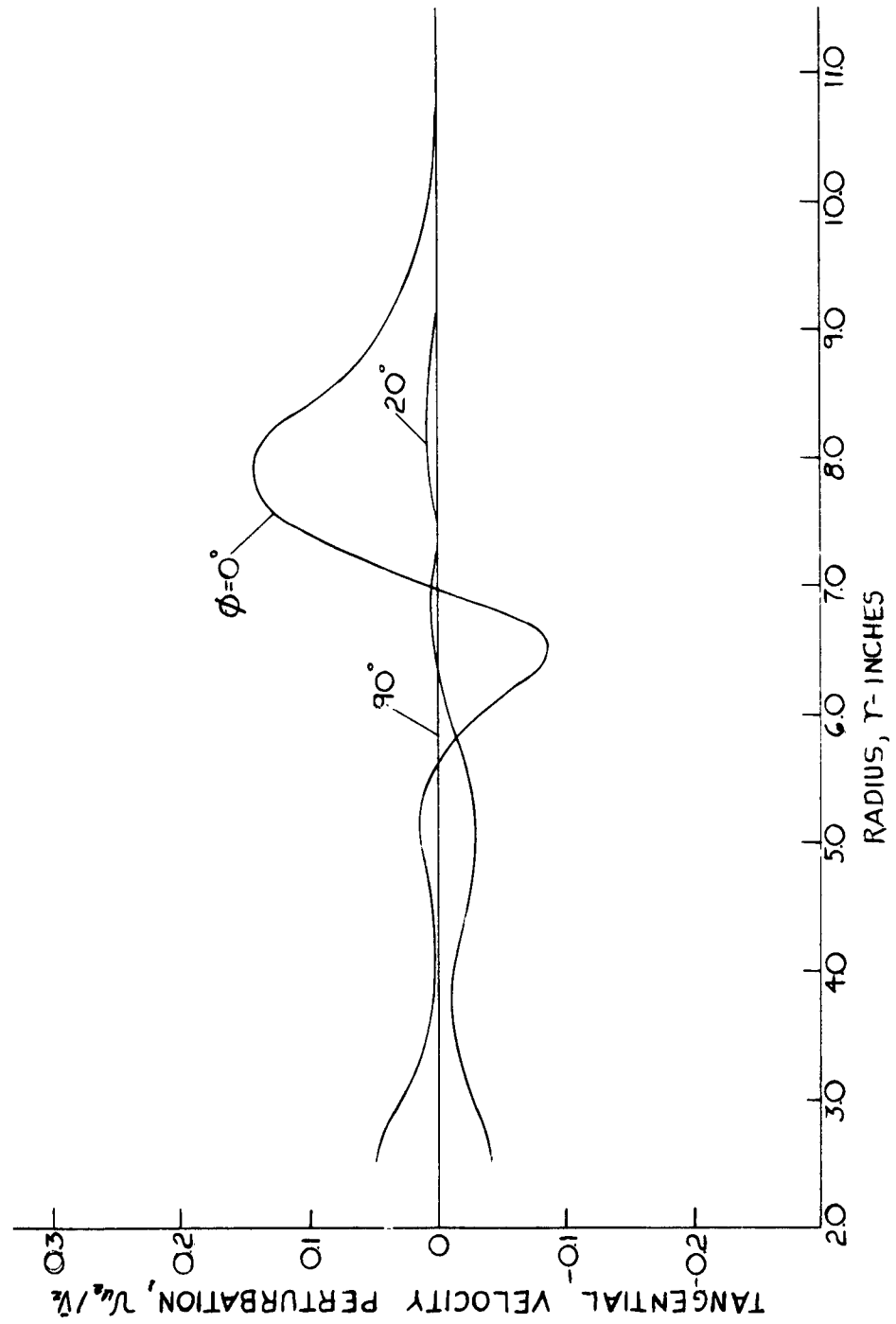


Fig. 60 Calculated Distribution of v_{u_2} at $z = d$
($d/R_p = 0.667$, $B = 10$)

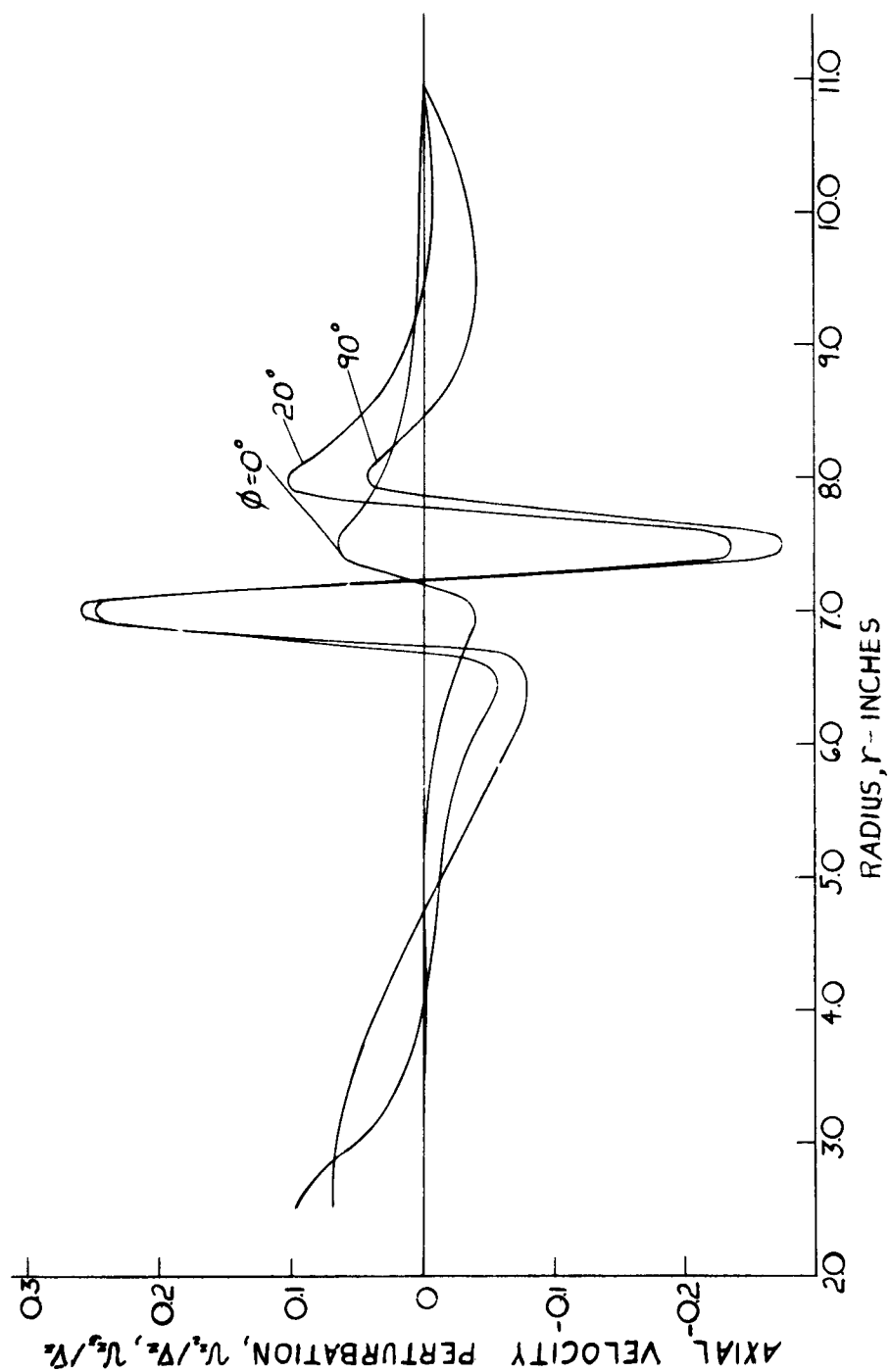


Fig. 61 Calculated Distribution of v_{z2} and v_{z3} at $z = d$
($d/R_p = 0.667$, $B = 10$)

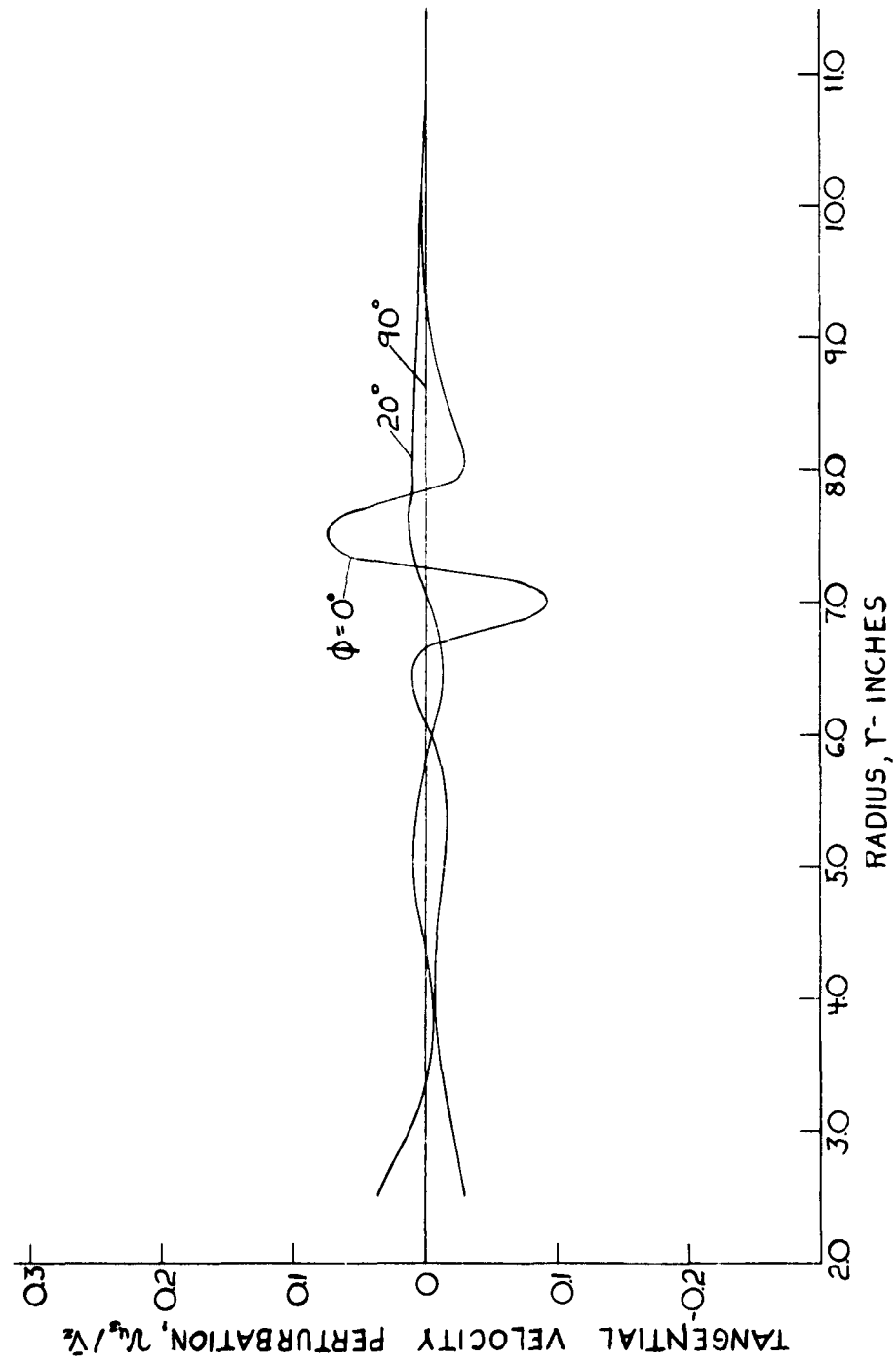


Fig. 62 Calculated Distribution of v_{u3} at $z = d$
 ($d/R_p = 0.667$, $B = 10$)

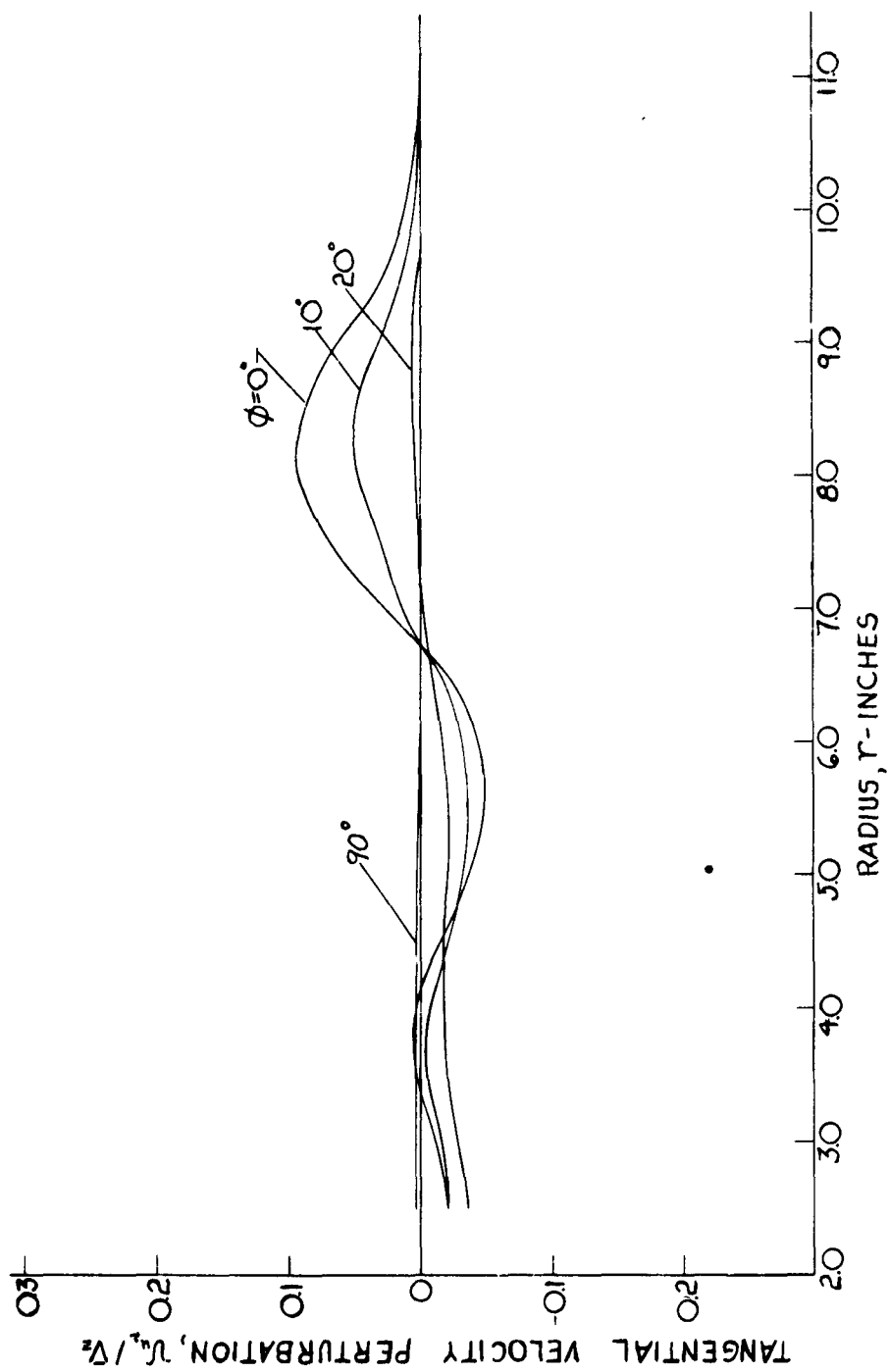


Fig. 63 Calculated Distribution of v_{u_2} at $z = d$
 ($d/R_p = 1.067$, $B = 10$)

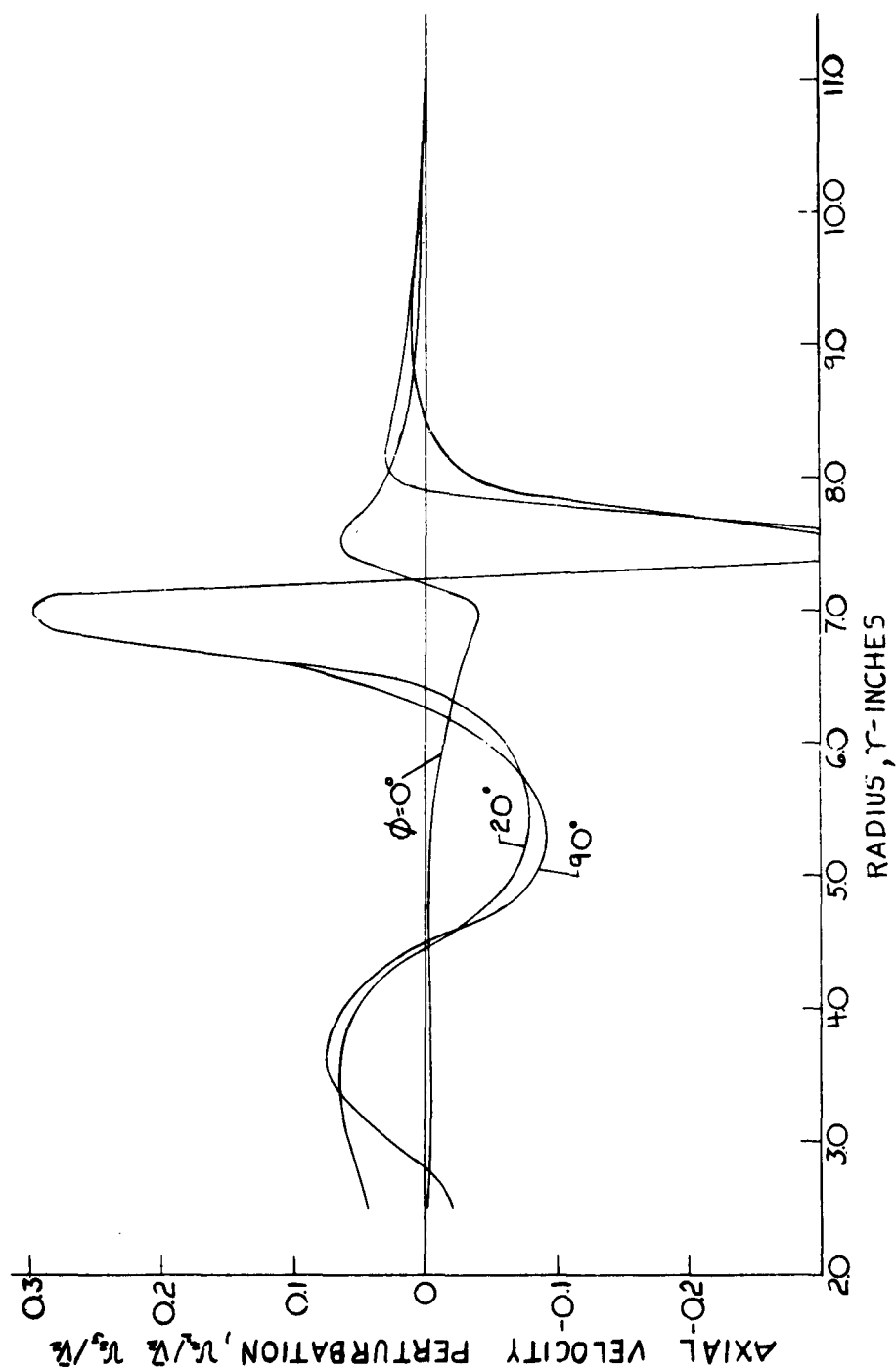


Fig. 64 Calculated Distribution of v_{z2} and v_{z3} at $z = d$
 ($d/R_p = 1.067$, $B = 10$)

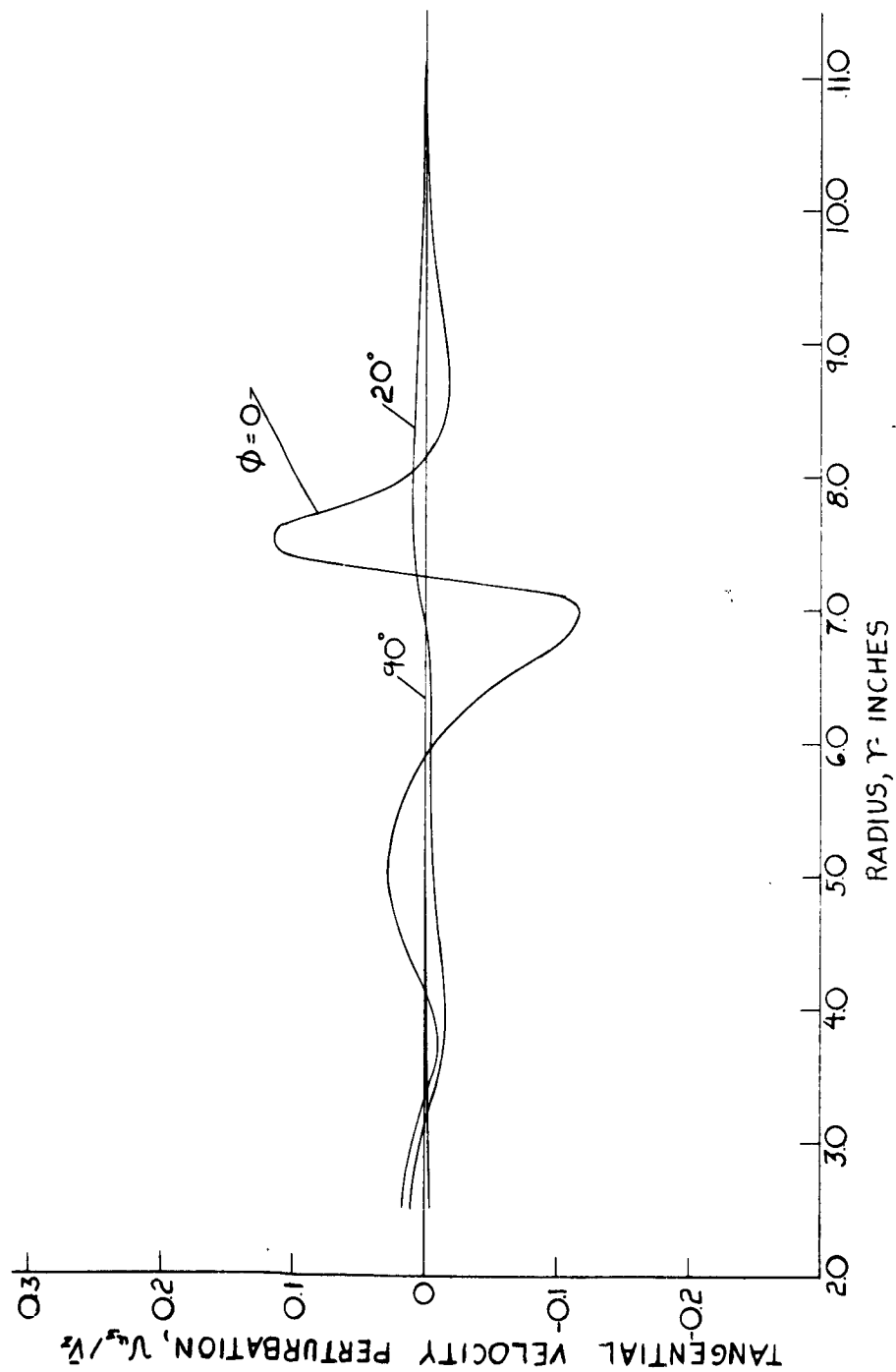


Fig. 65 Calculated Distribution of v_{u3} at $z = d$
($d/R_p = 1.067$, $B = 10$)

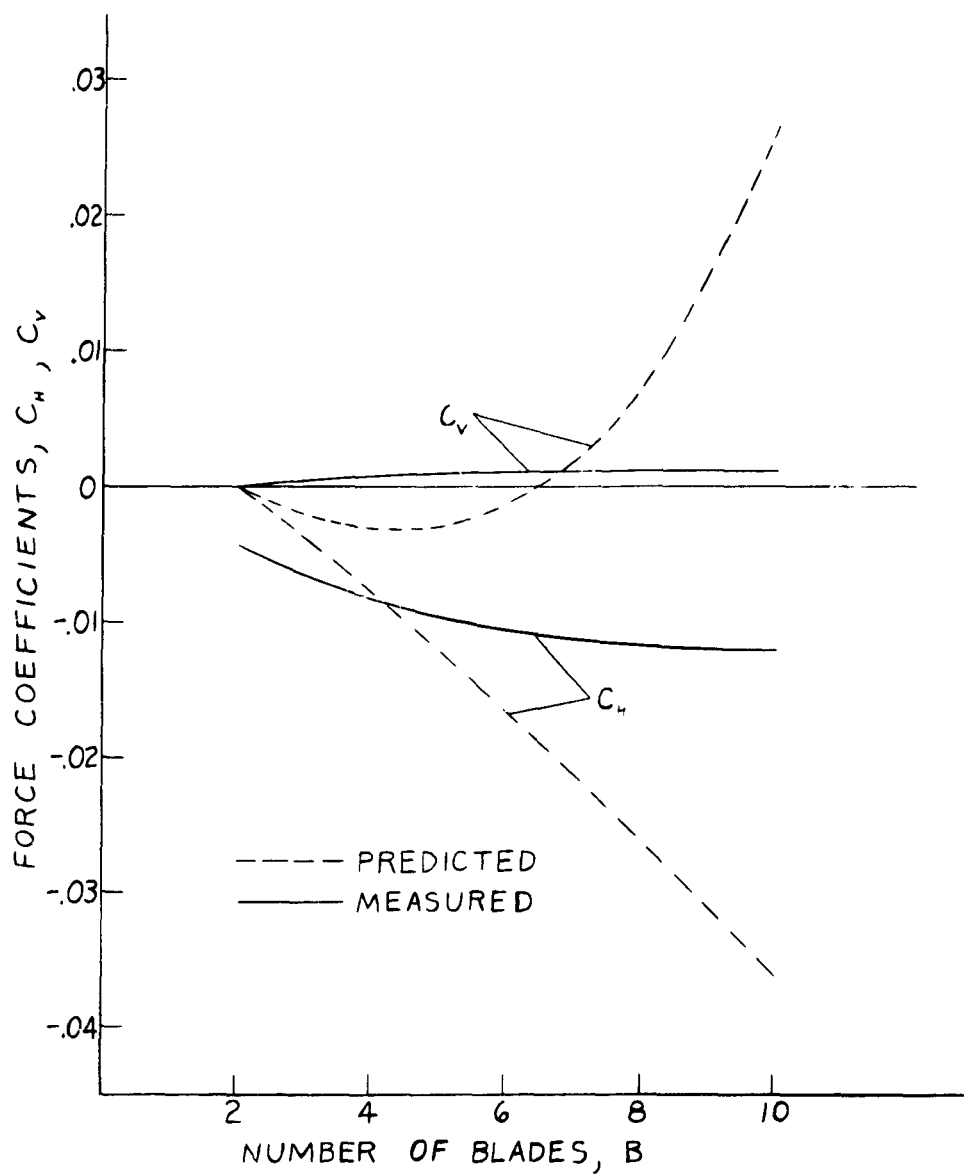


Fig. 66 Comparison of Measured and Calculated Force Coefficients